This is a preprint version of the article published in:
Journal of Sound and Vibration, Vol. 483 (2020), 115441.
https://doi.org/10.1016/j.jsv.2020.115441

Please, cite this document as:
T. G. ZIELIŃSKI, R. VENEGAS, C. PERROT, M. ČERVENKA, F. CHEVILLOTTE, K. ATTENBOROUGH, "Benchmarks for microstructure-based modelling of sound absorbing rigid-frame porous media." *Journal of Sound and Vibration*, Vol. **483** (2020), 115441. DOI: 10.1016/j.jsv.2020.115441

Benchmarks for microstructure-based modelling of sound absorbing rigid-frame porous media

TOMASZ G. ZIELIŃSKI [1,a] RODOLFO VENEGAS [2,b] CAMILLE PERROT [3,c] MILAN ČERVENKA [4,d]
FABIEN CHEVILLOTTE [5,e] KEITH ATTENBOROUGH [6,f]

[a] *Institute of Fundamental Technological Research, Polish Academy of Sciences, ul. Pawińskiego 5B, 02-106 Warsaw, Poland*
[b] *University Austral of Chile, Institute of Acoustics, P.O. Box 567, Valdivia, Chile*
[c] *MSME, Université Gustave Eiffel, UPEC, CNRS, F-77454, Marne-la-Vallée, France*
[d] *Czech Technical University in Prague, Faculty of Electrical Engineering, Technická 2, 166 27 Prague 6, Czech Republic*
[e] *MATELYS – Research Lab, 7 rue des Maraîchers (bâtiment B), F69120 Vaulx-en-Velin, France*
[f] *Faculty of Science, Technology, Engineering and Mathematics, School of Engineering and Innovation, The Open University, Walton Hall, Milton Keynes, MK7 6AA, United Kingdom*

Abstract

This work presents benchmark examples related to the modelling of sound absorbing porous media with rigid frame based on the periodic geometry of their microstructures. To this end, rigorous mathematical derivations are recalled to provide all necessary equations, useful relations, and formulae for the so-called direct multi-scale computations, as well as for the hybrid multi-scale calculations based on the numerically determined transport parameters of porous materials. The results of such direct and hybrid multi-scale calculations are not only cross verified, but also confirmed by direct numerical simulations based on the linearised Navier-Stokes-Fourier equations. In addition, relevant theoretical and numerical issues are discussed, and some practical hints are given.

Key words: Porous media; Periodic microstructure; Wave propagation; Sound absorption.

[1] *Corresponding Author*: tzielins@ippt.pan.pl
[2] rodolfo.venegas@uach.cl
[3] camille.perrot@univ-paris-est.fr
[4] milan.cervenka@fel.cvut.cz
[5] fabien.chevillotte@matelys.com
[6] keith.attenborough@open.ac.uk

1 Introduction

Porous materials are used widely for sound absorption. Methods of determining the bulk acoustical properties of porous media from their microstructures have a long history [1–9]. The classical approach is to assume idealised microstructures, e.g. arrays of pores with constant cross-section [9–13], fibres [14–18], or grains [19–23]. But typical microstructures of porous materials used for sound absorption are much more complicated.

To allow simultaneously for arbitrary pore shapes and pore cross-sections that change along their lengths, Johnson et al. [24] introduced the viscous characteristic length which takes into account the dominance of viscous effects in the narrower pore sections. Champoux, Allard, Lafarge and others [25–27] used an analogous method to account for thermal effects, hence introducing the thermal characteristic length, thermal permeability and thermal tortuosity.

Semi-analytical formulations for the bulk material complex-valued and frequency-dependent density and compressibility of a porous solid resulting from this approach are based upon physically admissible limiting forms for small and large characteristic lengths, in comparison with the viscous or thermal boundary layer thickness, together with the bulk parameters of porosity, steady flow air permeability and high frequency tortuosity. The high frequency tortuosity, otherwise known as the geometrical tortuosity, determines the inertial effect on the fluid motion in the presence of the solid frame. According to Pride et al. [28], another parameter is required to account for the enhancement of the effective fluid inertia at lower frequencies caused by the cross-sectional changes in the pore size and viscous friction at the smallest apertures of the pores.

The most complete semi-analytical model, i.e. the Johnson-Champoux-Allard-Lafarge-Pride (JCALP) model, requires eight transport parameters, namely, porosity, high frequency tortuosity, steady flow viscous permeability, viscous characteristic length, thermal characteristic length, static thermal permeability, and static viscous and thermal tortuosities. When the microstructure of the material closely resembles an array of uniform identical tortuous cylindrical pores, without too abrupt cross-sectional changes, the number of parameters required reduces to six so the JCALP model becomes the Johnson-Champoux-Allard-Lafarge (JCAL) model [24–27]. Recently, Horoshenkov et al. [29–32] have shown that, to predict the acoustical properties of media having a log-normal distribution of pore sizes, only three parameters viz. porosity, steady flow permeability and the standard deviation of the pore size distribution are required.

Gasser et al. [33] and Perrot et al. [34–36] have explored a technique based on numerical calculations of the transport parameters in rigid-frame porous media with complicated microstructures. Since the variability in the porous microstructures usually makes it difficult to identify local micro-geometry that can be used to predict bulk acoustical properties, a Representative Elementary Volume (REV) or Periodic Unit Cell (PUC) is used to reconstruct the actual microstructure in an idealised manner. For example, open cell polymer foams are represented by truncated octahedra with circular cross section ligaments and spherical nodes at their intersections. The dimensions of the PUC are deduced from the measurements of porosity and steady flow resistivity or from 3D images. Each PUC can be used for direct multiscale calculations which require solving the harmonic (i.e. oscillatory) Stokes flow and heat transfer equations for each frequency. Alternatively, the transport parameters can be computed from the steady Stokes flow and Laplace equations related to viscous and inertial effects, respectively, and from the Poisson equation related to heat transfer. This approach is less computationally intensive, since it uses the computed eight (or fewer) parameters as inputs to the semi-analytical formulae of the JCALP model (or its variations). Such a hybrid approach has been used to investigate the acoustical properties of fibrous materials [37–43], granular media [33, 37, 44–47], various polymeric and open-cell foams [34, 35, 48–59], ceramic foams with spherical pores [60], metallic foams [36], and syntactic hybrid foams, i.e. open-cell polyurethane foams with embedded hollow microbeads [61]. Moreover, a similar microstructure-based approach has been applied to model media with multiple scales [23, 37, 62–64], and recently, it has been used to study (and design) novel materials manufactured using modern additive manufacturing technologies, e.g. 3D-printed foams [65], optimally graded porous materials [66] and adaptable absorbers [67, 68], sintered fibrous materials [69–72], and even micro-perforated plates with complex patterns of micro-slits [73].

This paper provides a complete illustration of the microstructure-based approach for modelling of sound absorbing media by comparing the results of the direct and hybrid multiscale calculations, and also validating them with predictions obtained from direct numerical simulations based on the linearised, oscillatory, compressible Navier-Stokes-Fourier equations. Given the intricacies of the numerical calculations that are necessary, the purpose is to provide benchmark calculations for substantially different periodic microstructures. These should enable researchers who carry out such simulations in future to check the accuracy of their results.

The three calculation methods that were used for each benchmark problem are summarised in Section 2. Section 3 provides full descriptions of the calculations and the associated numerical results for two easily reproducible benchmark microstructures: (1) a two-dimensional periodic array of straight parallel fibres with circular cross-sections (Section 3.1), and (2) a regular periodic foam with identical spherical pores (Section 3.2). Computational hints are offered and concluding remarks are presented in Section 4. These should facilitate implementation of the methods and consequent benchmark computations using commercial finite element software (like *COMSOL Multiphysics*) or freeware (e.g. *FreeFEM++* [74, 75]). The full theoretical background is given in Appendix A, where equations for the acoustic wave

propagation in rigid-frame porous materials with arbitrary microstructures are derived using homogenisation theory, and the basis is supplied thereby for the direct multiscale calculations and also for numerical analyses required to determine the parameters used during the alternative hybrid multiscale calculations. The starting point for these derivations are the linearised Navier-Stokes-Fourier equations, which are also used for the computationally demanding direct numerical simulations.

2 Calculation methods and procedures

Three calculation approaches are used to determine sound absorption properties of porous and fibrous layers serving as benchmark examples, namely:

- **DNS** – *Direct Numerical Simulation* (see Table 1),
- **DM** – *Direct Multiscale* calculations (see Table 2),
- **HM** – *Hybrid Multiscale* calculations (see Table 3).

Tables 1, 2, and 3 present the calculation procedures for each method. Each table summarises the relevant equations (i.e. boundary value problems) and formulae necessary for calculations and for implementing the procedure. Note that some calculation steps can be performed in parallel, viz. harmonic viscous flow (HVF) and harmonic thermal diffusion (HTD) in Table 2, or Laplace's problem (LP), Stokes flow (SF), and Poisson's problem (PP) in Table 3. The full theoretical foundations for these methods are discussed in detail in Appendix A, where we show, in particular, how the DM method is obtained from DNS equations based on the assumptions of periodicity, scale separation, and local incompressibility. Therefore, below we only briefly discuss each method by stating the boundary value problems, dependent field variables and other involved functions. We also give the names of transport parameters used in the HM method referring to Appendix A for more details. Other parameters in the procedure tables describe the properties of the fluid and are summarised in Table 4, where the values for air used in the benchmark calculations are also given.

Table 1: Procedure for Direct Numerical Simulations (DNS)

DNS Solve the Navier-Stokes-Fourier equations of oscillatory viscous, compressible flow for p, $\mathbf{v}$, ϱ, and T in the fluid domain inside the "whole thickness" of a porous layer and the adjacent layer of air:

$$\eta\left(\nabla^2\mathbf{v}+\frac{1}{3}\nabla(\nabla\cdot\mathbf{v})\right)-\nabla p=\mathrm{i}\omega\varrho_0\mathbf{v} \quad \text{in } \Omega_\mathrm{f}, \qquad \mathbf{v}=\mathbf{0} \quad \text{on } \Gamma_\mathrm{sf},$$

$$\varrho_0\nabla\cdot\mathbf{v}+\mathrm{i}\omega\varrho=0 \quad \text{in } \Omega_\mathrm{f},$$

$$\kappa\nabla^2 T=\mathrm{i}\omega\varrho_0 C_\mathrm{p}T-\mathrm{i}\omega p \quad \text{in } \Omega_\mathrm{f}, \qquad T=0 \quad \text{on } \Gamma_\mathrm{sf}.$$

$$\frac{p}{P_0}=\frac{\varrho}{\varrho_0}+\frac{T}{T_0} \quad \text{in } \Omega_\mathrm{f},$$

with additional appropriate boundary conditions on lateral planes of symmetry or periodicity, and on the boundary of the plane incident wave. Use p and $\mathbf{v}$ to determine the required acoustic descriptors (surface acoustic impedance, sound absorption).

The *Direct Numerical Simulation* (DNS) consists in solving a coupled visco-thermal problem in harmonic regime, i.e. for a discrete set of angular frequencies ω, described by the set of equations summarised in Table 1 (note that these are field equations (A.1)–(A.4) in the fluid domain as well as no-slip (A.5) and isothermal boundary conditions (A.6) on solid walls). The computations are performed at the micro-scale: on the "whole" fluid domain Ω_f inside a band of a layer of porous or fibrous material with an adjacent thin layer of air in order to apply the plane wave excitation at some sufficient distance from the layer. The solid boundary Γ_sf consists not only of the walls of the solid skeleton (or fibres) inside the band but also of the rigid backing wall. The periodic or, if possible, symmetric conditions are applied only on the lateral fluid boundaries of the band, and the adiabatic pressure condition is applied on the external boundary of the adjacent air layer exposed to the normally-incident wave. The results are the complex-valued fields of acoustic pressure p, particle velocity $\mathbf{v}$, temperature T and density ϱ fluctuation in the fluid domain Ω_f, determined for each computational frequency ω. The sound absorption of the porous layer is computed as

$$A(\omega)=1-|R(\omega)|^2, \qquad R(\omega)=\frac{Z_\mathrm{s}(\omega)-Z_0}{Z_\mathrm{s}(\omega)+Z_0}, \tag{1}$$

where the surface acoustic impedance $Z_s(\omega)$ is calculated directly from its definition as the ratio between the pressure and (negative) normal velocity determined as the average on some surface inside the adjacent layer of air (with characteristic impedance Z_0), since the propagation in this layer is practically lossless. Moreover, $Z_s(\omega)$ can be also computed at any single point on the external boundary of the adjacent air layer where the wave is plane.

Table 2: Procedure for Direct Multiscale (DM) computations

HVF Solve the scaled problem of harmonic (oscillatory) viscous, incompressible flow for $\hat{\mathbf{k}}$ and $\hat{\pi}$ in a REV:

$$\begin{aligned} \frac{\mathrm{i}\omega}{\nu}\hat{\mathbf{k}} - \nabla_y^2\hat{\mathbf{k}} + \nabla_y\hat{\pi} &= \mathbf{e} \quad \text{in } \Omega_\mathrm{f}, \\ \nabla_y\cdot\hat{\mathbf{k}} &= 0 \quad \text{in } \Omega_\mathrm{f}, \\ \hat{\mathbf{k}} &= \mathbf{0} \quad \text{on } \Gamma_\mathrm{sf}, \end{aligned}$$

with additional periodic (or symmetric and asymmetric) boundary conditions on the appropriate planes.

HTD Solve the scaled problem of harmonic (oscillatory) thermal diffusion for $\tilde{\theta}$ in a REV:

$$\begin{aligned} \frac{\mathrm{i}\omega}{\nu_\mathrm{th}}\tilde{\theta} - \nabla_y^2\tilde{\theta} &= 1 \quad \text{in } \Omega_\mathrm{f}, \\ \tilde{\theta} &= 0 \quad \text{on } \Gamma_\mathrm{sf}, \end{aligned}$$

with additional periodic (or symmetric) boundary conditions on the appropriate planes.

DYNAMIC FUNCTIONS Compute the dynamic permeability functions:

$$\mathcal{K}(\omega) = \phi\left\langle\hat{\mathbf{k}}(\omega)\cdot\mathbf{e}\right\rangle_\mathrm{f}, \qquad \theta(\omega) = \phi\left\langle\tilde{\theta}(\omega)\right\rangle_\mathrm{f},$$

where $\phi = \Omega_\mathrm{f}/\Omega$ and $\langle.\rangle_\mathrm{f} = \frac{1}{\Omega_\mathrm{f}}\int_{\Omega_\mathrm{f}}(.)\,\mathrm{d}\Omega$. Calculate the dynamic tortuosity functions:

$$\alpha(\omega) = \frac{\phi\,\nu}{\mathrm{i}\omega\,\mathcal{K}(\omega)}, \qquad \alpha_\mathrm{th}(\omega) = \frac{\phi\,\nu_\mathrm{th}}{\mathrm{i}\omega\,\theta(\omega)}.$$

EFFECTIVE PROPERTIES Calculate effective properties of the equivalent fluid:

$$\varrho_\mathrm{e}(\omega) = \frac{\varrho_0\,\alpha(\omega)}{\phi}, \quad \mathcal{C}(\omega) = \frac{\phi\,\beta(\omega)}{\gamma P_0}, \quad c_\mathrm{e}(\omega) = \frac{c_0}{\sqrt{\alpha(\omega)\beta(\omega)}},$$

$$\text{where} \quad \beta(\omega) = \gamma - \frac{\gamma-1}{\alpha_\mathrm{th}(\omega)}.$$

MACRO-SCALE COMPUTATIONS Solve the corresponding Helmholtz problem on the macro-scale domain (for the acoustic pressure p), typically for a layer of the effective fluid equivalent to the porous medium, viz.:

$$\nabla^2 p + \frac{\omega^2}{c_\mathrm{e}^2(\omega)}p = 0\,,$$

with appropriate boundary conditions (e.g. the sound-hard b.c. $\nabla p = 0$ on rigid walls and symmetry planes, the pressure b.c. on the boundary of the plane incident wave). Compute the particle velocity field $\mathbf{v} = -\frac{\nabla p}{\mathrm{i}\omega\,\varrho_\mathrm{e}(\omega)}$. Use p and $\mathbf{v}$ to determine the required acoustic descriptors (surface acoustic impedance, sound absorption).

The *Direct Multiscale* (DM) calculations involve two uncoupled harmonically-driven complex-valued analyses, namely: the scaled harmonic viscous incompressible flow in a preferential direction $\mathbf{e}$ with no-slip boundary conditions on solid walls – see HVF in Table 2 (also equations (A.34)–(A.36)), and the scaled harmonic thermal diffusion with isothermal boundary conditions on solid walls – see HTD in Table 2 (also equations (A.38) and (A.39)). Both analyses are carried out for a set of computational frequencies ω, in the fluid domain Ω_f of a periodic representative elementary volume or cell Ω of a porous or fibrous medium of open porosity $\phi = \Omega_\mathrm{f}/\Omega$. The solid boundaries Γ_sf are only those inside Ω. The unknowns for the viscous flow problem are the normalised fields of velocity $\hat{\mathbf{k}}$ and pressure $\hat{\pi}$, while the thermal diffusion problem is solved for a normalised field of temperature $\tilde{\theta}$. The normalised fields $\hat{\mathbf{k}}$ and $\tilde{\theta}$ have the dimension of permeability (m^2) and the so-called dynamic viscous permeability of porous medium $\mathcal{K}(\omega)$ and dynamic thermal permeability $\theta(\omega)$ are *directly* calculated by averaging them over the REV as shown in Table 2 (see also Section A.2). Then, the so-called dynamic viscous $\alpha(\omega)$ and thermal $\alpha_\mathrm{th}(\omega)$ tortuosities are found from the formulae shown in Table 2 (see also equations (A.41) and (A.42), respectively). The dynamic permeabilities (or tortuosities) enable determination of the effective properties for a fluid equivalent to the porous material as described in Section A.1 or A.2. In particular, we determine the effective density $\varrho_\mathrm{e}(\omega)$, compressibility $\mathcal{C}(\omega)$, and sound speed $c_\mathrm{e}(\omega)$, which is used to solve the macro-scale Helmholtz problem

(see Table 2). Finally, based on the solution of the Helmholtz problem for a layer of such material with a thickness of h, the following formula for the surface acoustic impedance is derived

$$Z_{\mathrm{s}}(\omega) = -\mathrm{i}\varrho_{\mathrm{e}}(\omega)c_{\mathrm{e}}(\omega)\cot\left(\frac{\omega h}{c_{\mathrm{e}}(\omega)}\right). \tag{2}$$

The surface acoustic impedance $Z_{\mathrm{s}}(\omega)$ is an important acoustic descriptor, which is used to determine the reflection, $R(\omega)$, and acoustic absorption, $A(\omega)$, coefficients for the porous layer using formulae (1). The three acoustic descriptors $Z_{\mathrm{s}}(\omega)$, $R(\omega)$, and $A(\omega)$, calculated in that way, i.e. using the DM approach, can be compared with the corresponding results of DNS.

Table 3: Procedure for Hybrid Multiscale (HM) calculations

LP Solve the Laplace's problem for q in a REV:

$$\nabla_y^2 q = 0 \quad \text{in } \Omega_{\mathrm{f}},$$
$$\nabla_y q \cdot \mathbf{n} = \mathbf{e}\cdot\mathbf{n} \quad \text{on } \Gamma_{\mathrm{sf}},$$

with additional periodic (or symmetric and asymmetric) boundary conditions on the appropriate planes. Compute: $\mathbf{E} = \mathbf{e} - \nabla_y q$.

SF Solve the scaled Stokes flow problem for $\hat{\mathbf{k}}_0$ and $\hat{\pi}_0$ in a REV:

$$-\nabla_y^2\hat{\mathbf{k}}_0 + \nabla_y\hat{\pi}_0 = \mathbf{e} \quad \text{in } \Omega_{\mathrm{f}},$$
$$\nabla_y\cdot\hat{\mathbf{k}}_0 = 0 \quad \text{in } \Omega_{\mathrm{f}},$$
$$\hat{\mathbf{k}}_0 = \mathbf{0} \quad \text{on } \Gamma_{\mathrm{sf}},$$

with additional periodic (or symmetric and asymmetric) boundary conditions on the appropriate planes.

PP Solve the Poisson's problem for $\tilde{\theta}_0$ in a REV:

$$-\nabla_y^2\tilde{\theta}_0 = 1 \quad \text{in } \Omega_{\mathrm{f}},$$
$$\tilde{\theta}_0 = 0 \quad \text{on } \Gamma_{\mathrm{sf}},$$

with additional periodic (or symmetric) boundary conditions on the appropriate planes.

TRANSPORT PARAMETERS Calculate the required transport parameters (all 8 for the JCALP model):

$$\phi = \frac{\Omega_{\mathrm{f}}}{\Omega}, \qquad \alpha_\infty = \frac{\langle\mathbf{E}\cdot\mathbf{E}\rangle_{\mathrm{f}}}{\langle\mathbf{E}\rangle_{\mathrm{f}}\cdot\langle\mathbf{E}\rangle_{\mathrm{f}}}, \qquad \alpha_{0\mathrm{v}} = \frac{\left\langle\hat{\mathbf{k}}_0\cdot\hat{\mathbf{k}}_0\right\rangle_{\mathrm{f}}}{\left\langle\hat{\mathbf{k}}_0\right\rangle_{\mathrm{f}}\cdot\left\langle\hat{\mathbf{k}}_0\right\rangle_{\mathrm{f}}}, \qquad \alpha_{0\mathrm{th}} = \frac{\left\langle\tilde{\theta}_0^2\right\rangle_{\mathrm{f}}}{\left\langle\tilde{\theta}_0\right\rangle_{\mathrm{f}}^2},$$

$$\Lambda_{\mathrm{th}} = 2\frac{\Omega_{\mathrm{f}}}{\Gamma_{\mathrm{sf}}}, \qquad \Lambda_{\mathrm{v}} = 2\frac{\int_{\Omega_{\mathrm{f}}}\mathbf{E}\cdot\mathbf{E}\,\mathrm{d}\Omega}{\int_{\Gamma_{\mathrm{sf}}}\mathbf{E}\cdot\mathbf{E}\,\mathrm{d}\Gamma}, \qquad \mathcal{K}_0 = \phi\left\langle\hat{\mathbf{k}}_0\cdot\mathbf{e}\right\rangle_{\mathrm{f}}, \qquad \theta_0 = \phi\left\langle\tilde{\theta}_0\right\rangle_{\mathrm{f}}.$$

JCA / JCAL / JCALP MODEL Calculate the dynamic tortuosity functions

$$\alpha(\omega) = \alpha(\omega;\phi,\alpha_\infty,\alpha_{0\mathrm{v}},\mathcal{K}_0,\Lambda_{\mathrm{v}}), \qquad \alpha_{\mathrm{th}}(\omega) = \alpha_{\mathrm{th}}(\omega;\phi,\alpha_{0\mathrm{th}},\theta_0,\Lambda_{\mathrm{th}}),$$

using transport parametrs and formulas (A.79)–(A.82) according to the JCALP, JCAL, or JCA model. Additionally, calculate the dynamic permeability functions:

$$\mathcal{K}(\omega) = \frac{\phi\,\nu}{\mathrm{i}\omega\,\alpha(\omega)}, \qquad \theta(\omega) = \frac{\phi\,\nu_{\mathrm{th}}}{\mathrm{i}\omega\,\alpha_{\mathrm{th}}(\omega)}.$$

EFFECTIVE PROPERTIES & **MACRO-SCALE COMPUTATIONS** See Table 2.

In the case of the *Hybrid Multiscale* (HM) calculations three uncoupled, frequency-independent and real-valued problems are solved: the Laplace's problem – see LP in Table 3 (also equations (A.58)–(A.59)), the scaled problem of the Stokes flow – see SF in Table 3 (also equations (A.70)–(A.72)), and the Poisson's problem – see PP in Table 3 (also equations (A.75)–(A.76)). Each problem is defined in the fluid domain Ω_{f} of a periodic REV or cell Ω, as in the case of DM computations. The representative geometry and results of static solutions are used to determine the transport parameters as described in Section A.3. These are (see Table 3): the porosity ϕ, (geometrical) tortuosity α_∞, static viscous $\alpha_{0\mathrm{v}}$ and thermal $\alpha_{0\mathrm{th}}$ tortuosities, static viscous $\mathcal{K}_0$ and thermal θ_0 permeabilities, and two characteristic lengths, i.e. the viscous length Λ_{v} and thermal length Λ_{th}. These numerically-computed parameters are used to calculate the dynamic tortuosities (A.79) and (A.81), as well as the dynamic permeabilities (A.83) (see also Table 3), using the analytical approximations according to each of the three models (i.e. JCA, JCAL, and JCALP) discussed in Section A.3. The dynamic functions computed with this *Hybrid* approach can be confronted with the corresponding DM results. Then, the effective properties of such a homogenised medium equivalent to a porous material, as well as the acoustic descriptors (i.e. the surface acoustic impedance, reflection and acoustic absorption coefficients) for a porous layer of known thickness modelled on a macro-scale using the Helmholtz equation, can be calculated in the same way as in the case of the *Direct Multiscale* method (see Table 2).

The following finite-element approximation functions were applied in numerical analyses. The Taylor-Hood approximation [76] was used for the scaled (static as well as harmonic) viscous flow problems, which means quadratic (i.e. second-order Lagrange) functions for all components of the scaled velocity fields $\hat{\mathbf{k}}$ and $\hat{\mathbf{k}}_0$, while linear functions for the scaled pressure fields $\hat{\pi}$ and $\hat{\pi}_0$. The quadratic Lagrange approximation was also applied for the field of scaled potential q, as well as for the scaled temperature fields $\tilde{\theta}$ and $\tilde{\theta}_0$. To ensure high accuracy of the results of benchmark calculations, the quadratic approximation was also used for geometry (when the software implementation allowed it), since it does not change the number of degrees of freedom, but may slightly improve the overall accuracy in case of curved boundaries. Finally, in the case of DNS, the density fluctuation ϱ is eliminated from the set of equations (A.1)–(A.4) (by using the last one of them) and the problem is formulated with respect to the remaining fields of acoustic pressure p (approximated with linear functions), particle velocity $\mathbf{v}$ (with components approximated using the Lagrange quadratic functions), and temperature fluctuation T (with the quadratic Lagrange approximation).

Table 4: Air properties at temperature of 20°C and ambient mean (atmospheric) pressure of 1 atmosphere (i.e. 101325 Pa)

Parameter name	**Symbol**	**Unit**	**Value**	(*formula*)
ambient mean pressure	P_0	Pa	101325	
ambient mass density	ϱ_0	$\mathrm{kg/m^3}$	1.205	
heat capacity ratio	γ	–	1.400	
dynamic viscosity	η	Pa·s	$1.821 \cdot 10^{-5}$	
thermal conductivity	κ	W/(m·K)	0.02560	
isobaric specific heat	C_p	J/(kg·K)	1006	
adiabatic bulk modulus	B_0	Pa	141855	$= \gamma\, P_0$
speed of sound	c_0	m/s	343.1	$= \sqrt{B_0/\varrho_0}$
characteristic impedance	Z_0	Pa·s/m	413.4	$= \varrho_0\, c_0$
Prandtl number	N_Pr	–	0.7156	$= \eta\, C_\mathrm{p}/\kappa$
kinematic viscosity	ν	$\mathrm{m^2/s}$	$1.511 \cdot 10^{-5}$	$= \eta/\varrho_0$
thermal diffusivity	ν_th	$\mathrm{m^2/s}$	$2.112 \cdot 10^{-5}$	$= \nu/N_\mathrm{Pr}$

Table 4 presents air properties at "standard conditions" of temperature and pressure (that is, at 20°C and 1 atmosphere) used in the calculations. Apart from the values of the ambient mean pressure and adiabatic bulk modulus, all other data are listed with an accuracy to 4 significant digits. The parameters with names in *italics* are computed from the (recalled) well-known formulae using the "basic" parameters. Note that the bulk viscosity of air is neglected, which is consistent with *Multiscale* calculations, where this parameter would have no effect at all, since incompressible flow is assumed on the micro-scale level.

3 Numerical benchmark examples

3.1 BENCHMARK 1: A periodic fibrous material composed of straight parallel fibres with circular cross-sections

Figure 1 shows the (micro- and macro-) geometry of a fibrous layer composed of straight parallel fibres. The material is truly periodic and contains two types of fibres with circular cross-sections, which differ only by their diameters, namely, $D_1 = 0.04\,\mathrm{mm}$ and $D_2 = 0.05\,\mathrm{mm}$. Moreover, the direction of wave propagation in such artificial fibrous material is assumed perpendicular to the fibres, which means that the micro-scale geometry and analyses on the microstructural level are essentially two-dimensional. The periodic micro-geometry can be represented in the y_1y_2-plane by a square cell containing two fibres as depicted in Figure 1; the cell size is $\ell_\mathrm{c} = 0.20\,\mathrm{mm}$, while the "horizontal" and "vertical" projections of the distance between the two fibres are $d_\mathrm{h} = 0.08\,\mathrm{mm}$ and $d_\mathrm{v} = 0.10\,\mathrm{mm}$, respectively. The fibrous material would be structurally isotropic in the y_1y_2-plane and transversally isotropic in 3D, with the symmetry axis along the y_3 direction, if $d_\mathrm{h} = d_\mathrm{v}$. This is not fulfilled. However, since d_h and d_v differ only slightly, and the propagation along the fibres (i.e. in the direction of y_3-axis) is completely different than in the y_1y_2-plane, the material can be treated as *nearly* transversally isotropic.

The (preferential) propagation direction $\mathbf{e}$ is assumed along the y_1-axis which coincides with the "macroscopic" x_1-axis (see Figure 1). Plane waves propagate at normal incidence into a rigidly-backed layer of fibrous material with thickness $h = N_\mathrm{c}\ell_\mathrm{c}$, where N_c is the number of cells along the propagation direction (see Figures 1 and 2). Three cases will be considered: (1) $N_\mathrm{c} = 50$, $h = 10\,\mathrm{mm}$, (2) $N_\mathrm{c} = 80$, $h = 16\,\mathrm{mm}$, and (3) $N_\mathrm{c} = 120$, $h = 24\,\mathrm{mm}$. The thickness of the adjacent lossless layer of air is $h_\mathrm{a} = 10\ell_\mathrm{c} = 2\,\mathrm{mm}$ in each case. Figure 2 shows the whole microstructural geometry of the fibrous layer used in *Direct Numerical Simulations* together with the adjacent air layer and relevant boundary

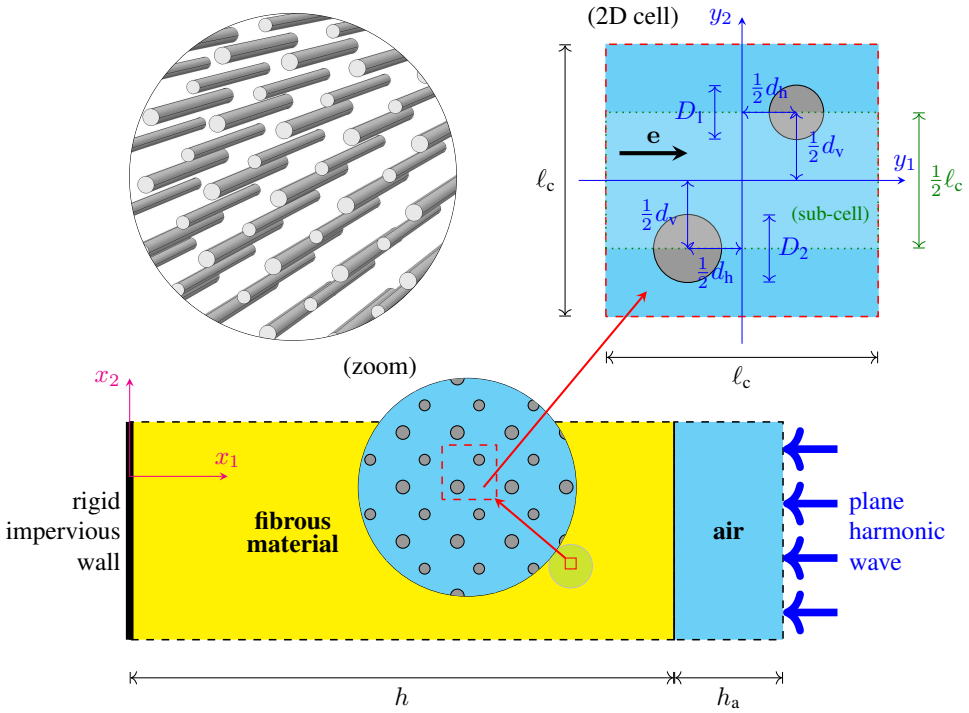

Figure 1: Macro-scale configuration of a sound-absorbing layer with a lossless adjacent layer of air, showing also a micro-scale zoom and a periodic two-dimensional cell representative for a fibrous material with straight parallel fibres of circular cross-sections

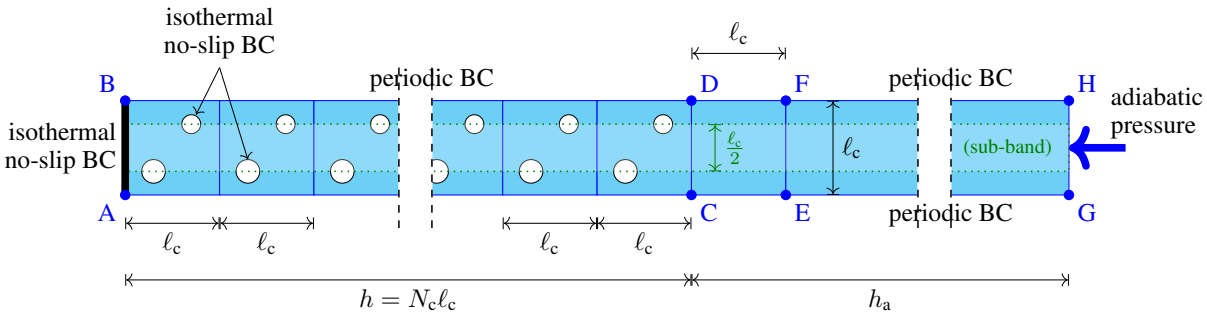

Figure 2: Microstructural geometry of the periodic fibrous layer and boundary conditions used in DNS

conditions: isothermal and no-slip on the solid surfaces of fibres and the backing wall, periodic on the top and bottom boundaries of the fluid band domain, and the adiabatic pressure excitation on the external face of the air layer.

It is important to notice that $d_v = \frac{1}{2}\ell_c$, which means that there are horizontal axes (planes) of symmetry, parallel to the direction of propagation. As shown in Figure 1, a semi-symmetric / semi-periodic sub-cell can be resected from the periodic cell by the parallel symmetry axes which pass through the centre of (respectively) the top or bottom fibre. This sub-cell can be used, instead of the periodic representative cell, in all *Multiscale* calculations with the relevant symmetric boundary conditions applied on the symmetry edges. The issue of symmetric (and antisymmetric) boundary conditions will be discussed in Section 3.2. The advantage of symmetry should be also taken in the case of DNS, where simulations can be carried out on the symmetric sub-band shown in Figure 2, by applying the symmetry boundary conditions along the top and bottom edges of such fluid sub-domain.

Figure 3 presents two finite-element meshes used for the *Multiscale* calculations (one generated on the periodic cell and the other on the semi-periodic sub-cell), as well as a finite-element mesh of the sub-band of the fluid domain used for DNS; the edges of periodicity and symmetry are indicated in each of the mesh cases. The static finite-element analyses (scaled Stokes', Laplace's and Poisson's problems) were carried out using the periodic and semi-periodic meshes. The results are essentially the same for both mesh cases, as presented in Figure 4, and they served to calculate the relevant transport parameters for the fibrous material.

The values of all transport parameters are given in Table 5 with accuracy of 5 significant digits. Within this accuracy, the same results were obtained using the cell and the sub-cell finite-element meshes shown in Figure 3, and even with

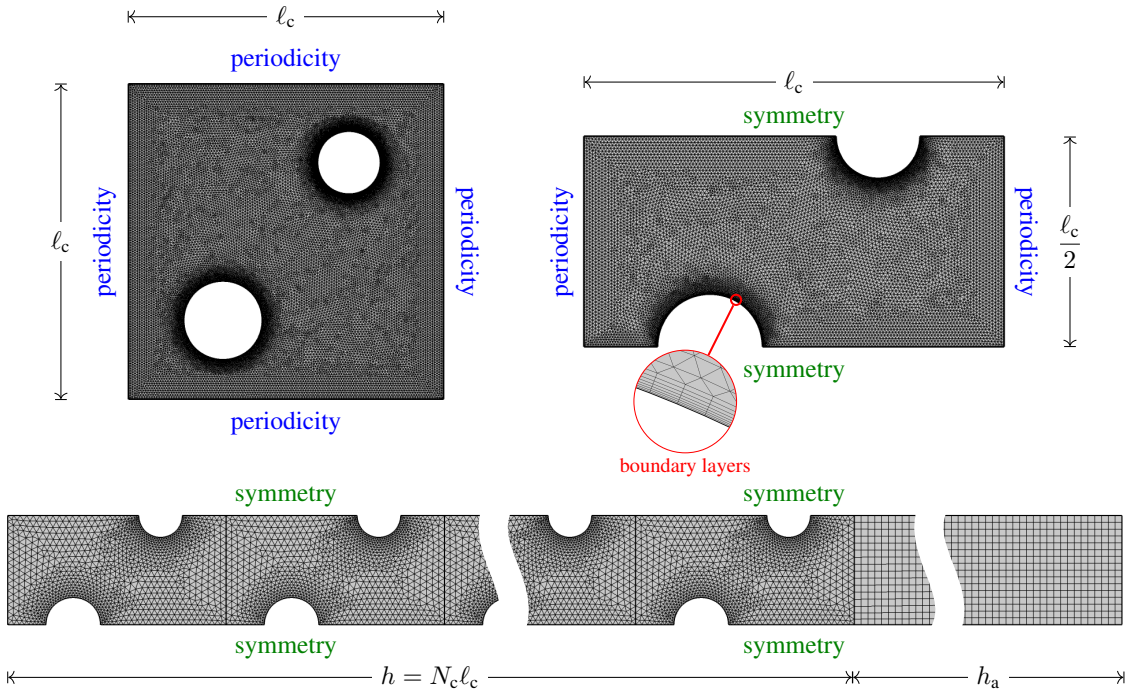

Figure 3: Finite element meshes on the computational fluid domains for the periodic fibrous material used for *Multiscale* calculations (top), and for DNS (bottom)

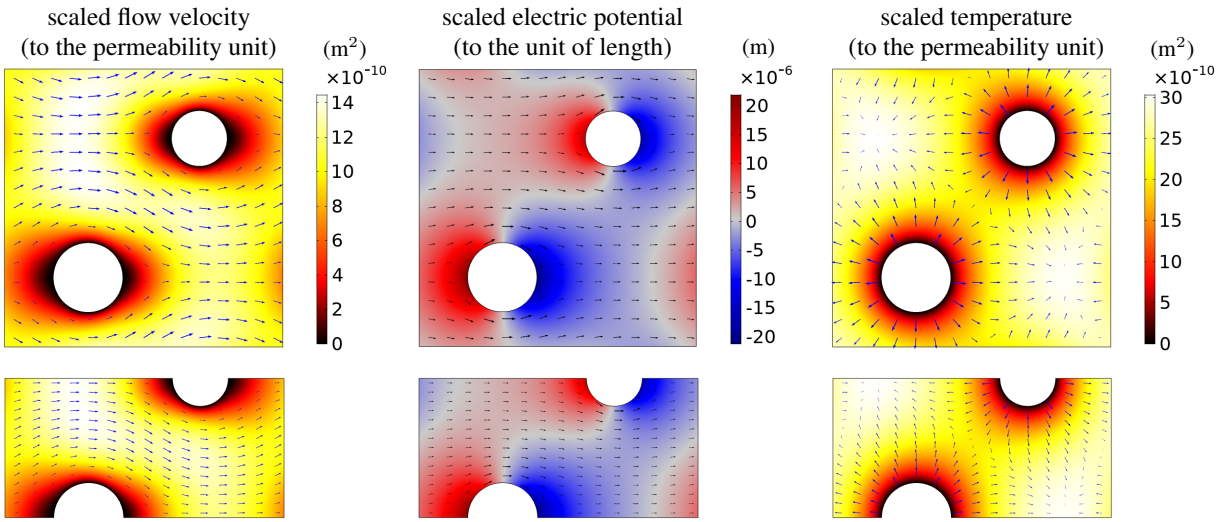

Figure 4: Fields of the scaled velocity projected onto $\mathbf{e}$, scaled electric potential, and scaled temperature for *Hybrid Multiscale* calculations of the fibrous material (the arrows show the velocity, electric field, and temperature gradient, respectively). Note that averaging the fields of scaled velocity and temperature gives the viscous and thermal permeability, respectively.

Table 5: Transport parameters for the periodic fibrous material

Transport parameter	Symbol	Unit	Value
(open) porosity	ϕ	%	91.950
(inertial) tortuosity	α_∞	–	1.0815
static viscous tortuosity	α_{0v}	–	1.2693
static thermal tortuosity	α_{0th}	–	1.1085
viscous permeability	$\mathcal{K}_0$	10^{-10}m^2	9.0799
thermal permeability	θ_0	10^{-9}m^2	1.9677
viscous length	Λ_v	10^{-4}m	1.3883
thermal length	Λ_{th}	10^{-4}m	2.6016

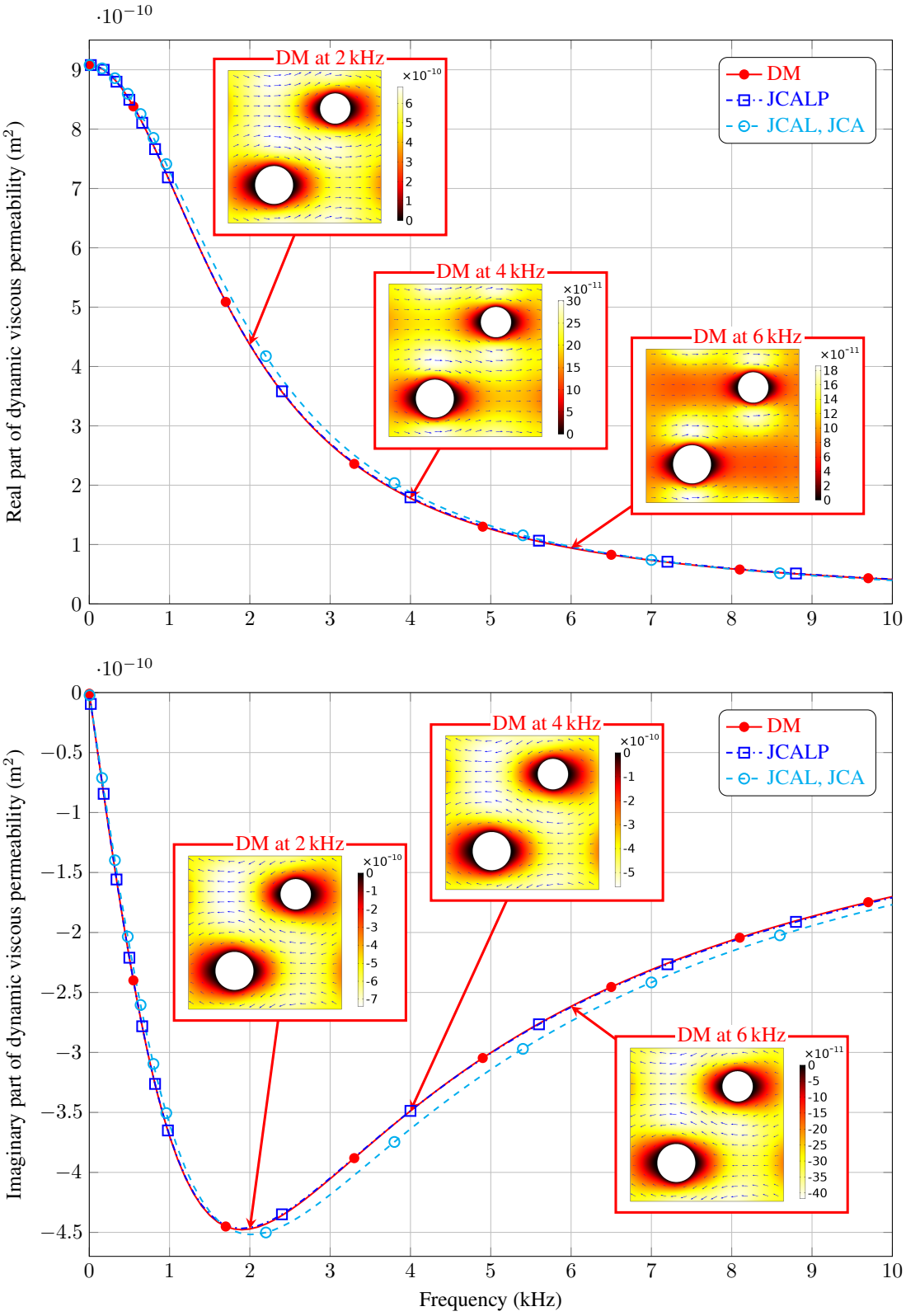

Figure 5: Dynamic viscous permeability for the periodic fibrous material: DM – *Direct Multiscale* computations; JCALP, JCAL, JCA – *Hybrid Multiscale* calculations with the specified model

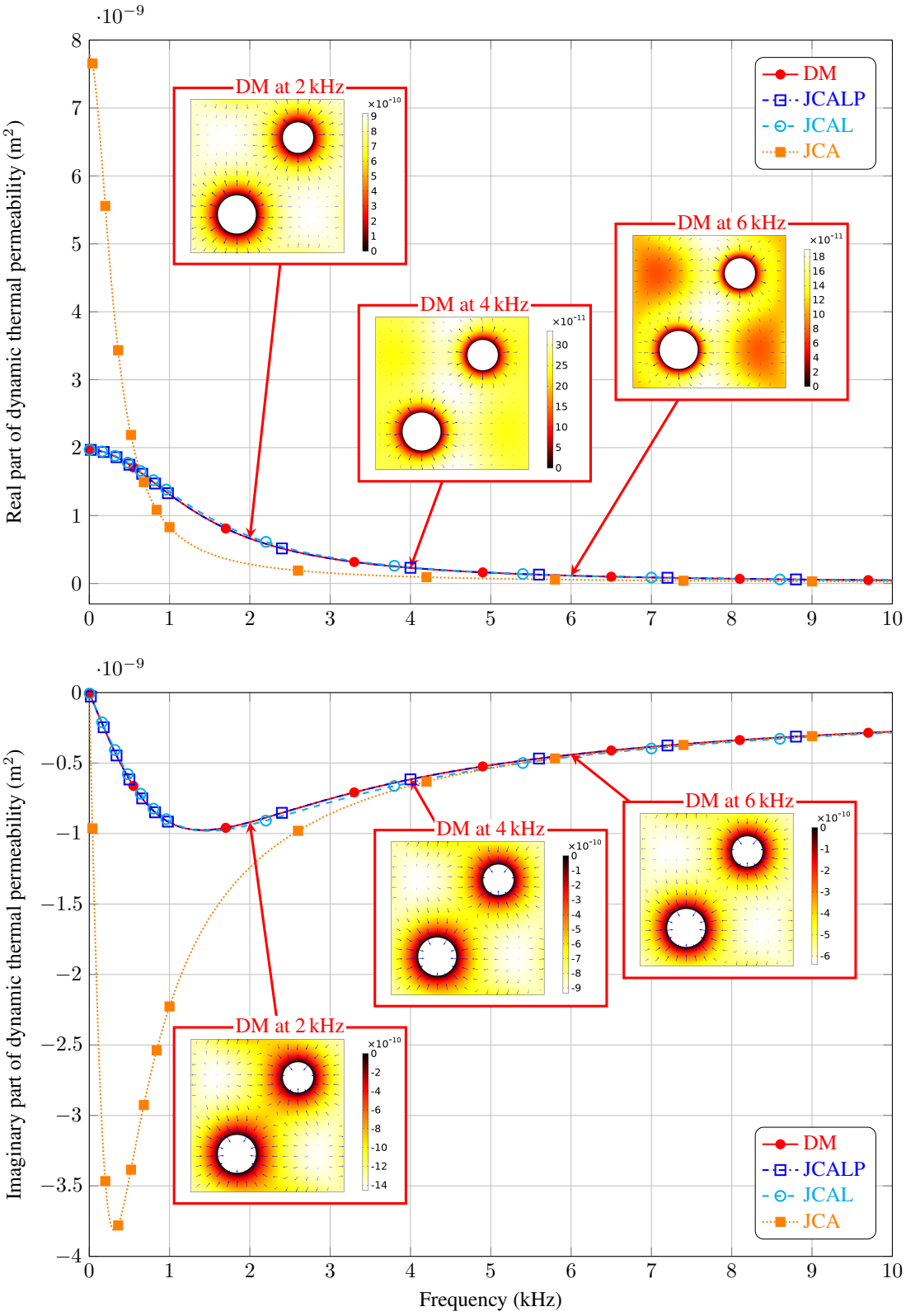

Figure 6: Dynamic thermal permeability for the periodic fibrous material: DM – *Direct Multiscale* computations; JCALP, JCAL, JCA – *Hybrid Multiscale* calculations with the specified model

some slightly coarser meshes not presented here. Note that the available analytical formulae for porosity, $\phi = 1 - \frac{\pi}{4}\left(D_1^2 + D_2^2\right)/\ell_c^2$, and characteristic length, $\Lambda_{\text{th}} = \left(\frac{4}{\pi}\ell_c^2 - D_1^2 - D_2^2\right)/\left(2D_1 + 2D_2\right)$, confirm exactly the corresponding numerical values obtained with a purely geometrical calculation.

The numerically-determined transport parameters were used for the analytical formulae for dynamic permeabilities (A.83) and dynamic tortuosities (A.79) and (A.81), accordingly to each of the three models (JCA, JCAL, and JCALP) recalled in Section A.2. These results of *Hybrid* calculations are compared in Figures 5–8 with their counterparts found using the *Direct Multiscale* (DM) approach (discussed in Section 2 and in Appendix A.2) and the same finite-element meshes shown in Figure 3. In particular, the dynamic permeabilities are compared in Figures 5 and 6, where also the relevant fields of direct calculations at particular frequencies of 2, 4, and 6 kHz are shown. Most of the results of *Hybrid* calculations are very similar (or nearly identical) to the DM results, however, there are significant discrepancies at lower frequencies in the case of the dynamic thermal permeability computed using the JCA model (see Figure 6). This discrepancy almost vanishes with the low-frequency correction of the thermal permeability parameter θ_0 introduced by Lafarge et al. [27] and used in the JCAL and JCALP models; here, note that the analytical estimation of thermal permeability $\phi\Lambda_{\text{th}}^2/8 = 7.78 \cdot 10^{-9}\,\text{m}^2$, which leads to the JCA model, is nearly 4 times larger than the correct value found numerically (see Table 5). To better visualise some other differences, the dynamic tortuosites are compared in Figures 7 and 8, where the DM results where determined from the directly-computed dynamic permeabilities using Eqs. (A.41) and (A.42). Notice especially the discrepancies of the real part of both dynamic tortuosities calculated using the JCAL model with respect to the corresponding (nearly identical) DM and JCALP results, and also small discrepancies at higher frequencies between the DM and JCALP calculations of the real part of dynamic viscous tortuosity (see top plot in Figure 7). We assume that the DM results may be used for reference, however, the frequency-dependent DM computations were carried out using

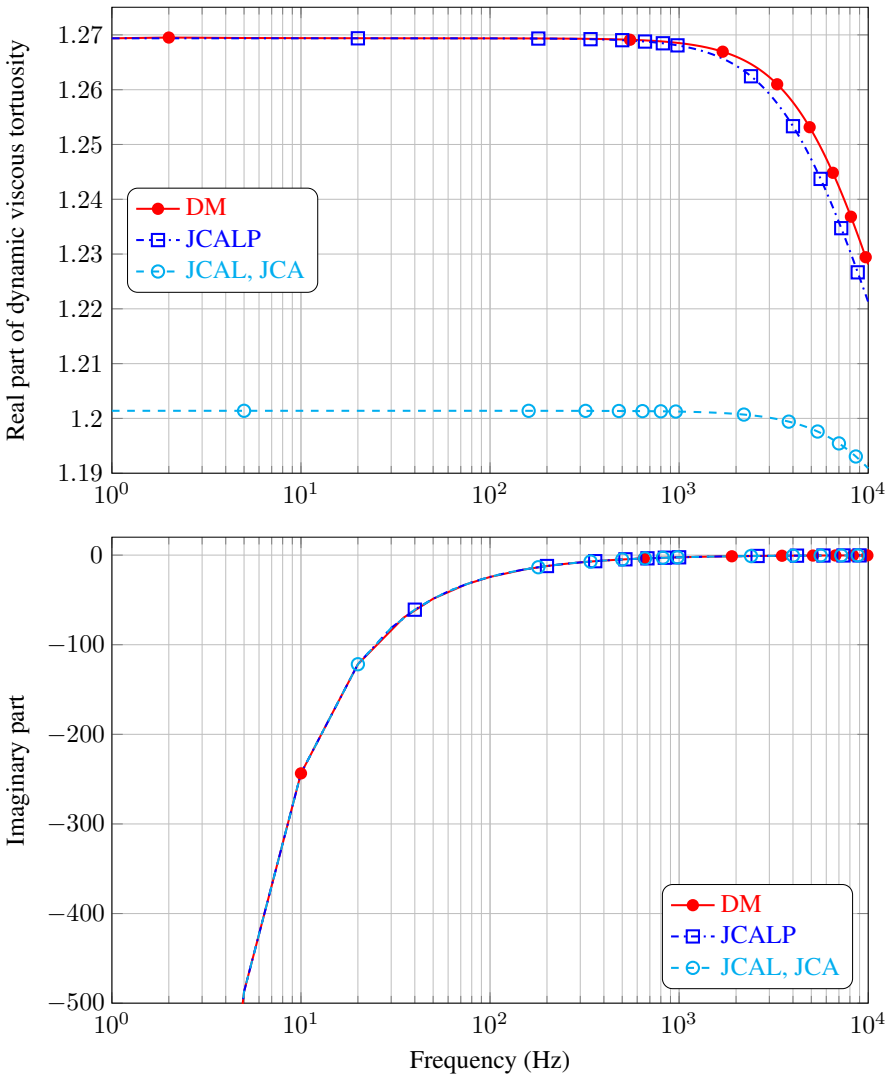

Figure 7: Dynamic viscous tortuosity for the periodic fibrous material: DM – *Direct Multiscale* computations; JCALP, JCAL, JCA – *Hybrid Multiscale* calculations with the specified model

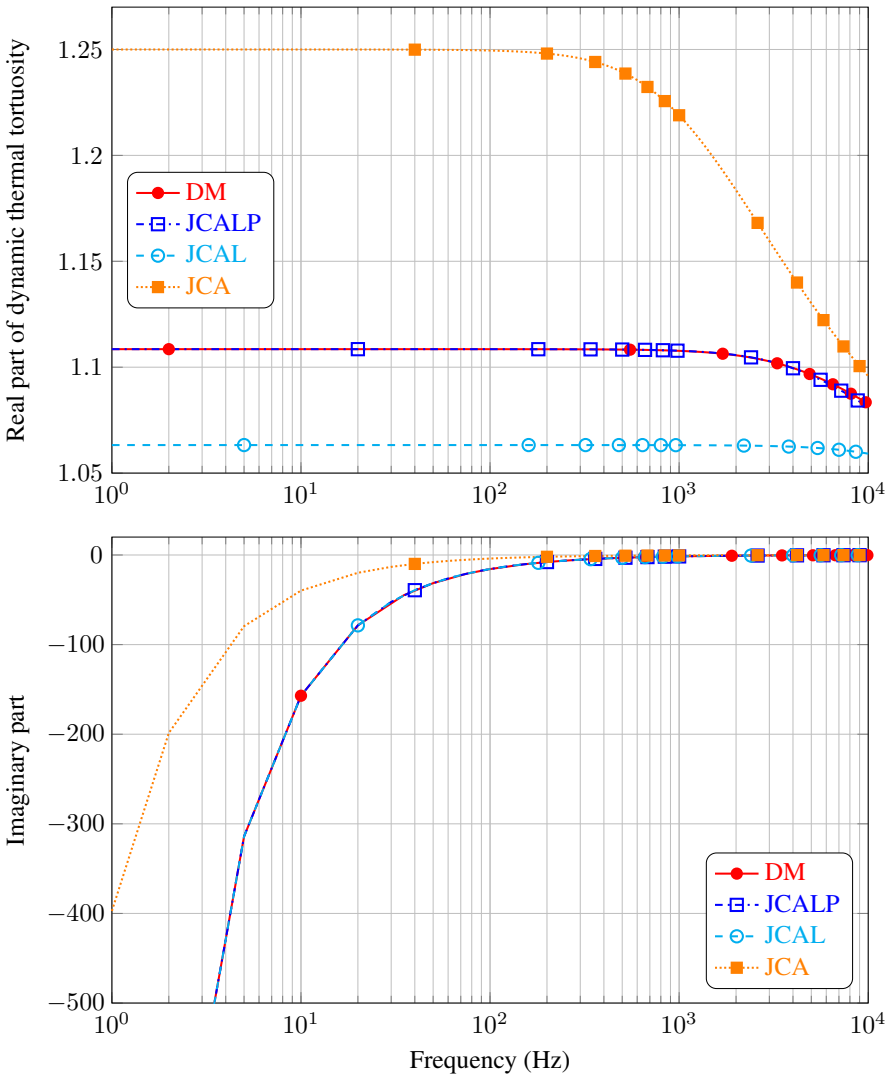

Figure 8: Dynamic thermal tortuosity for the periodic fibrous material: DM – *Direct Multiscale* computations; JCALP, JCAL, JCA – *Hybrid Multiscale* calculations with the specified model

always (i.e. for each computational frequency) the same finite-element mesh as the corresponding frequency-independent (i.e. static) computations of transport parameters used by *Hybrid* calculations.

The dynamic functions calculated for the periodic fibrous material were used to compute its effective properties, and finally the effective wave number (A.45), from which the wave speed and attenuation (A.47) were determined and plotted in Figure 9 for the relevant cases of calculation methods and models. Here, the discrepancies between various results are related to the ones discussed above, although they seem less pronounced. Note also that at higher frequencies, the waves in the fibrous material are only slightly (i.e. 80% to 90%) slower than the waves in the open air, however, they dramatically slow down below 2 kHz. The corresponding wavelengths are compared in Figure 10 to demonstrate that at lower frequencies these are much shorter than the wavelengths in the open air. Note, however, that even the shortest-considered wavelength ($\lambda_w \approx 30$ mm at 10 kHz) is still 150 times larger than the cell size ($\ell_c = 0.2$ mm), which ensures a very good separation of scales and the absence of scattering.

Figure 11 compares sound absorption coefficient spectra computed using various methods and models (as discussed in Section 2) for layers of the periodic fibrous material of different thickness $h = 10$ mm, 16 mm, and 24 mm, respectively. A close comparison of the absorption curves shows that the results of *Direct Multiscale* calculations (DM) are practically the same as the results obtained from *Direct Numerical Simulations* (DNS), and also nearly identical to the results of *Hybrid Multiscale* calculations using the JCALP model. If these results are used for reference, then small but noticeable discrepancies appear when the JCAL model is used, especially at higher frequencies above 2 or 3 kHz, while in the case of the JCA model much more significant discrepancies manifest themselves in the whole frequency range (especially for thinner layers), which proves the importance of the correction introduced by the thermal permeability parameter θ_0 for such fibrous materials. Note that for a particular method and model, the sound absorption coefficients are virtually the

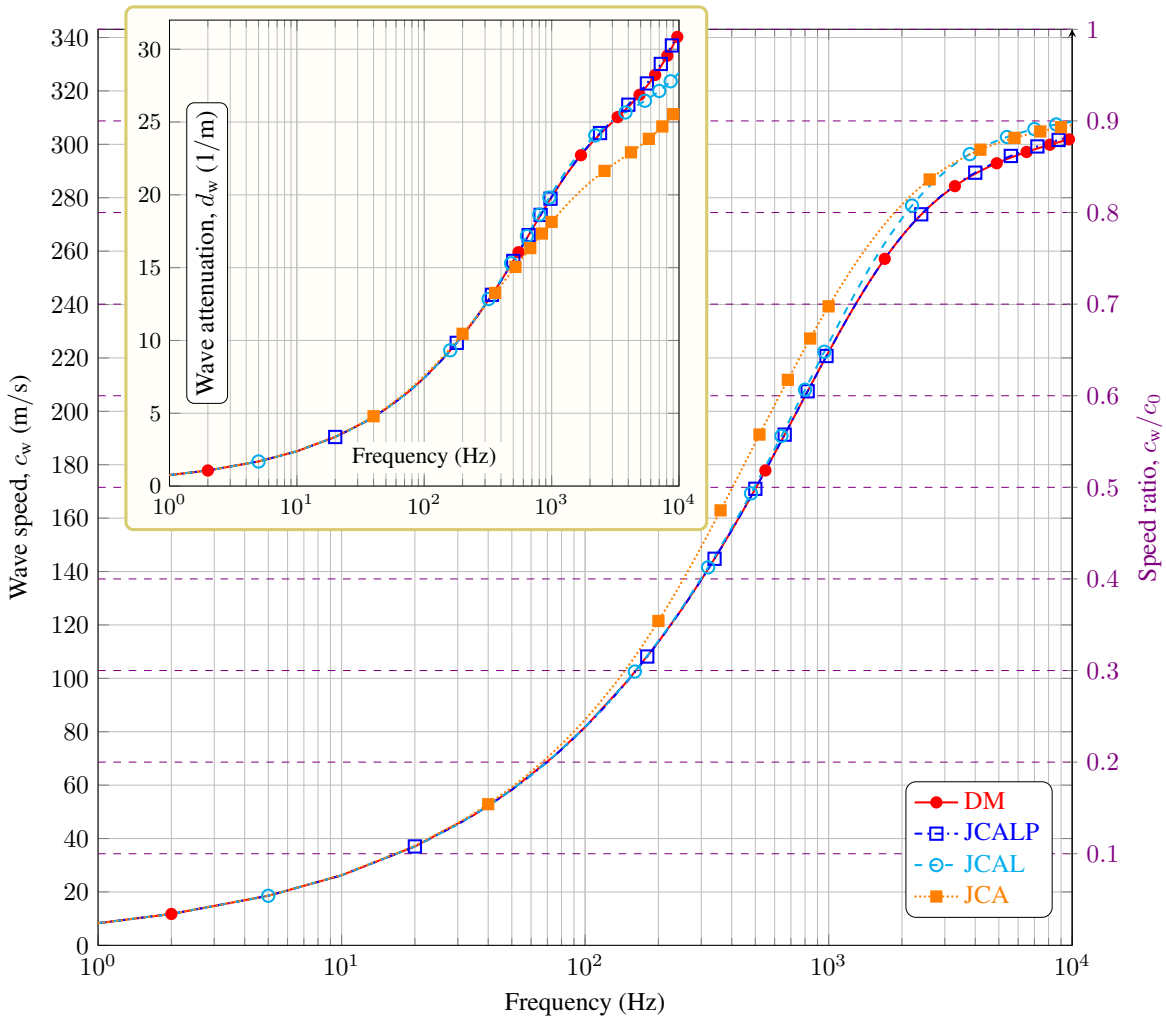

Figure 9: Wave speed and attenuation for the periodic fibrous material: DM – *Direct Multiscale* computations; JCALP, JCAL, JCA – *Hybrid Multiscale* calculations with the specified model

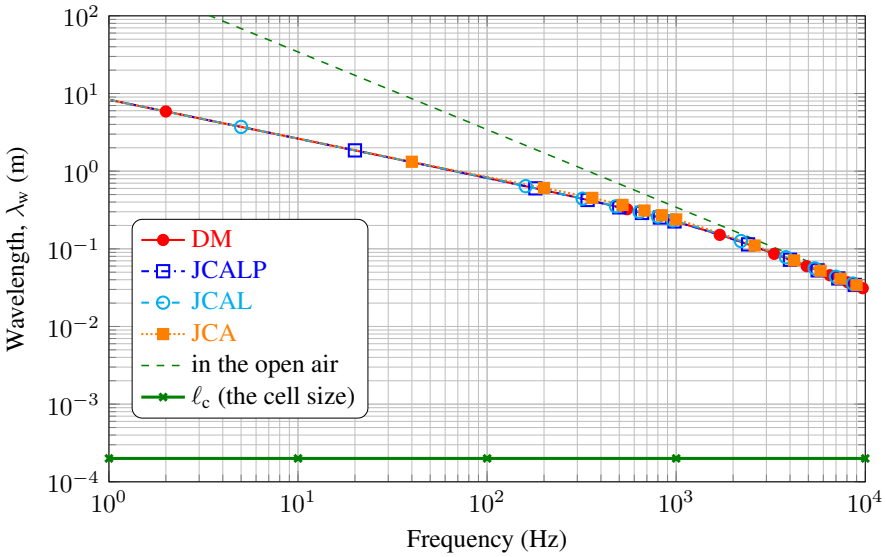

Figure 10: Wavelength for the periodic fibrous material (and in the open air): DM – *Direct Multiscale* computations; JCALP, JCAL, JCA – *Hybrid Multiscale* calculations with the specified model

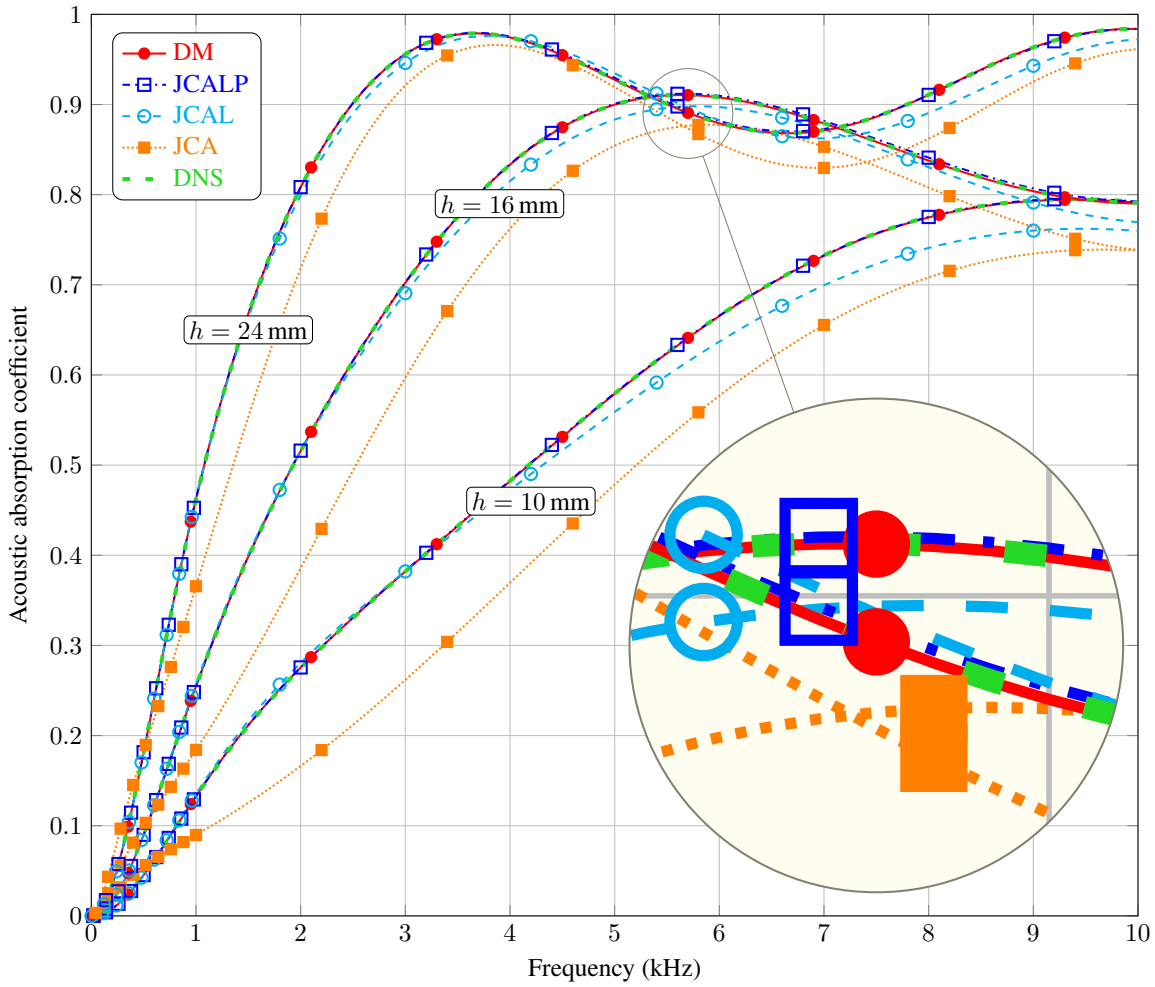

Figure 11: Sound absorption for the rigidly-backed fibrous layers (of the specified thickness h): DM – *Direct Multiscale* computations; JCALP, JCAL, JCA – *Hybrid Multiscale* calculations with the specified model; DNS – *Direct Numerical Simulation*

same when they are computed on the face of the fibrous layer (with a certain thickness h) or anywhere inside the adjacent layer of air, because the wave propagation in the air layer is lossless. This was also confirmed in the case of DNS (see Figure 2 and the finite-element mesh at the bottom of Figure 3), for which the surface impedances $Z_\mathrm{s}(\omega)$ computed (for each frequency) using values of the pressure and normal velocity averaged over the interface EF (or even CD) or the boundary GH, respectively, were obviously different, but the final results of the acoustic absorption coefficient, calculated from Eq. (1), were practically the same.

3.2 BENCHMARK 2: A regular periodic foam with identical spherical pores in overlapped cubic packing

Figure 12 shows the Representative Elementary Volume of a very regular foam with identical spherical pores. The pores are set in a cubic packing and they overlap, so that the porosity is fully open. The assumed size of the cubic REV is $\ell_\mathrm{c} = 0.20\,\mathrm{mm}$, and the spherical pore diameter is $R_\mathrm{p} = 0.55\,\ell_\mathrm{c} = 0.11\,\mathrm{mm}$, which results in a porosity of 67.18%. The REV is fully symmetric so that the porous material is structurally isotropic having the same macroscopic properties for any direction $\mathbf{e}$. For the micro-scale computations, we assume that $\mathbf{e}$ is along the y_1-axis and divide the periodic REV into 16 and 48 symmetrical sections, as presented in Figure 12, in order to take advantage of the geometrical symmetry. The division into 16 sections is for problems that depend on the direction $\mathbf{e}$ (i.e. the Stokes flow, Laplace's problem, and harmonic viscous flow), while the division into 48 sections is for fully-symmetric direction-independent problems (i.e. the Poison's problem and harmonic thermal diffusion). In the first case, instead of using the whole periodic REV one can perform direction-dependent computations on one of the $1/16$-th sections by applying the symmetric boundary conditions on all its fluid faces parallel to the direction $\mathbf{e}$, and the antisymmetric boundary conditions on the remaining two fluid faces perpendicular to $\mathbf{e}$ (see Figure 13). In the case of the direction-independent problems any of the $1/48$-th sections can serve as the computational domain with the symmetric boundary conditions applied on all fluid faces (see Figure 13).

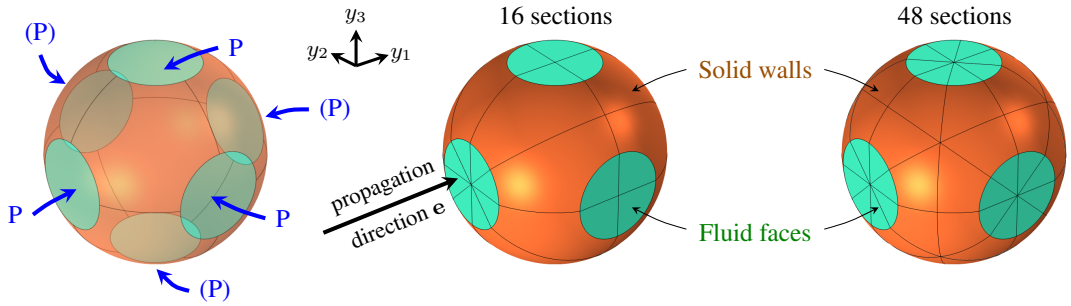

Figure 12: Fluid domain inside the cubic periodic porous cell (i.e. REV of the size ℓ_c) with a single spherical pore (radius $R_p = 0.55\,\ell_c$) and its partitioning based on the symmetry; the symbol P means periodic boundary conditions applied on the corresponding fluid faces; the parentheses around this symbol indicates that the fluid face is on the back of the pore (visible only for transparency)

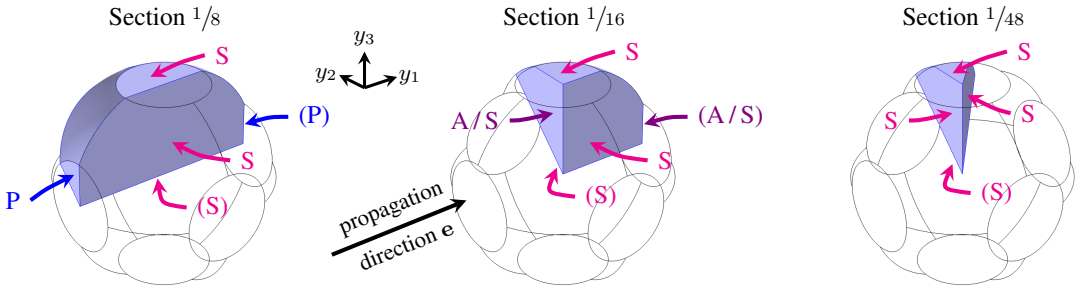

Figure 13: Symmetric sections of the periodic REV and the faces of: S – symmetry, and P – periodicity; the parentheses around the symbols mark that the fluid face is invisible (i.e. at the back of the section); A / S means that the antisymmetric boundary condition is applied in the case of Stokes flow, harmonic viscous flow, or Laplace's problem driven in the direction y_1, while the symmetric condition is applied in the case of Poisson's problem or harmonic thermal diffusion; note that because of the symmetry, P can be conveniently replaced by A / S; the smallest ($^1/_{48}$) section may serve only in direction-independent analyses, i.e. the Poisson's problem and harmonic thermal diffusion

This smallest possible symmetrical section cannot be used for the direction-dependent problems. On the other hand, the Poisson's and harmonic thermal diffusion problems can be solved on the larger $^1/_{16}$-th section by applying the symmetric boundary conditions on all fluid faces. Finally, all problems can be solved on the $^1/_8$-th section depicted in Figure 13, by applying the symmetric boundary conditions on all faces parallel to $\mathbf{e}$, and periodic continuity conditions on the two remaining faces, although (because of the symmetry) the conditions of periodicity can be also conveniently replaced with the antisymmetric boundary conditions in the case of the direction-dependent analyses, or with the symmetric ones in the case of the direction-independent analyses.

Here, we specify the symmetric boundary conditions for each of the relevant computational problems. The fluid does not flow through the plane of symmetry which means that in the case of the scaled Stokes flow (A.70)–(A.71) we must set on each symmetry face the no-penetration condition $\hat{\mathbf{k}}_0 \cdot \mathbf{n} = 0$, which in the case of the scaled harmonic flow (A.34)–(A.35) is $\hat{\mathbf{k}} \cdot \mathbf{n} = 0$, where $\mathbf{n}$ is the unit vector normal to the symmetry plane. In the case of the Laplace's equation (A.58), related to the scaled problem of electric conduction, the condition on the symmetry plane is $\nabla_y q \cdot \mathbf{n} = 0$, which is also related to the fact that the (scaled) electric field (A.55) is tangent to the symmetry plane, namely, $\mathbf{E} \cdot \mathbf{n} = \mathbf{e} \cdot \mathbf{n} - \nabla_y q \cdot \mathbf{n} = 0$, and here, $\mathbf{e} \cdot \mathbf{n} = 0$, because all symmetry planes are parallel to the direction $\mathbf{e}$ of the external uniform electric field (see Figure 13). Finally, in the case of the Poisson's equation (A.75), or the scaled equation of harmonic thermal diffusion (A.38), there is no (heat) flux through the symmetry planes (like in thermal insulation), namely, $\nabla_y \tilde{\theta}_0 \cdot \mathbf{n} = 0$, or respectively, $\nabla_y \tilde{\theta} \cdot \mathbf{n} = 0$.

Antisymmetric boundary conditions are relevant only for the direction-dependent problems: for the (scaled) Stokes flow and harmonic (oscillatory) viscus flow, and for the Laplace's problem. In order to discuss them, let us introduce two unit vectors $\mathbf{t}^{(1)}$ and $\mathbf{t}^{(2)}$, which are *not* collinear, but both are tangent to the considered plane of antisymmetry, i.e. $\mathbf{t}^{(1)} \cdot \mathbf{n} = \mathbf{t}^{(2)} \cdot \mathbf{n} = 0$, where $\mathbf{n}$ is the unit vector normal to the antisymmetry plane; note also that for any antisymmetric face, $\mathbf{n}$ is collinear with $\mathbf{e}$ (see Figure 13). Antisymmetry requires that there is no tangential flow along the antisymmetric faces, or in other words, the velocity projection on the antisymmetry plane is zero, i.e. $\mathbf{v}^{(0)} \cdot \mathbf{t}^{(1)} = \mathbf{v}^{(0)} \cdot \mathbf{t}^{(2)} = 0$, which in the case of the scaled Stokes flow (A.70)–(A.71) means that $\hat{\mathbf{k}}_0 \cdot \mathbf{t}^{(1)} = \hat{\mathbf{k}}_0 \cdot \mathbf{t}^{(2)} = 0$, and in the case of the scaled harmonic flow (A.34)–(A.35), similarly, $\hat{\mathbf{k}} \cdot \mathbf{t}^{(1)} = \hat{\mathbf{k}} \cdot \mathbf{t}^{(2)} = 0$. Additionally, the local pressure and normal stresses on the antisymmetry plane are zero, i.e. $p^{(1)} = 0$ and $\underline{\underline{\boldsymbol{\sigma}}}^{(0)} \cdot \mathbf{n} = \mathbf{0}$; here, the stress tensor $\underline{\underline{\boldsymbol{\sigma}}}^{(0)}$ (not to be confused with the flow resistivity tensor $\underline{\underline{\boldsymbol{\sigma}}}$) is defined as $\underline{\underline{\boldsymbol{\sigma}}}^{(0)} = \underline{\underline{\boldsymbol{\tau}}}^{(0)} - p^{(1)}\underline{\underline{\mathbf{I}}}$, where $\underline{\underline{\boldsymbol{\tau}}}^{(0)} = 2\eta\,\underline{\underline{\dot{\boldsymbol{\varepsilon}}}}(\mathbf{v}^{(0)})$ is the shear stress tensor (i.e.

the stress deviator) and $\underline{\underline{\dot{\boldsymbol{\varepsilon}}}}(\mathbf{v}^{(0)}) = \frac{1}{2}\left(\nabla_y \mathbf{v}^{(0)} + \nabla_y^{\mathrm{T}} \mathbf{v}^{(0)}\right)$ is the rate of strain (i.e. the symmetric part of the gradient of velocity). Note that, since the local pressure is zero on the antisymmetry plane, the zero normal stress condition can be equivalently rewritten as $\underline{\underline{\boldsymbol{\tau}}}^{(0)} \cdot \mathbf{n} = \mathbf{0}$ or $\underline{\underline{\dot{\boldsymbol{\varepsilon}}}} \cdot \mathbf{n} = \mathbf{0}$, and it simply means that inside the weak integral formulations of the corresponding (oscillatory, stationary, or scaled) flow problems, the relevant surface integral which involves the term $\underline{\underline{\dot{\boldsymbol{\varepsilon}}}}(\mathbf{v}^{(0)}) \cdot \mathbf{n}$ (or its scaled equivalent) is zero on the plane of antisymmetry, and thus, the surface integral vanishes in practice on the antisymmetric boundaries. On the other hand, the condition $p^{(1)} = 0$ must be explicitly set on the planes of antisymmetry as an additional constraint for the local pressure field, and in the case of the scaled flow problems (A.70)–(A.71) or (A.34)–(A.35), it means that the corresponding scaled pressure is zero, i.e. $\hat{\pi}_0 = 0$ or $\hat{\pi} = 0$, respectively, on each plane of antisymmetry. Finally, in the case of the Laplace's equation (A.58), the antisymmetric boundary condition is $q = 0$. Note also that from this condition results what follows: the potential q is constant on the antisymmetric face so that the projection of its gradient onto this plane is zero, i.e. $\nabla_y q \cdot \mathbf{t}^{(1)} = \nabla_y q \cdot \mathbf{t}^{(2)} = 0$, and since for antisymmetric faces $\mathbf{e} \cdot \mathbf{t}^{(1)} = \mathbf{e} \cdot \mathbf{t}^{(2)} = 0$, then, as expected, the projection of the scaled electric field (A.55) onto the antisymmetric plane is also zero, i.e. $\mathbf{E} \cdot \mathbf{t}^{(1)} = \mathbf{E} \cdot \mathbf{t}^{(2)} = 0$.

The representative periodic geometry shown in Figures 12 and 13 can be easily reconstructed, however, it has sharp edges all around the windows connecting the pores. These sharp edges may cause serious computational problems, especially, when computing the viscous characteristic length Λ_{v}, because the (scaled electric) potential q is not smooth in the vicinity of a sharp edge, and $\mathbf{E}$, being a function of the gradient of q, may be there very singular [77]. In formula (A.68) for Λ_{v} one actually integrates the term $\mathbf{E}\cdot\mathbf{E}$ over the whole solid surface, and when this surface has sharp edges one cannot easily get rid of this singularity, which entails a problem with mesh independence, no matter how dense the finite element mesh around the sharp edges is.

To ensure a numerical convergence for all transport parameters the sharp edges can be replaced by small smooth fillets with radius R_{F} much smaller than the radii of pores and windows. In Appendix B we present how to add fillets with *smooth* inflection points to the periodic porous microstructure used here for benchmark calculations. We also provide all necessary data for accurate reconstruction of such geometry, as well as formulae for analytical calculations of important geometric parameters, such as porosity, surface of solid walls inside the periodic REV, and filleted window radius. In the benchmark calculations we used the geometry without fillets for DNS and DM computations, where the Laplace's problem is not solved so there is no convergence problem. For HM calculations we used fillets with a radius 200 times smaller than the pore radius, however, for comparison we also present the values of transport parameters computed for larger fillet radii, namely, when the ratio $R_{\mathrm{p}}/R_{\mathrm{F}}$ equals to 100 and 50.

Figure 14 presents finite-element meshes that were used in micro-scale computations for the regular periodic foam (for fillets with different sizes, i.e. $R_{\mathrm{F}} = R_{\mathrm{p}}/50$, $R_{\mathrm{p}}/100$, and $R_{\mathrm{p}}/200$, as well as with sharp edges). Typically, the meshes were constructed as follows. First, triangular elements were generated on the solid boundary (including fillets); the maximum triangular element size for the fillets was $\frac{\ell_{\mathrm{c}}}{8R_{\mathrm{p}}/R_{\mathrm{F}}}$ (e.g. it was $\frac{\ell_{\mathrm{c}}}{400}$ for $R_{\mathrm{F}} = R_{\mathrm{p}}/50$), while for the remaining solid surface it was set to $\frac{\ell_{\mathrm{c}}}{80}$. Then, tetrahedral elements were generated over the whole fluid domain with the maximum element size set to $\frac{\ell_{\mathrm{c}}}{40}$. Additionally, the minimal element size was set equal to the maximum element size assigned for the fillet surfaces. Such approach allowed for an efficient distribution of the degrees of freedom. Finally, some meshes were enriched with boundary layers generated along the solid surface. Note that the finite element meshes on the $1/8$-th section are symmetric with respect to the middle plane, because they were constructed from the mesh generated on the $1/16$-th section using a mirror copy operation. Table 6 lists the numbers of elements for each of the meshes used in the REV-based

Table 6: Numbers of elements (in the computational domain, on its surfaces and edges) and degrees of freedom (DoF in various types of analyses) for all cases of finite element meshes generated for the regular periodic foam

Mesh case (section type)	3D elements	2D elements	1D elements	DoF in SF or HVF	DoF in LP, PP, HTD	HVF	SF	LP	PP	HTD
R/50# (1/8)	476 795	18 749	446	2 429 392	847 583	○	●	●	●	○
R/50# (1/16)	279 011	17 102	752	1 217 618	424 687	○	●	●	●	○
R/50 (1/16)	352 107	20 006	792	2 150 250	734 591	○	●	●	●	○
R/50 (1/48)	524 386	17 502	516		751 808	×	×	×	●	○
R/100 (1/16)	765 107	36 732	1 252	4 621 785	1 562 906	○	●	●	●	○
R/200 (1/16)	1 570 599	69 172	2 136	8 560 125	2 889 481	○	●	●	●	○
R/∞ (1/8)	121 088	10 464	404	537 489	194 203	○	●	!	●	○
R/∞ (1/16)	60 544	5 420	231	270 070 *	97 507 *	●	●	!	●	●
R/∞ (1/48)	547 314	25 072	557		805 602 *	×	×	×	●	●

Numerical analyses: ● – computed, ○ – possible, × – not applicable, *complex DoF in HVF and HTD
! – singularity at sharp edges causes computational problems (Λ_{v} is mesh-dependent);
HVF – harmonic viscous flow, SF – Stokes flow, LP – Laplace's problem,
PP – Poisson's problem, HTD – harmonic thermal diffusion.

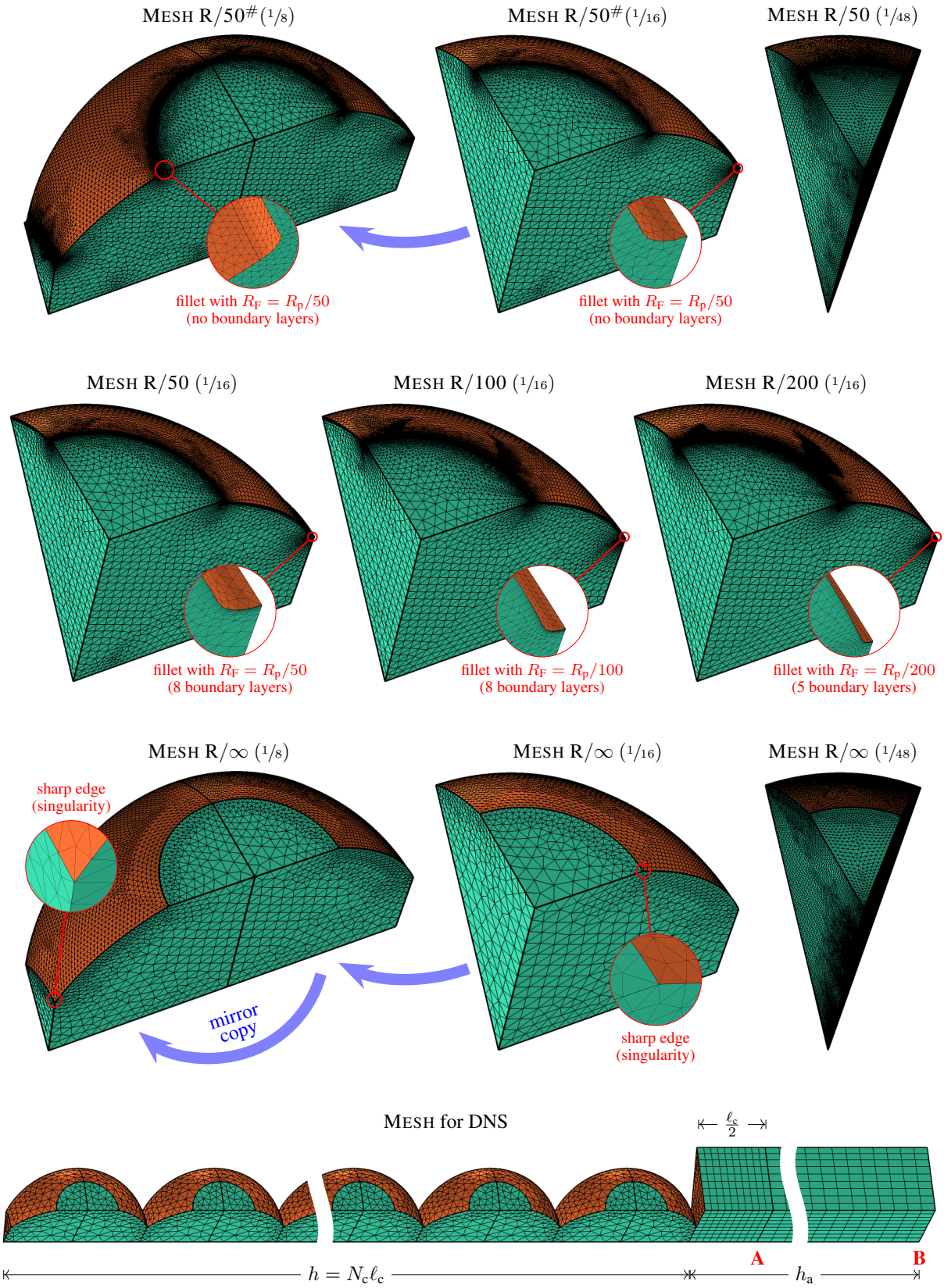

Figure 14: Finite element meshes on sections of the fluid domain of the REV of regular periodic foam, and the finite element mesh used for DNS

calculations, as well as the numbers of degrees of freedom (DoF) related to particular mesh cases and numerical analyses. For convergence tests even denser meshes were generated with the minimal element size smaller than the one specified above, which also allowed for denser meshing on fillets. However, the results obtained for these meshes were virtually the same as the ones found using the coarser meshes shown in Figure 14, which proved a very good convergence.

Numerical analyses for *Multiscale* calculations were carried out using various FE meshes as shown in Table 6. The field results of static analyses (for the fillet with radius $R_F = R_p/50$), obtained using MESH R/50 ($1/8$) and MESH R/50 ($1/16$), are shown in Figures 15 and 16, as well as in Figure 17, where the results of computations based on MESH R/50 ($1/48$) are also presented. As expected, the same results were obtained from the corresponding meshes of the $1/16$-th and $1/8$-th sections, and also for the $1/48$-th section in the case of the Poisson's problem. The corresponding field results obtained for the cases with smaller fillets were very similar to the ones presented in Figures 15–17. The meshes with fillets were used only for the static analyses, while MESH R/∞ ($1/16$) served for all static and both dynamic (oscillatory) analyses, however, as anticipated, in the case of the Laplace's problem the singularity at the sharp edges did not allow the viscous characteristic length (even when trying extremely dense mesh cases). MESH R/∞ ($1/8$) served for the Poisson's analysis and the oscillatory thermal diffusion problem. Finally, MESH for DNS was constructed on N_c successive pairs of the $1/16$-th section (without fillets) and its mirror copy, forming a fluid domain with thickness $h = N_c \ell_c$, with an adjacent layer with thickness $h_a = 5\ell_c = 1$ mm, as depicted at the bottom of Figure 14. Two cases were considered: (1) $N_c = 50$, $h = 10$ mm, and (2) $N_c = 100$, $h = 20$ mm.

The static solutions were used to determine the transport parameters for the regular periodic foam (with fillets). Recall that calculations of transport parameters involve averaging over the periodic fluid domain Ω_f. However, when Ω_f is symmetric with respect to one or more symmetry planes, FE computations should be conducted on subdomains Ω_f^{sub} (the smallest possible), resected from Ω_f by the symmetry (and antisymmetry) planes, as demonstrated in this benchmark example. Now, let us define the averaging operator over a fluid subdomain Ω_f^{sub}, i.e.: $\langle\cdot\rangle_{fsub} = \dfrac{1}{\Omega_f^{sub}} \displaystyle\int_{\Omega_f^{sub}} (\cdot)\, d\Omega$. Because of the symmetry, the integrations over Ω_f (and over its solid surface) can be replaced by the integrations over Ω_f^{sub} (and over its solid surface) in the formulae (A.68) and (A.69) for Λ_v and Λ_{th}, respectively, while the averaging over Ω_f can be replaced by the averaging over Ω_f^{sub} in the formulae (A.73), (A.77), (A.78), and (A.65), for $\mathcal{K}_0$, θ_0, α_{0th}, and α_∞, respectively. However, in the case of formula (A.74) for α_{0v}, and Eqs. (A.66) and (A.67) for α_∞, such substitution is not valid for the $1/16$-th section of the REV used in this benchmark example (i.e. for subdomains set between two successive planes of antisymmetry), since for such subdomains $\left\langle \hat{\mathbf{k}}_0 \right\rangle_{fsub} \neq \left\langle \hat{\mathbf{k}}_0 \right\rangle_f$ and $\langle \mathbf{E} \rangle_{fsub} \neq \langle \mathbf{E} \rangle_f$. Ignoring this may lead to

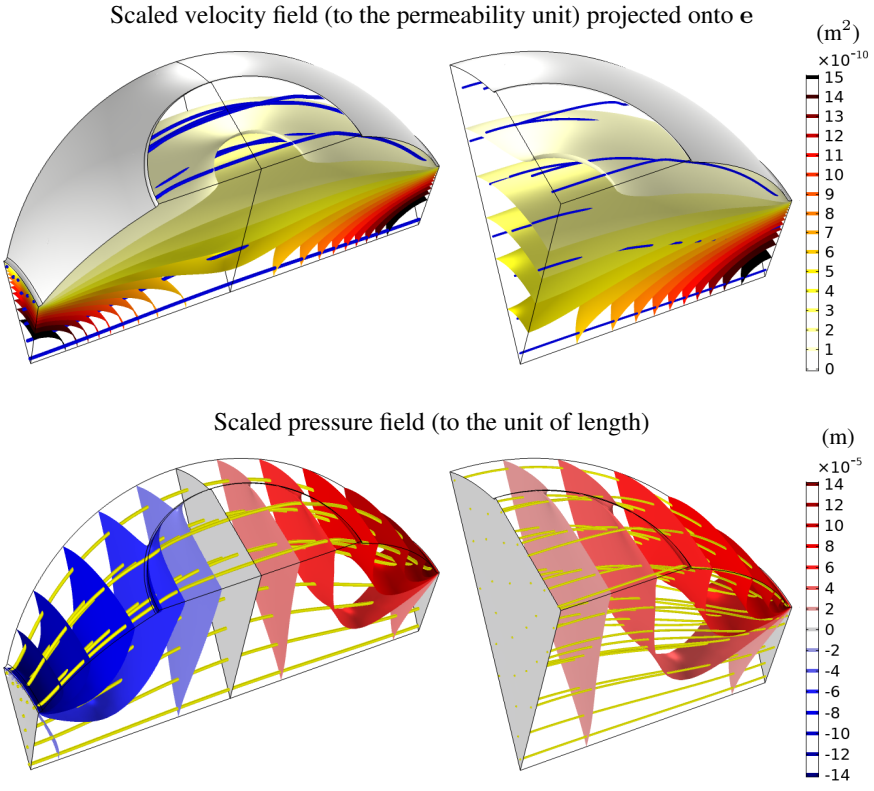

Figure 15: Results of the scaled problems of Stokes flow for the regular periodic foam

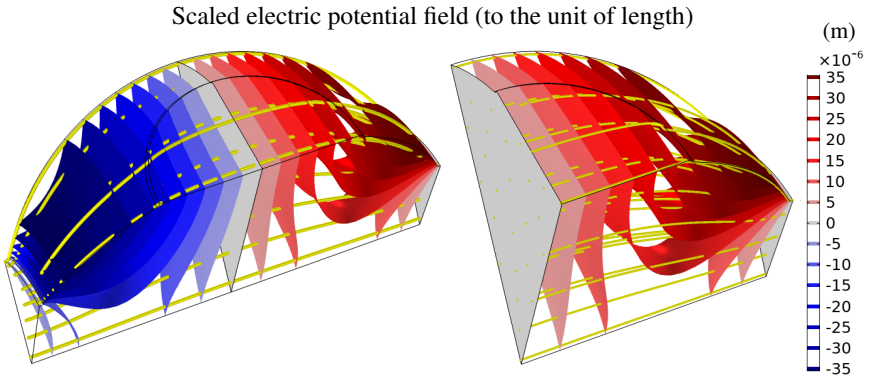

Figure 16: Results of the Laplace's analyses for the regular periodic foam

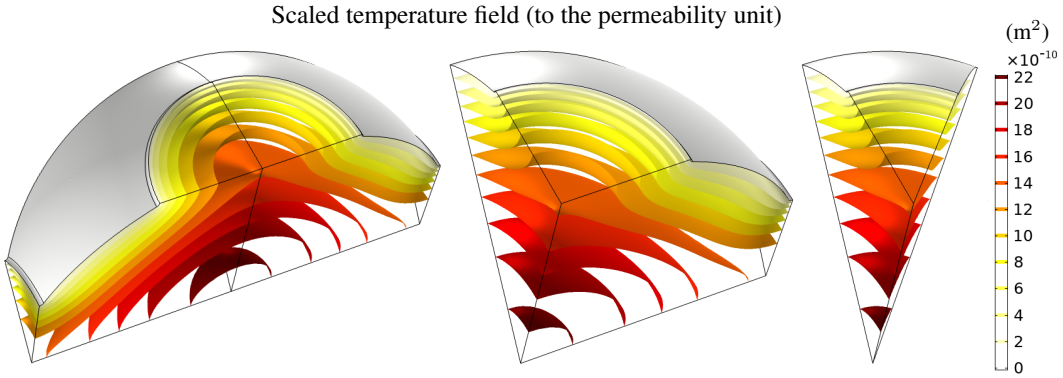

Figure 17: Results of the Poisson's analyses for the regular periodic foam

serious errors. On the other hand, for fluid domains with antisymmetric field solutions of the Stokes flow and Laplace's problem (see, e.g. Figures 15 and 16), the components of $\hat{\mathbf{k}}_0$ and $\mathbf{E}$ perpendicular to $\mathbf{e}$ cancel out in averaging, so that $\left\langle \hat{\mathbf{k}}_0 \right\rangle_{\mathrm{f}} \cdot \left\langle \hat{\mathbf{k}}_0 \right\rangle_{\mathrm{f}} = \left\langle \hat{\mathbf{k}}_0 \cdot \mathbf{e} \right\rangle_{\mathrm{f}}^2 = \left\langle \hat{\mathbf{k}}_0 \cdot \mathbf{e} \right\rangle_{\mathrm{fsub}}^2$ and $\langle \mathbf{E} \rangle_{\mathrm{f}} \cdot \langle \mathbf{E} \rangle_{\mathrm{f}} = \langle \mathbf{E} \cdot \mathbf{e} \rangle_{\mathrm{f}}^2 = \langle \mathbf{E} \cdot \mathbf{e} \rangle_{\mathrm{fsub}}^2$, which means that the formulae (A.74) and (A.67) in such cases can be replaced by

$$\alpha_{0\mathrm{v}} = \frac{\left\langle \hat{\mathbf{k}}_0 \cdot \hat{\mathbf{k}}_0 \right\rangle_{\mathrm{f}}}{\left\langle \hat{\mathbf{k}}_0 \cdot \mathbf{e} \right\rangle_{\mathrm{f}}^2} = \frac{\left\langle \hat{\mathbf{k}}_0 \cdot \hat{\mathbf{k}}_0 \right\rangle_{\mathrm{fsub}}}{\left\langle \hat{\mathbf{k}}_0 \cdot \mathbf{e} \right\rangle_{\mathrm{fsub}}^2}, \qquad \alpha_\infty = \frac{\langle \mathbf{E} \cdot \mathbf{E} \rangle_{\mathrm{f}}}{\langle \mathbf{E} \cdot \mathbf{e} \rangle_{\mathrm{f}}^2} = \frac{\langle \mathbf{E} \cdot \mathbf{E} \rangle_{\mathrm{fsub}}}{\langle \mathbf{E} \cdot \mathbf{e} \rangle_{\mathrm{fsub}}^2}, \tag{3}$$

where it has been assumed that $\|\mathbf{e}\| = 1$ (otherwise, simply substitute $\frac{\mathbf{e}}{\|\mathbf{e}\|}$ for $\mathbf{e}$ in the expressions above), while Eq. (A.66) transforms into the first formula in (A.65). Finally, for (larger) symmetric subdomains like the $1/8$-th section of the REV used in this benchmark example (i.e. with the plane of antisymmetry in the middle) the substitution of $\langle \cdot \rangle_{\mathrm{fsub}}$ in place of $\langle \cdot \rangle_{\mathrm{f}}$ is valid also for Eqs. (A.66), (A.67), and (A.74).

The values of transport parameters for the regular periodic foams (with fillets of three different sizes), computed from FE solutions based on various mesh cases, are shown in Table 7 with an accuracy to 5 significant digits (4 significant digits

Table 7: Transport parameters for the regular periodic foam with fillets

Mesh case	ϕ (%)	α_∞ (–)	$\alpha_{0\mathrm{v}}$ (–)	$\alpha_{0\mathrm{th}}$ (–)	$\mathcal{K}_0$ (m^2)	θ_0 (m^2)	Λ_{v} (m)	Λ_{th} (m)
R/50$^\#$	67.222	1.5106	2.1554	1.3000	$1.8757 \cdot 10^{-10}$	$7.1188 \cdot 10^{-10}$	$5.306 \cdot 10^{-5}$	$1.0059 \cdot 10^{-4}$
R/50	67.228	1.5108	2.1558	1.3000	$1.8750 \cdot 10^{-10}$	$7.1195 \cdot 10^{-10}$	$5.308 \cdot 10^{-5}$	$1.0059 \cdot 10^{-4}$
R/100	67.191	1.5348	2.2085	1.3048	$1.7459 \cdot 10^{-10}$	$7.0231 \cdot 10^{-10}$	$4.981 \cdot 10^{-5}$	$9.8914 \cdot 10^{-5}$
R/200	67.181	1.5468	2.2375	1.3072	$1.6805 \cdot 10^{-10}$	$6.9789 \cdot 10^{-10}$	$4.741 \cdot 10^{-5}$	$9.8061 \cdot 10^{-5}$

The *linear* geometry shape order was used for the mesh case R/50$^\#$, while the *quadratic* one in all other cases. Note that in the latter cases the numerical values for ϕ and Λ_{th} are virtually equal to the analytical results.

in the case of Λ_v). The linear geometry shape order was used for MESH R/50$^{\#}$. In the case of quadratic shape order, the results were virtually the same as for MESH R/50, though this latter mesh contains boundary layers. When the quadratic shape order was used for geometry (as it was for the remaining mesh cases), the purely geometric parameters (ϕ and Λ_{th}) were calculated accurately with assumed accuracy (cf. with Table B.1 in Appendix B). Moreover, the convergence tests proved also the correctness of the values found for the other transport parameters. To get such accuracy when using the linear geometry shape order, the mesh density must be increased on the curved surfaces, leading to larger numbers of degrees of freedom. The values of transport parameters found for the case without fillets are not given in Table 7, but they were close to the values shown in the last row and computed for the smallest fillet (i.e. with radius $R_F = R_p/200$), although with the exception of Λ_v, which did not converge at all, and in an extreme case of a very fine meshing around the sharp edges its value even reached a value of more than 10% smaller than the radius of the window connecting the pores.

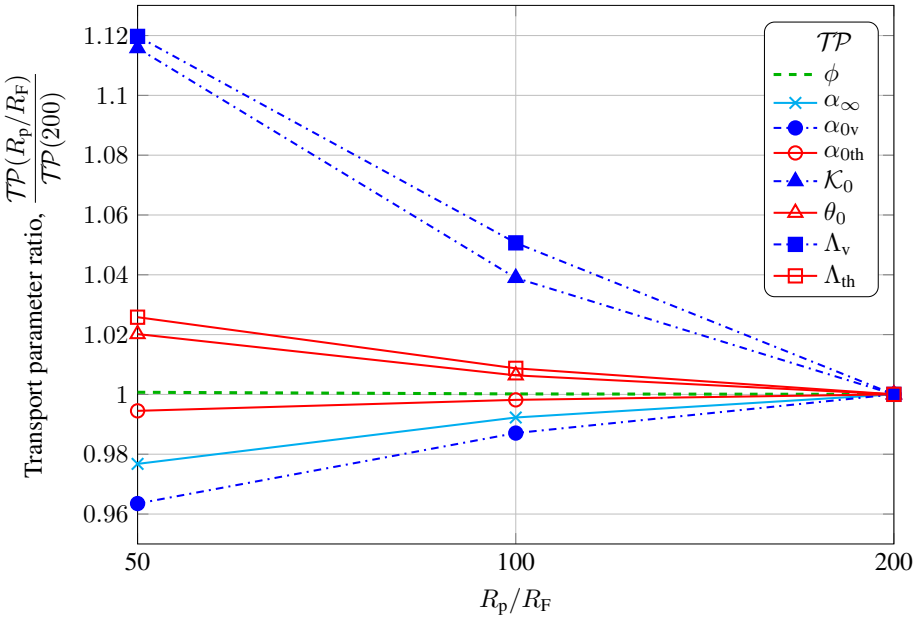

Figure 18: Relative changes of transport parameters ($\mathcal{TP}$) with respect to the ratio of the pore radius $R_p = 0.11$ mm to the decreasing fillet radius R_F

Figure 18 shows how the transport parameters, computed for different (decreasing) radii of fillets, converge to the values found for the smallest considered fillet radius $R_F = R_p/200$. The values of transport parameters for the case with the smallest fillet (i.e. the values from the last row in Table 7) were used to calculate the dynamic permeability and tortuosity functions using the JCA, JCAL, and JCALP models recalled at the end of Section A.2. These dynamic functions are compared in Figures 19, 20, and 21 with their counterparts found from the *Direct Multiscale* (DM) computations using MESH R/∞ ($^1/_{16}$) (for the analysis of harmonic viscous flow) and MESH R/∞ ($^1/_{48}$) (for the harmonic thermal diffusion). As expected, the results for the JCALP model are the most accurate in the sense of being nearly the same as the DM results: small discrepancies between the DM and JCALP curves of dynamic permeabilities are barely visible in Figure 19; they are easier to see when comparing the real parts of dynamic tortuosities in Figures 20 and 21. The discrepancies between the DM results and the JCAL or JCA results are more pronounced. The JCA curves of dynamic thermal permeability (see the lower chart in Figure 19) differ but not so much from the DM / JCALP / JCAL results, and it seems that the correction introduced by θ_0 is not so crucial as in the case of the fibrous material investigated in Section 3.1 (cf. Figure 6). The corrections introduced by α_{0th} and α_{0v} appear to be more important than those introduced by θ_0, especially, when looking at the curves of the wave speed and attenuation presented in Figure 22, and sound absorption presented in Figure 23, where more noticeable differences appear only when the JCAL / JCA results are compared versus the DM / JCALP ones. Figure 23 shows also the acoustic absorption curves computed using the *Direct Numerical Simulations* (DNS). For the considered porous layer thickness values (i.e. for $h = 10$ mm and $h = 20$ mm) the DNS results tend to be closer to the DM / JCALP results than to the JCAL / JCA results. Note that the DNS curves were computed from the surface acoustic impedances determined on the surface A, or alternatively, on the surface B (see MESH for DNS in Figure 14), since the propagation in the adjacent air layer is practically lossless, i.e. the surface acoustic impedance $Z_s(\omega)$ on the surface A is different than the one on the surface B, but the results of acoustic absorption are the same. Finally, recall also that the DM and DNS results were computed using the geometry without fillets and (consistently) rather coarse meshes, which might have had some influence on their accuracy. On the other hand, the direct results are not affected by the singularity around sharp edges and the consistency between the DNS, DM and JCALP results is indeed confirmed.

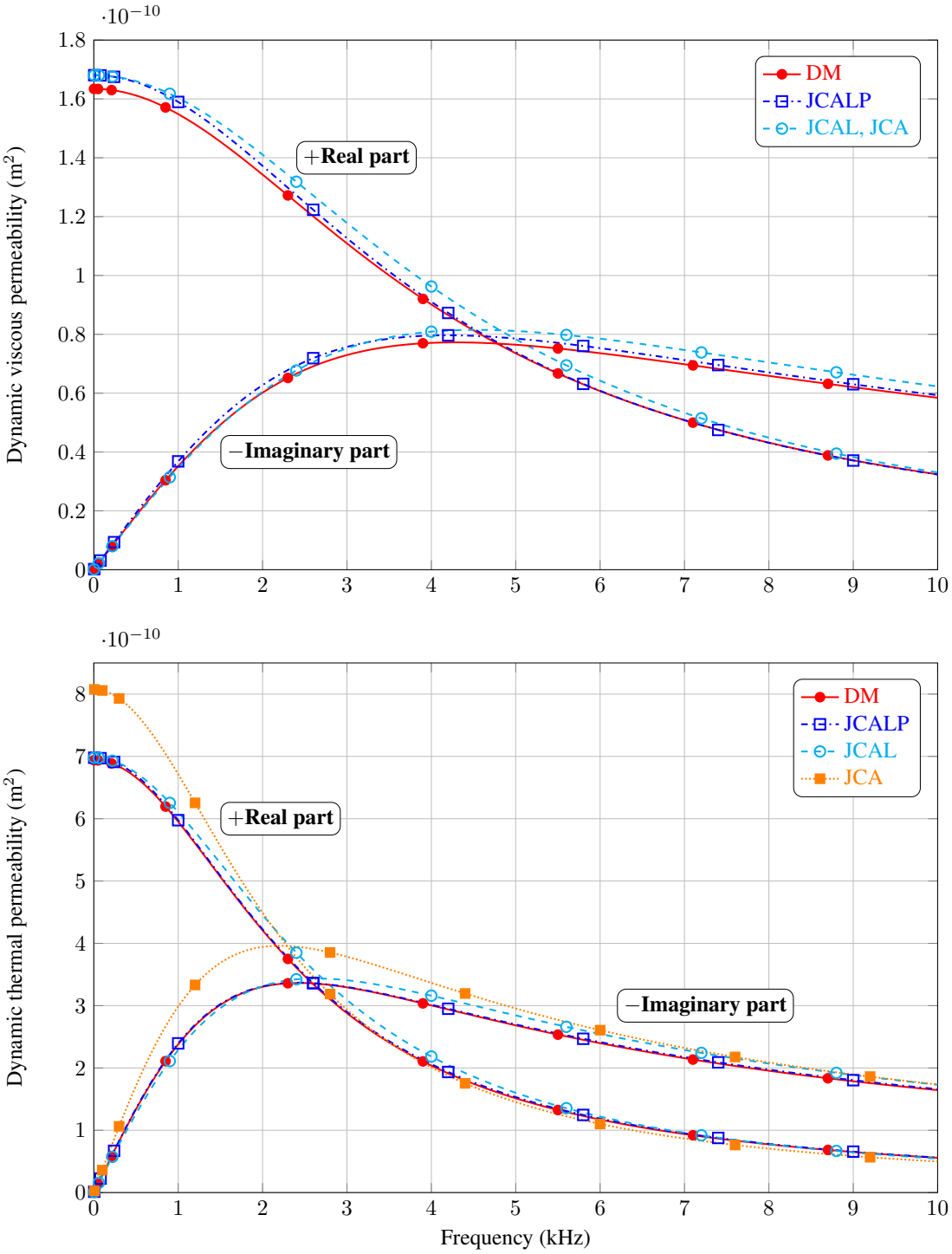

Figure 19: Dynamic viscous and thermal permeabilities for the regular periodic foam: DM – *Direct Multiscale* computations; JCALP, JCAL, JCA – *Hybrid Multiscale* calculations with the specified model

4 Conclusions

Two benchmark examples have been considered based on idealised (easily reproducible) microstructures intended to represent fibrous materials and cellular foams, respectively, i.e. two main kinds of sound-absorbing materials. Various results obtained for both benchmarks using three different methods of calculation (DM, HM, and DNS) have been compared, enabling mutual verification of these results. Moreover, the simple geometries have enabled precise convergence tests, so that the values of transport parameters in Tables 5 and 7 (with the only exception of the results presented for the mesh case $\mathrm{R}/50^{\#}$) are accurate up to the last shown significant digit. Periodic boundary conditions have been applied, however, when possible and in particular in the second benchmark example, we have demonstrated how to take advantage of

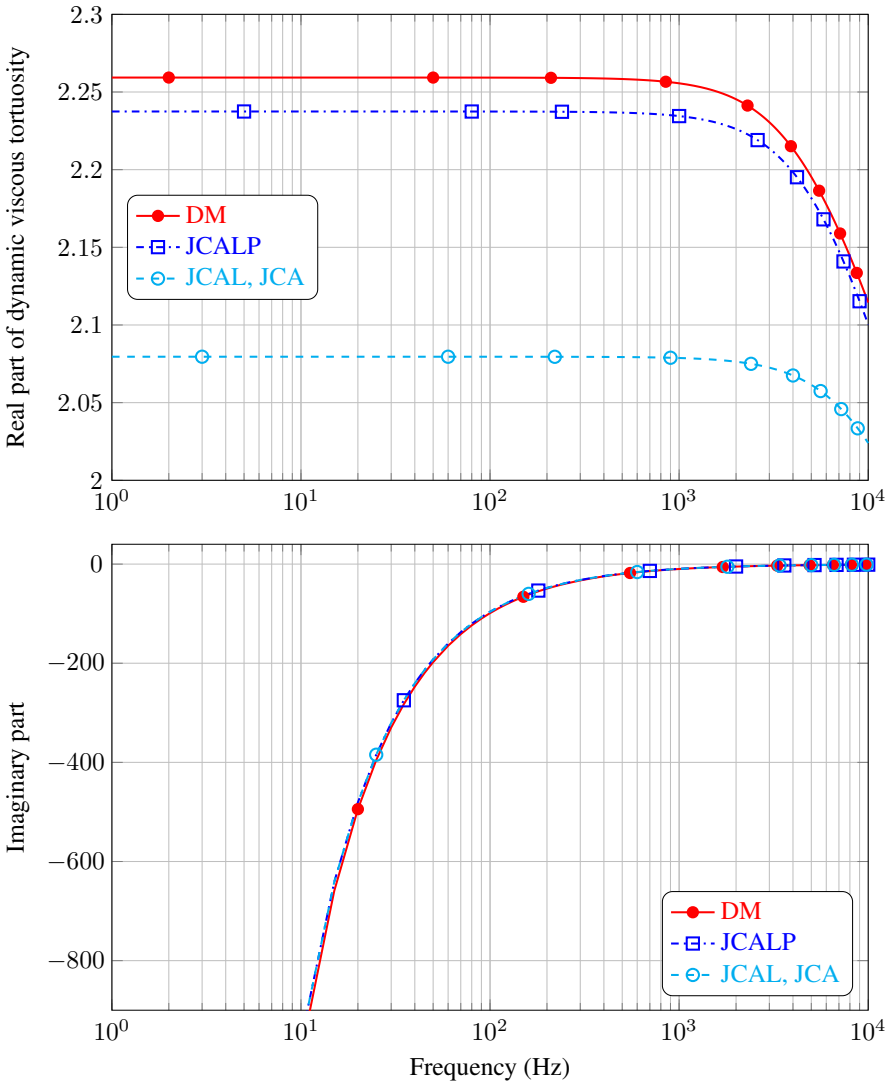

Figure 20: Dynamic viscous tortuosity for the regular periodic foam: DM – *Direct Multiscale* computations; JCALP, JCAL, JCA – *Hybrid Multiscale* calculations with the specified model

all existing symmetries (and anti-symmetries) of a REV. Below we present some additional remarks and practical hints that should help the readers to carry out their own numerical calculations for both benchmarks as well as other sound absorbing materials.

Finite element meshes for the HM calculations must be sufficiently fine in order to determine the transport parameters with proper accuracy. Of course, for practical use, it is not important to have the transport parameters determined to 5-digit accuracy, as we have done it in this work for obvious benchmarking reasons. Usually, the DM calculations do not require meshes of such density, because the viscous and thermal permeability functions are determined directly at each frequency by averaging the relevant viscous and thermal fields (of the scaled velocity and temperature), so they are less sensitive than the calculations based on the formulae depending on transport parameters. Nevertheless, the HM approach is less computationally demanding than the DM approach, since the latter requires solution of complex-valued problems (i.e. the oscillatory Stokes flow and thermal diffusion) for each computational frequency. In both cases, meshes on the corresponding periodic boundaries must be consistent, which means that, in practice, a mesh from one periodic boundary must be copied onto its periodic counterpart. Otherwise (i.e. when an approach involving Lagrange multipliers is used instead of realising periodic boundary conditions on non-consistent meshes), one has to expect large (often unacceptable) inaccuracies, especially when the meshes on periodic boundaries are not very dense. Correct sound absorption predictions from DNS, obtained by solving at each frequency large systems of the linearised complex-valued Navier-Stokes equations, usually require huge computational resources, although, they can be reduced by using coarser meshes, which may be acceptable in case of simple microstructural geometries of appropriate size (as the ones proposed in the benchmark examples).

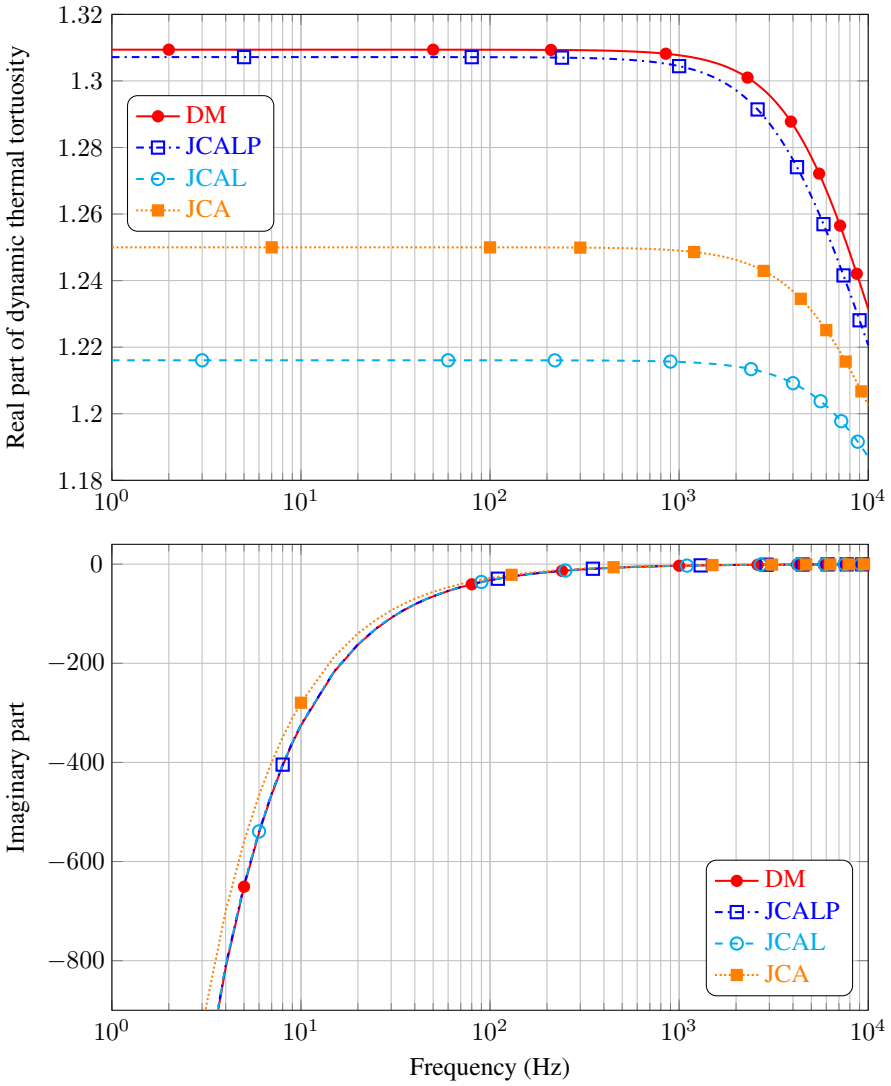

Figure 21: Dynamic thermal tortuosity for the regular periodic foam: DM – *Direct Multiscale* computations; JCALP, JCAL, JCA – *Hybrid Multiscale* calculations with the specified model

To calculate transport parameters with high accuracy, in particular, the porosity which in fact appears in the formulae for other transport parameters, any curved geometry of the solid boundary (e.g. the circular boundaries of fibres, or the partially spherical boundaries of pore walls and fillets in the benchmark examples) must be very accurately approximated by the finite element mesh which entails fine discretization on all curved boundaries. This requirement often makes the mesh on solid boundaries much denser than is actually required by proper implementation of boundary conditions in the Stokes flow or Laplace's problem, and thus, unnecessarily increases the number of degrees of freedom. One can easily avoid this by applying the quadratic shape order for geometry. This is a very efficient approach since it does not increase the number of degrees of freedom and at the same time it allows to represent the curved geometry much more accurately than in the case of the commonly-used linear shape order. The quadratic geometry shape order has enabled to obtain very accurate values of transport parameters using *not extremely* dense finite element meshes. For the mesh case $\mathrm{R}/50^{\#}$ we present the results computed using the linear geometry shape order (see the first row in Table 7) to demonstrate a small loss in accuracy related with that. On the other hand, we realise that many finite element systems or implementations take all information about the geometry (only) by importing finite element meshes generated by some dedicated software, or they simply do not support non-linear approximation of geometry. In such cases, one must increase the mesh density on the curved boundaries to reach the accuracy reported in this paper.

In the case of the viscous flow or Laplace problems with periodic boundaries, the solutions are not unique with respect to the pressure or potential, respectively, as there are no boundary conditions anywhere specifying their values. This may result in convergence problems during the numerical solution of the corresponding equations. The uniqueness of the flow solution is ensured by forcing the average of the pressure field to zero [55], i.e. $\langle \hat{\pi} \rangle_{\mathrm{f}} = 0$ or $\langle \hat{\pi}_0 \rangle_{\mathrm{f}} = 0$. Another way to

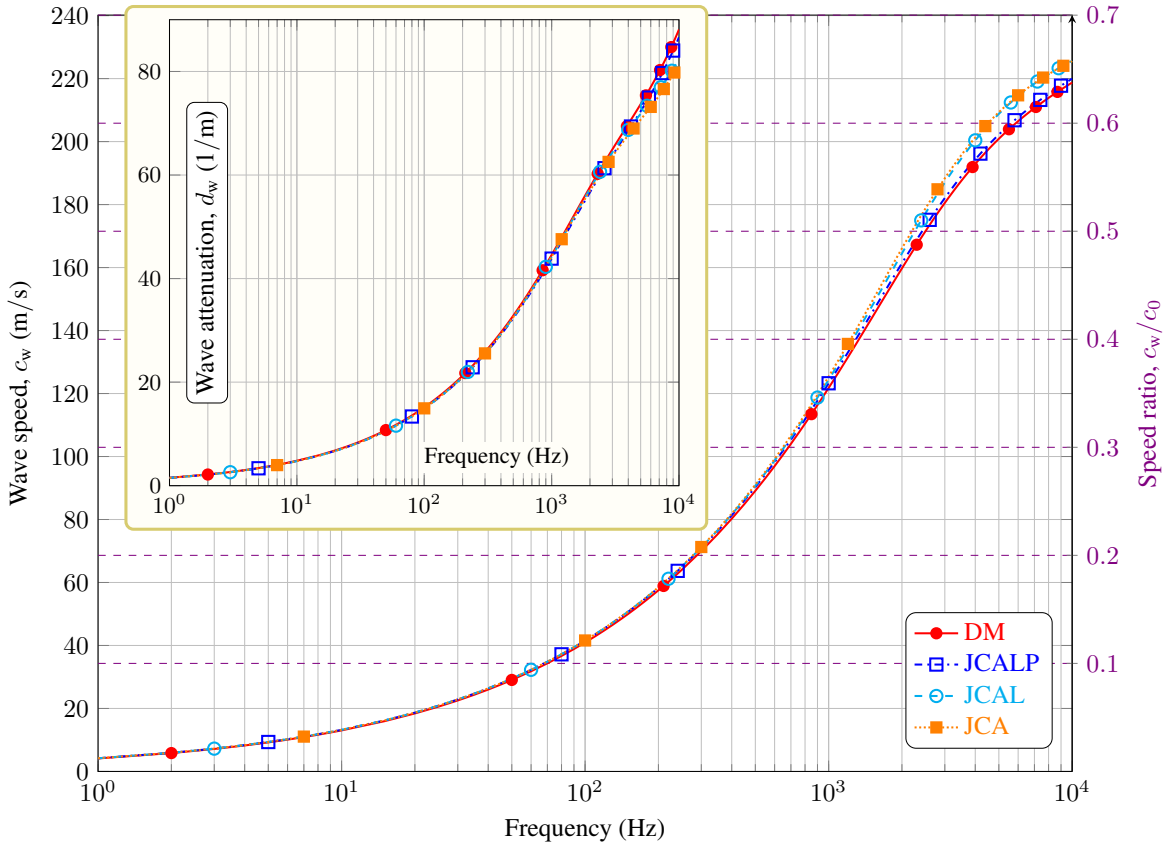

Figure 22: Wave speed and attenuation for the regular periodic foam: DM – *Direct Multiscale* computations; JCALP, JCAL, JCA – *Hybrid Multiscale* calculations with the specified model

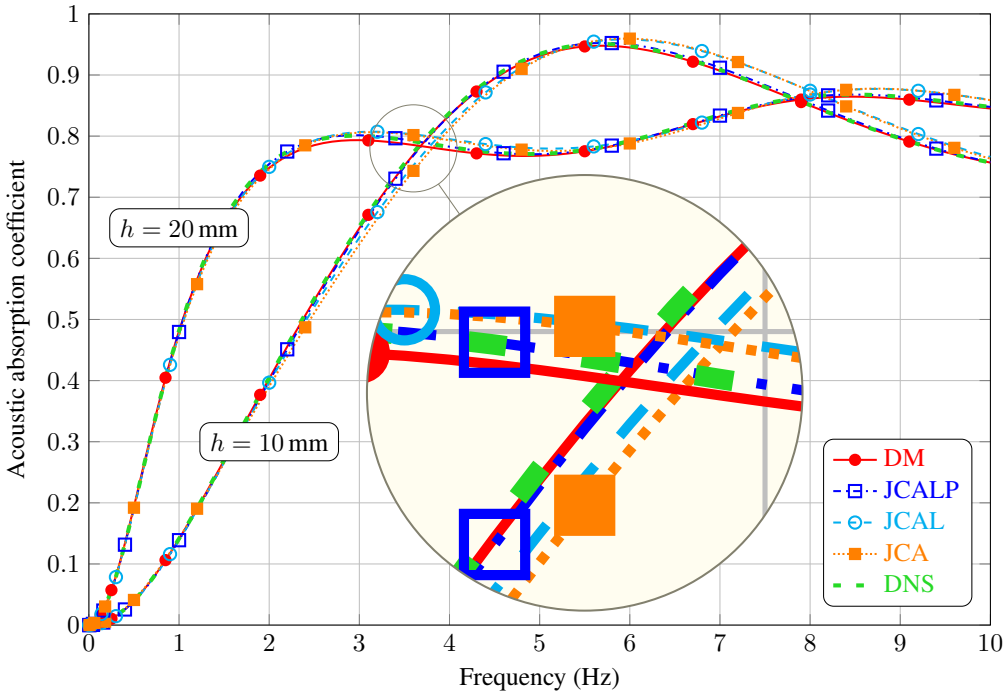

Figure 23: Sound absorption for the rigidly-backed regular periodic foam layers (of the specified thickness h): DM – *Direct Multiscale* computations; JCALP, JCAL, JCA – *Hybrid Multiscale* calculations with the specified model; DNS – *Direct Numerical Simulations*

ensure uniqueness is to set the level of pressure or potential by specifying them at some point (or in some other way). Of course, if the antisymmetric boundary conditions are used instead of the periodic ones, the values of pressure or potential are set to zero on the antisymmetry planes making the corresponding solutions unique.

When a porous microstructure possesses a sharp edge, the solution will not be smooth in its vicinity and the gradient of the solution can be singular at that point [77]. Therefore, one cannot expect the viscous characteristic length Λ_v to be mesh-independent and converge. We have shown how to deal with this problem by applying small fillets. In engineering practice, the size of fillets may be comparable or smaller than typical shape imperfections. In this work we have presented a few sets of transport parameters computed for the geometries with fillets of decreasing size. However, we have found out that reliable values of the transport parameters other than Λ_v can also be determined for the geometry without fillets.

Acknowledgements

This work is based upon collaboration between the authors supported by European Cooperation in Science and Technology (COST) through the COST Action CA15125 – DENORMS: "*Designs for Noise Reducing Materials and Structures*". T. G. Zieliński would like to acknowledge the financial support from Project "*Relations between the micro-geometry and sound propagation and absorption in porous and poroelastic media*", under Grant Agreement No. 2015/19/B/ST8/03979 by the National Science Centre (NCN), Poland. M. Červenka would like to acknowledge the financial support by grant No. GA18-24954S by the Czech Science Foundation. R. Venegas acknowledges partial support from Corporación de Fomento de la Producción CORFO Chile (Production Development Corporation) through grant 16ENI2-66903 InnovIng2030.

A Sound propagation in rigid-frame porous media

A.1 Homogenisation based on periodicity

Let us consider a periodic porous material comprising a pore fluid network and a solid frame. The former is fully connected and saturated with fluid (air) while the latter is assumed motionless because either the solid frame stiffness or its weight is significantly larger than that of the saturating fluid. The existence of a microscopic characteristic length ℓ, determined by the size of local heterogeneities or the period size of the material, and a macroscopic characteristic length $L = \lambda_\mathrm{w}/2\pi$, where λ_w is the sound wavelength, and their highly distinct values, i.e. $\ell/L \ll 1$, permit defining a Representative Elementary Volume. The porosity of the material is the ratio between the volume occupied by the fluid and the total volume of the material, which in terms of the volume of the REV occupied by the fluid Ω_f and the total volume of the REV Ω can be calculated as $\phi = \Omega_\mathrm{f}/\Omega$.

The linearised equations that describe the flow of a compressible fluid saturating the pore fluid network Ω_f in harmonic regime are [7–9, 27, 78] the equations of momentum (A.1), mass (A.2), and energy (A.3) conservation, as well as the equation of state (A.4), namely,

$$\eta\left(\nabla^2\mathbf{v} + \frac{1}{3}\nabla(\nabla\cdot\mathbf{v})\right) - \nabla p = \mathrm{i}\omega\varrho_0\mathbf{v} \quad \text{in } \Omega_\mathrm{f}, \tag{A.1}$$

$$\varrho_0\nabla\cdot\mathbf{v} + \mathrm{i}\omega\varrho = 0 \quad \text{in } \Omega_\mathrm{f}, \tag{A.2}$$

$$\kappa\nabla^2 T = \mathrm{i}\omega\varrho_0 C_\mathrm{p} T - \mathrm{i}\omega p \quad \text{in } \Omega_\mathrm{f}, \tag{A.3}$$

$$\frac{p}{P_0} = \frac{\varrho}{\varrho_0} + \frac{T}{T_0} \quad \text{in } \Omega_\mathrm{f}, \tag{A.4}$$

together with the no-slip (A.5) and zero-temperature (A.6) conditions formulated on the interface Γ_sf between the pore fluid network and the solid frame:

$$\mathbf{v} = \mathbf{0} \quad \text{on } \Gamma_\mathrm{sf}, \tag{A.5}$$

$$T = 0 \quad \text{on } \Gamma_\mathrm{sf}. \tag{A.6}$$

Here, $\omega = 2\pi f$ is the angular frequency (f is the frequency; note also that a positive convention has been adopted, i.e. $\exp(+\mathrm{i}\omega t)$, where i is the imaginary unit and t is the temporal variable), while $\mathbf{v}$, p, ϱ, and T are the (unknown complex amplitudes of) oscillatory fluid velocity, pressure, density, and temperature, respectively. The physical parameters are the dynamic viscosity η, thermal conductivity κ, and heat capacity at constant pressure C_p of the saturating fluid, and those with a zero subscript are equilibrium quantities, i.e. ϱ_0 is the fluid density at the equilibrium state of ambient pressure P_0 and temperature T_0. The standard values of these properties (which were used in calculations) are given for air in Table 4, in Section 2.

We aim at deriving a macroscopic description of sound propagation in periodic porous media by using the two-scale asymptotic homogenisation method [78]. To do so, a physical analysis of the local description, Eqs. (A.1)–(A.6), is first conducted. This analysis for the variables and terms of the local description is well established [8, 27, 78], will be used to rescale the local description, and is as follows.

Consistent with the assumed separation of scales $\ell \ll L$, the pressure varies macroscopically, i.e. $\nabla p = O(p/L)$, while viscous effects occur locally, i.e. $\eta\nabla^2\mathbf{v} = O(\eta v/\ell^2)$, where $v = \|\mathbf{v}\|$ is an estimation of the fluid velocity ($\|\cdot\|$ is the Euclidean norm). Furthermore, in order to account for the macroscopic compressibility, the divergence of the velocity is considered to vary with the sound wavelength $\lambda_\mathrm{w} = 2\pi L$, i.e. $\nabla\cdot\mathbf{v} = O(v/L)$. The quoted estimates will lead to a fluid velocity field that is asymptotically divergence-free at the pore scale, bringing as a consequence the uncoupling of the viscous and thermal effects in the pores. On the other hand, heat conduction effects occur locally and, consequently, one has the following estimate $\kappa\nabla^2 T = O(\kappa T/\ell^2)$.

Regarding the relative order of magnitude of the terms in the equation of conservation of momentum (A.1), the case of interest occurs when the viscous and inertial terms are balanced by the pressure gradient, which is expressed as $O(\eta v/\ell^2) = O(\omega\varrho_0 v) = O(p/L)$. Furthermore, the estimations of the terms in the equation of conservation of mass (A.2) are of the same order of magnitude, i.e. $O(v/L) = O(\omega\varrho/\varrho_0)$. On the other hand, the conduction and inertial terms in Eq. (A.3) are balanced by the heat source due to pressure. Hence one has that $O(\kappa T/\ell^2) = O(\varrho_0 C_\mathrm{p}\omega T) = O(\omega p)$.

Now let us introduce two independent space variables, namely, $\mathbf{x}$ which is the usual spatial variable, and $\mathbf{y} = \varepsilon^{-1}\mathbf{x}$, where $\varepsilon = \ell/L \ll 1$; therefore, $\mathbf{x}$ accounts for variations at the macroscopic scale while $\mathbf{y}$ for those occurring locally. As a consequence of the introduction of these two spatial variables, the large separation of scales (i.e. $\varepsilon \ll 1$), and periodicity, the unknown physical variables are, a priori, functions of $\mathbf{x}$ and $\mathbf{y}$, namely, $\mathbf{v} = \mathbf{v}(\mathbf{x},\mathbf{y})$ and so on. Furthermore, considering once again the large separation of scales, invoking the chain rule and taking L as the reference length, the gradient operator can be expressed as $\nabla = \nabla_{(x,y)} = \nabla_x + \varepsilon^{-1}\nabla_y$. Note that to simplify the notation we have unbolded the spatial variables.

The use of two space variables is combined with a rescaling of the local equations based upon a single space variable. The reason for the rescaling lies in the fact that when expressed with the two space variables (x, y), the actual physical gradient of a quantity Q that varies at the macroscopic scale, i.e. $\nabla_x Q$ becomes ∇Q. On the other hand, if the quantity varies at the local scale, the actual physical gradient $\nabla_y Q$ is expressed as $\varepsilon\nabla Q$. Therefore, the gradient of variables oscillating locally is rescaled.

Recalling that the gradient operator reads now as $\nabla = \nabla_x + \varepsilon^{-1}\nabla_y$, the rescaled equations of motion in the fluid-saturated pore domain Ω_f are given by

$$\varepsilon^2\eta\left(\nabla^2\mathbf{v} + \frac{1}{3}\nabla(\nabla\cdot\mathbf{v})\right) - \nabla p = \mathrm{i}\omega\varrho_0\mathbf{v} \quad \text{in } \Omega_\mathrm{f}, \tag{A.7}$$

$$\nabla\cdot\mathbf{v} + \mathrm{i}\omega\left(\frac{p}{P_0} - \frac{T}{T_0}\right) = 0 \quad \text{in } \Omega_\mathrm{f}, \tag{A.8}$$

$$\varepsilon^2\kappa\nabla^2 T = \mathrm{i}\omega\varrho_0 C_\mathrm{p} T - \mathrm{i}\omega p \quad \text{in } \Omega_\mathrm{f}, \tag{A.9}$$

with the no-slip and isothermal boundary conditions on the walls of solid frame (skeleton, fibres, etc.)

$$\mathbf{v} = \mathbf{0} \quad \text{on } \Gamma_\mathrm{sf}, \tag{A.10}$$

$$T = 0 \quad \text{on } \Gamma_\mathrm{sf}. \tag{A.11}$$

The unknown variables are then looked for in the form of asymptotic expansions in powers of the small parameter ε, i.e. $Q(x,y) = \sum_{i=0}^{\infty}\varepsilon^i Q^{(i)}$, where $Q = \mathbf{v}, p, \varrho, T$. Then, these series are replaced into Eqs. (A.7)–(A.11) and the terms of the same order are identified. Note that $Q^{(i)}$ and Q are frequency-dependent, which is implicitly assumed in all formulae.

At ε^{-1}, it follows from the equation of conservation of momentum that $\nabla_y p^{(0)} = \mathbf{0}$, which means that the leading-order pressure is a macroscopic variable, i.e. $p^{(0)} = p^{(0)}(x)$.

Further identification provides the following oscillatory Stokes flow problem

$$\eta\nabla_y^2\mathbf{v}^{(0)} - \nabla_y p^{(1)} = \mathrm{i}\omega\varrho_0\mathbf{v}^{(0)} + \nabla_x p^{(0)} \quad \text{in } \Omega_\mathrm{f}, \tag{A.12}$$

$$\nabla_y\cdot\mathbf{v}^{(0)} = 0 \quad \text{in } \Omega_\mathrm{f}, \tag{A.13}$$

$$\mathbf{v}^{(0)} = \mathbf{0} \quad \text{on } \Gamma_\mathrm{sf}. \tag{A.14}$$

This is a linear problem forced by the macroscopic pressure gradient $\nabla_x p^{(0)}$. Therefore, the velocity $\mathbf{v}^{(0)}$ and local pressure $p^{(1)}$ can be linearly related to $\nabla_x p^{(0)}$ via [7, 8]

$$\mathbf{v}^{(0)}(x,y) = -\frac{\tilde{\underline{\underline{\mathbf{k}}}}(y,\omega)}{\eta}\cdot\nabla_x p^{(0)}(x), \tag{A.15}$$

$$p^{(1)}(x,y) = -\tilde{\pi}(y,\omega)\cdot\nabla_x p^{(0)}(x) + \bar{p}^{(1)}(x), \tag{A.16}$$

where $\tilde{\underline{\underline{\mathbf{k}}}}(y,\omega)$ represents an Ω-periodic local tensor field, $\tilde{\pi}(y,\omega)$ is an Ω-periodic local vector field, and $\bar{p}^{(1)}(x)$ is a constant field. The Ω-periodicity means that such a field must satisfy the conditions of periodic continuity on the corresponding fluid boundaries lying on opposite faces of the periodic cell Ω.

Let us now define the following averaging operator

$$\langle\cdot\rangle = \frac{1}{\Omega}\int_{\Omega_\mathrm{f}}(\cdot)\,\mathrm{d}\Omega = \frac{\phi}{\Omega_\mathrm{f}}\int_{\Omega_\mathrm{f}}(\cdot)\,\mathrm{d}\Omega = \phi\,\langle\cdot\rangle_\mathrm{f}\,, \tag{A.17}$$

which is related to the whole periodic cell Ω (containing a fluid domain Ω_f and a motionless rigid skeleton), while the operator $\langle\cdot\rangle_\mathrm{f} = \frac{1}{\Omega_\mathrm{f}}\int_{\Omega_\mathrm{f}}(\cdot)\,\mathrm{d}\Omega$ averages over the fluid domain Ω_f. Incidentally, note that the pressure field (A.16) has been expressed in terms of the integration constant $\bar{p}^{(1)}(x)$ and a zero-mean part, i.e. the first term on the right-hand side of Eq. (A.16) vanishes when the averaging operator (A.17) is applied.

The application of the operator (A.17) to Eq. (A.15) yields the dynamic Darcy's law [8]

$$\mathbf{V}(x) = -\frac{\underline{\underline{\mathbf{k}}}(\omega)}{\eta}\cdot\nabla p(x), \tag{A.18}$$

where the superscript indicating the order and the subscript x have been dropped in this macroscopic description and

$$\mathbf{V}(x) = \left\langle \mathbf{v}^{(0)}(x,y)\right\rangle = \phi\left\langle \mathbf{v}^{(0)}(x,y)\right\rangle_\mathrm{f} \tag{A.19}$$

defines the Darcy velocity (i.e. the macroscopic flux), while the dynamic viscous permeability (second-rank) tensor $\underline{\underline{\mathbf{k}}}$ is calculated as [8]

$$\underline{\underline{\mathbf{k}}}(\omega) = \left\langle \tilde{\underline{\underline{\mathbf{k}}}}(y,\omega)\right\rangle = \phi\left\langle \tilde{\underline{\underline{\mathbf{k}}}}(y,\omega)\right\rangle_\mathrm{f}. \tag{A.20}$$

Now, let us consider the equation of conservation of energy (A.9) and the isothermal boundary condition (A.11), from which the following leading-order heat conduction cell problem is identified

$$\kappa\nabla_y^2 T^{(0)} = \mathrm{i}\omega\varrho_0 C_\mathrm{p} T^{(0)} - \mathrm{i}\omega p^{(0)} \quad \text{in } \Omega_\mathrm{f}, \tag{A.21}$$

$$T^{(0)} = 0 \quad \text{on } \Gamma_\mathrm{sf}. \tag{A.22}$$

This linear problem is driven by the harmonic rate of macroscopic pressure $\mathrm{i}\omega p^{(0)}$. Therefore, the unknown leading-order temperature $T^{(0)}$ can be linearly related to $\mathrm{i}\omega p^{(0)}$ via [7, 27]

$$T^{(0)}(x,y) = \frac{\tilde{\theta}(y,\omega)}{\kappa}\mathrm{i}\omega p^{(0)}(x), \tag{A.23}$$

where $\tilde{\theta}(y,\omega)$ represents an Ω-periodic local scalar field. The averaging operation (A.17) can be applied to this relation and the so-called dynamic thermal permeability [27] is defined in a way similar to its viscous analogue (A.20), namely,

$$\theta(\omega) = \left\langle \tilde{\theta}(y,\omega)\right\rangle = \phi\left\langle \tilde{\theta}(y,\omega)\right\rangle_\mathrm{f}. \tag{A.24}$$

Finally, let us consider the resulting leading-order of the mass balance equation (A.8) (which has already been combined with the equation of state)

$$\nabla_x\cdot\mathbf{v}^{(0)} + \nabla_y\cdot\mathbf{v}^{(1)} + \mathrm{i}\omega\left(\frac{p^{(0)}}{P_0} - \frac{T^{(0)}}{T_0}\right) = 0. \tag{A.25}$$

The following results are obtained when averaging this equation using the operator (A.17). The averaging of the first term in Eq. (A.25) becomes the divergence of the macroscopic (Darcy) velocity (A.19), namely, $\left\langle\nabla_x\cdot\mathbf{v}^{(0)}\right\rangle = \nabla_x\cdot\left\langle\mathbf{v}^{(0)}\right\rangle = \nabla\cdot\mathbf{V}$, while the second term simply vanishes, i.e. $\left\langle\nabla_y\cdot\mathbf{v}^{(1)}\right\rangle = 0$, since by applying the divergence theorem when this term is averaged, it can be re-written as a surface integral which becomes zero because of both the overall no-slip condition (A.5) on the solid walls and the fact that on the remaining boundaries of the fluid domain (lying on the periodic cell faces) it cancels out due to periodicity. The averaging of the third term in Eq. (A.25) and inserting the relation (A.23) lead to the following result

$$\mathrm{i}\omega\left\langle\frac{p^{(0)}(x)}{P_0} - \frac{T^{(0)}(x,y)}{T_0}\right\rangle = \mathrm{i}\omega\frac{\phi\,p^{(0)}(x)}{P_0}\left(1 - \frac{(\gamma-1)}{\gamma}\frac{\varrho_0 C_\mathrm{p}}{\kappa}\,\mathrm{i}\omega\left\langle\tilde{\theta}(y,\omega)\right\rangle_\mathrm{f}\right), \tag{A.26}$$

where the thermodynamic identity $P_0/T_0 = \varrho_0 C_\mathrm{p}(\gamma-1)/\gamma$ has been used, with γ being the specific heat ratio of the pore fluid. Finally, by combining all these results together and using the definition (A.24), the averaging of Eq. (A.25) leads to

the following formula for the macroscopic mass balance equation (after dropping the superscript indicating the order and the subscript x)

$$\nabla \cdot \mathbf{V}(x) + \mathrm{i}\omega\, \mathcal{C}(\omega)\, p(x) = 0, \tag{A.27}$$

where the effective compressibility $\mathcal{C}(\omega)$ of the homogenised medium is defined as

$$\mathcal{C}(\omega) = \frac{\phi}{P_0}\left(1 - \frac{(\gamma-1)}{\gamma}\frac{\varrho_0 C_\mathrm{p}}{\phi\kappa}\,\mathrm{i}\omega\,\theta(\omega)\right). \tag{A.28}$$

Equations (A.18) and (A.27) describe the harmonic flow in a homogenised porous medium characterised by the effective compressibility $\mathcal{C}$ and dynamic viscous permeability tensor $\underline{\underline{\mathbf{k}}}$ (alternatively, one may use the dynamic flow resistivity tensor $\underline{\underline{\boldsymbol{\sigma}}} = \eta\,\underline{\underline{\mathbf{k}}}^{-1}$). To discuss the isotropic sound propagation in such a medium, let us now consider that the porous material is macroscopically isotropic, i.e. $\underline{\underline{\mathbf{k}}}(\omega) = \mathcal{K}(\omega)\,\underline{\underline{\mathbf{I}}}$, where $\underline{\underline{\mathbf{I}}}$ is the unitary second-rank tensor (and consequently, $\underline{\underline{\boldsymbol{\sigma}}} = \sigma(\omega)\,\underline{\underline{\mathbf{I}}}$, where $\sigma(\omega) = \eta/\mathcal{K}(\omega)$); with some approximation, this approach is also valid in the case of a preferential flow (or wave propagation) direction. Now, the dynamic Darcy's law (A.18) takes the isotropic form

$$\mathbf{V}(x) = -\frac{\mathcal{K}(\omega)}{\eta}\nabla p(x) \tag{A.29}$$

which, when combined with the macroscopic mass balance equation (A.27), leads to the Helmholtz equation for harmonic wave propagation in isotropic media

$$\nabla^2 p(x) + \omega^2 \frac{\eta\,\mathcal{C}(\omega)}{\mathrm{i}\omega\,\mathcal{K}(\omega)} p(x) = 0\,, \tag{A.30}$$

where the effective wave number k_w and the effective (complex-valued) speed of sound c_e can be at once identified as

$$k_\mathrm{w}(\omega) = \omega\sqrt{\frac{\eta\,\mathcal{C}(\omega)}{\mathrm{i}\omega\,\mathcal{K}(\omega)}}, \qquad c_\mathrm{e}(\omega) = \sqrt{\frac{\mathrm{i}\omega\,\mathcal{K}(\omega)}{\eta\,\mathcal{C}(\omega)}}. \tag{A.31}$$

The effective bulk modulus B_e and density ϱ_e, as well as the characteristic impedance Z_e for the homogenised medium are calculated from the following formulae

$$B_\mathrm{e}(\omega) = \frac{1}{\mathcal{C}(\omega)}\,, \qquad \varrho_\mathrm{e}(\omega) = \frac{\eta}{\mathrm{i}\omega\,\mathcal{K}(\omega)} = \frac{\sigma(\omega)}{\mathrm{i}\omega}\,, \qquad Z_\mathrm{e}(\omega) = \sqrt{\frac{\eta}{\mathrm{i}\omega\,\mathcal{K}(\omega)\,\mathcal{C}(\omega)}} = \sqrt{\frac{\sigma(\omega)}{\mathrm{i}\omega\,\mathcal{C}(\omega)}}\,, \tag{A.32}$$

where the first formula is (by definition) straightforward, while the latter two are derived by recalling the well-known relations $c_\mathrm{e} = \sqrt{B_\mathrm{e}/\varrho_\mathrm{e}}$ and $Z_\mathrm{e} = \varrho_\mathrm{e}\,c_\mathrm{e}$. Note that the following (harmonic and source-less) Cauchy momentum equation is satisfied: $\mathrm{i}\omega\varrho_\mathrm{e}\mathbf{V} + \nabla p = 0$; the formula for ϱ_e is also obtained when this equation is combined with the isotropic form of Darcy's law (A.29).

A.2 Dynamic permeability and tortuosity functions, effective properties and sound absorption

As demonstrated above, the macroscopic description of sound propagation in single-porosity rigid-frame materials is related to two response functions: the dynamic viscous permeability $\mathcal{K}(\omega)$ and the dynamic thermal permeability $\theta(\omega)$. When these functions are known, the complex-valued frequency-dependent effective properties (i.e. $\varrho_\mathrm{e}(\omega)$, $\mathcal{C}(\omega)$ or $B_\mathrm{e}(\omega)$, etc.) can be calculated and sound propagation can be analysed in a homogenised medium of acoustic fluid using the Helmholtz equation (A.30).

In this work, wave propagation in isotropic media is considered, which means that the dynamic permeability tensor $\underline{\underline{\mathbf{k}}}(\omega)$ is isotropic or can be approximated as such. Then, the dynamic permeability function can be computed as the spherical part of this tensor, namely, $\mathcal{K}(\omega) = \frac{1}{N}\,\mathrm{tr}\,\underline{\underline{\mathbf{k}}}(\omega) = \frac{1}{N}\underline{\underline{\mathbf{k}}}(\omega) \bullet \underline{\underline{\mathbf{I}}}$ (here, $N = 2$ or $N = 3$ for two- or three-dimensional problems, respectively, the operator tr is the trace of a tensor, and the operation $\bullet$ is the scalar product of two second-order tensors), which is justified when its deviatoric part $(\underline{\underline{\mathbf{k}}} - \mathcal{K}\,\underline{\underline{\mathbf{I}}})$ is zero (i.e. tends to $\underline{\underline{\mathbf{0}}}$ when compared with $\underline{\underline{\mathbf{k}}}$) or at least the norm of it is much smaller than $|\mathcal{K}|$. Finally, the isotropic approximation is also possible in the case of a plane-wave propagation in the preferential direction defined by a unitary vector $\mathbf{e}$; then, the dynamic permeability function is computed as $\mathcal{K}(\omega) = \left(\underline{\underline{\mathbf{k}}}(\omega)\cdot\mathbf{e}\right)\cdot\mathbf{e}$. Note that in that case (which is, of course, also true for truly isotropic tensor $\underline{\underline{\mathbf{k}}}$), one needs to know only the projection of $\underline{\underline{\mathbf{k}}}$ onto this direction, i.e. the vector $\mathbf{k}^{\{\mathbf{e}\}} \equiv \underline{\underline{\mathbf{k}}}\cdot\mathbf{e}$. To determine this vector (for any chosen direction $\mathbf{e}$) one must solve the leading-order boundary value problem of oscillatory viscous flow (A.12)–(A.14) (arising from homogenisation) for a discrete set of (computational) frequencies, assuming that the locally-constant pressure gradient driving the flow is $\nabla_x p^{(0)} = \left\|\nabla_x p^{(0)}\right\|\mathbf{e}$ (where the value of $\left\|\nabla_x p^{(0)}\right\|$ can be taken arbitrarily but should be small enough to comply with the assumption of linearity). Then, the numerically calculated

leading-order fluid velocity field $\mathbf{v}^{(0)}$ is inserted in formula (A.15), which is averaged using the operator (A.17) to get the projection of the dynamic permeability tensor onto $\mathbf{e}$ as

$$\mathbf{k}^{\{\mathbf{e}\}} \equiv \underline{\underline{\mathbf{k}}} \cdot \mathbf{e} = \left\langle \underline{\underline{\tilde{\mathbf{k}}}} \cdot \mathbf{e} \right\rangle = -\frac{\eta}{\left\| \nabla_x p^{(0)} \right\|} \phi \left\langle \mathbf{v}^{(0)} \right\rangle_{\mathrm{f}} . \tag{A.33}$$

Alternatively, one can conveniently reformulate the oscillatory Stokes problem and use the fact that the dynamic viscous permeability tensor is symmetric [78] as follows. Let us formally define: the unitary vector $\mathbf{e} \equiv \nabla_x p^{(0)} / \left\| \nabla_x p^{(0)} \right\|$ specifying the constant pressure gradient direction (and thus, the preferential wave propagation direction), the vector component $\hat{\mathbf{k}}$ (related to that direction) of the tensor field $\underline{\underline{\tilde{\mathbf{k}}}}$, that is, $\hat{\mathbf{k}} \equiv \underline{\underline{\tilde{\mathbf{k}}}} \cdot \mathbf{e}$, and the scalar field $\hat{\pi} \equiv \tilde{\pi} \cdot \mathbf{e}$ as the projection of the vector field $\tilde{\pi}$ onto $\mathbf{e}$. Using these relations for formulae (A.15) and (A.16), when inserting them into Eqs. (A.12)–(A.14), leads to an oscillatory viscous flow problem formulated in terms of the Ω-periodic (unknown) vector field $\hat{\mathbf{k}}$ and scalar field $\hat{\pi}$, namely,

$$\frac{\mathrm{i}\omega}{\nu} \hat{\mathbf{k}} - \nabla_y^2 \hat{\mathbf{k}} + \nabla_y \hat{\pi} = \mathbf{e} \quad \text{in } \Omega_{\mathrm{f}}, \tag{A.34}$$

$$\nabla_y \cdot \hat{\mathbf{k}} = 0 \quad \text{in } \Omega_{\mathrm{f}}, \tag{A.35}$$

$$\hat{\mathbf{k}} = \mathbf{0} \quad \text{on } \Gamma_{\mathrm{sf}}, \tag{A.36}$$

where $\nu = \eta / \varrho_0$ is the kinematic viscosity of the pore fluid. Note that $\hat{\mathbf{k}}(y, \omega)$ can be treated as an Ω-periodic velocity field normalised by $-\left\| \nabla_x p^{(0)} \right\| / \eta$, so this scaled-velocity field $\hat{\mathbf{k}}$ has the unit of permeability (m^2) [79], while $\hat{\pi}$ is a similarly normalised pressure field with the unit of length (m). Having calculated the solution $\hat{\mathbf{k}}$, the corresponding vector component of the (macroscopic) dynamic permeability tensor is found by averaging, i.e. $\mathbf{k}^{\{\mathbf{e}\}}(\omega) = \left\langle \hat{\mathbf{k}}(y, \omega) \right\rangle = \phi \left\langle \hat{\mathbf{k}}(y, \omega) \right\rangle_{\mathrm{f}}$. In the case of isotropy or if $\mathbf{e}$ is the preferential direction of flow the dynamic viscous permeability can be calculated as $\mathcal{K}(\omega) = \mathbf{k}^{\{\mathbf{e}\}}(\omega) \cdot \mathbf{e}$.

In general, if the whole (anisotropic) permeability tensor is needed, one should carry out N oscillatory flow calculations ($N = 2$ for 2D, and $N = 3$ for 3D problems), separately, for N mutually perpendicular directions $\mathbf{e}^{\{i\}}$ ($i = 1, \ldots, N$) related to the locally-constant pressure gradients driving the flow $\nabla_x p^{(0)} = \left\| \nabla_x p^{(0)} \right\| \mathbf{e}^{\{i\}}$. Denoting the projection of tensor $\underline{\underline{\mathbf{k}}}$ onto $\mathbf{e}^{\{i\}}$ by $\mathbf{k}^{\{i\}}$, i.e. $\mathbf{k}^{\{i\}} \equiv \underline{\underline{\mathbf{k}}} \cdot \mathbf{e}^{\{i\}}$, when all projections are found the dynamic permeability tensor is computed as $\underline{\underline{\mathbf{k}}} = \sum_{i=1}^{N} \mathbf{k}^{\{i\}} \otimes \mathbf{e}^{\{i\}}$.

To determine the dynamic thermal permeability $\theta(\omega)$, the leading-order boundary value problem (A.21)–(A.22), arising from homogenisation and describing the harmonically-driven thermal diffusion (or heat conduction) in the pores, must be solved for each one of the computational frequencies, assuming an arbitrary value for the locally-constant pressure field $p^{(0)}$. When the solution $T^{(0)}$ is found, this local temperature field is used with formula (A.23) to obtain the local field $\tilde{\theta}$, which is then averaged as shown in Eq. (A.24), to get the dynamic thermal permeability as

$$\theta = \left\langle \tilde{\theta} \right\rangle = \frac{\kappa}{\mathrm{i}\omega \, p^{(0)}} \phi \left\langle T^{(0)} \right\rangle_{\mathrm{f}} . \tag{A.37}$$

Equivalently, inserting Eq. (A.23) into Eqs. (A.21)–(A.22) leads to a (thermal) diffusion problem formulated in terms of the Ω-periodic unknown scalar field $\tilde{\theta}$, namely,

$$\frac{\mathrm{i}\omega}{\nu_{\mathrm{th}}} \tilde{\theta} - \nabla_y^2 \tilde{\theta} = 1 \quad \text{in } \Omega_{\mathrm{f}}, \tag{A.38}$$

$$\tilde{\theta} = 0 \quad \text{on } \Gamma_{\mathrm{sf}}, \tag{A.39}$$

where $\nu_{\mathrm{th}} = \kappa / (\varrho_0 C_{\mathrm{p}}) = \nu / N_{\mathrm{Pr}}$ is the thermal diffusivity, with $N_{\mathrm{Pr}} = \eta \, C_{\mathrm{p}} / \kappa$ being the Prandtl number for the pore fluid. Note that $\tilde{\theta}(y, \omega)$ can be treated as an Ω-periodic field of temperature normalised by $\mathrm{i}\omega p^{(0)} / \kappa$, so that $\tilde{\theta}$ has the unit of permeability (m^2) [79]. When this local field $\tilde{\theta}$ is found as the solution of this re-scaled thermal diffusion problem (A.38)–(A.39), the dynamic thermal permeability is computed by averaging, i.e. $\theta(\omega) = \left\langle \tilde{\theta}(y, \omega) \right\rangle = \phi \left\langle \tilde{\theta}(y, \omega) \right\rangle_{\mathrm{f}}$.

The effective density of the homogenised medium can be calculated from the formula depending on its porosity ϕ, dynamic visco-inertial tortuosity $\alpha(\omega)$ which is a generalization of the concept of tortuosity, and on the density ϱ_0 of saturating fluid, namely,

$$\varrho_{\mathrm{e}}(\omega) = \frac{\varrho_0 \, \alpha(\omega)}{\phi} . \tag{A.40}$$

When this equation is compared with the second formula from (A.32), the following relation of inverse proportionality between the functions of dynamic visco-inertial tortuosity and dynamic viscous permeability is obtained

$$\alpha(\omega) = \frac{\phi \, \nu}{\mathrm{i}\omega \, \mathcal{K}(\omega)} . \tag{A.41}$$

In the case of anisotropic porous structures, the second-order tensors of dynamic viscous tortuosity, $\underline{\underline{\boldsymbol{\alpha}}}(\omega) = \frac{\phi\,\nu}{\mathrm{i}\omega}\underline{\underline{\mathbf{k}}}^{-1}(\omega)$, and effective density, $\underline{\underline{\boldsymbol{\rho}}}_{\mathrm{e}}(\omega) = \frac{\varrho_0}{\phi}\underline{\underline{\boldsymbol{\alpha}}}(\omega) = \frac{\eta}{\mathrm{i}\omega}\underline{\underline{\mathbf{k}}}^{-1}(\omega)$, can be introduced as related to the anisotropic tensor of dynamic permeability $\underline{\underline{\mathbf{k}}}$.

Now, the so-called dynamic thermal tortuosity is introduced per analogy to its visco-inertial counterpart (A.41), namely,

$$\alpha_{\mathrm{th}}(\omega) = \frac{\phi\,\nu_{\mathrm{th}}}{\mathrm{i}\omega\,\theta(\omega)}\,. \tag{A.42}$$

Note that at each frequency, the thermal tortuosity is inversely proportional to the dynamic thermal permeability. Using this formula, the effective compressibility (A.28) and its inverse (the effective bulk modulus) can be presented as follows

$$\mathcal{C}(\omega) = \frac{\phi\,\beta(\omega)}{\gamma P_0}\,, \quad B_{\mathrm{e}}(\omega) = \frac{B_0}{\phi\,\beta(\omega)}\,, \quad \text{where} \quad \beta(\omega) = \gamma - \frac{\gamma-1}{\alpha_{\mathrm{th}}(\omega)}\,, \tag{A.43}$$

and $B_0 = \gamma P_0$ is the adiabatic bulk modulus of the pore fluid.

Now, the effective speed of sound and characteristic impedance for the fluid acoustically equivalent to porous medium can be computed from the formulae involving the dynamic tortuosities α and α_{th} (or instead of α_{th}, the more convenient function β defined above), namely,

$$c_{\mathrm{e}}(\omega) = \sqrt{\frac{B_{\mathrm{e}}(\omega)}{\varrho_{\mathrm{e}}(\omega)}} = \frac{c_0}{\sqrt{\alpha(\omega)\beta(\omega)}}\,, \qquad Z_{\mathrm{e}}(\omega) = \varrho_{\mathrm{e}}(\omega)\,c_{\mathrm{e}}(\omega) = \frac{Z_0}{\phi}\sqrt{\frac{\alpha(\omega)}{\beta(\omega)}}\,, \tag{A.44}$$

where $c_0 = \sqrt{B_0/\varrho_0}$ and $Z_0 = \varrho_0 c_0$ are the speed of sound and characteristic impedance of the saturating fluid, respectively. The effective speed of sound allows to calculate the complex wave number

$$k_{\mathrm{w}}(\omega) = \frac{\omega}{c_{\mathrm{e}}(\omega)} = \frac{\omega}{c_0}\sqrt{\alpha(\omega)\beta(\omega)}. \tag{A.45}$$

The real part of this frequency-dependent function is always positive, while the imaginary part is always negative (for $\omega > 0$, and because the positive convention $\exp(+\mathrm{i}\omega t)$ has been adopted), so that the complex wave number may be decomposed into its real and imaginary parts as follows

$$k_{\mathrm{w}}(\omega) = \mathrm{Re}\,k_{\mathrm{w}}(\omega) + \mathrm{i}\,\mathrm{Im}\,k_{\mathrm{w}}(\omega) = \frac{\omega}{c_{\mathrm{w}}(\omega)} - \mathrm{i}\,d_{\mathrm{w}}(\omega), \tag{A.46}$$

where we define

$$c_{\mathrm{w}}(\omega) = \frac{\omega}{\mathrm{Re}\,k_{\mathrm{w}}(\omega)} \quad \text{and} \quad d_{\mathrm{w}}(\omega) = -\,\mathrm{Im}\,k_{\mathrm{w}}(\omega) \tag{A.47}$$

as the real-valued (and positive for $\omega > 0$) frequency-dependent functions of wave speed and wave attenuation, respectively. Note that typically, i.e. for any wave-attenuating media, $c_{\mathrm{w}} = c_0/\,\mathrm{Re}(\sqrt{\alpha\beta})$ is *not* the same as as the real part of the effective speed of sound, $\mathrm{Re}\,c_{\mathrm{e}} = c_0\,\mathrm{Re}(1/\sqrt{\alpha\beta})$. Finally, in such dispersive media, i.e. where $c_{\mathrm{w}} = c_{\mathrm{w}}(f)$, the wavelength λ_{w} is related to the frequency f in a more complex way than by a simple inverse proportionality, although the general formula, $\lambda_{\mathrm{w}} = c_{\mathrm{w}}/f$, remains the same.

When the effective properties of a porous material are determined, the sound absorption of a porous layer (or a multilayered system) of known thickness can be quickly evaluated. To this end, the real-valued frequency-dependent acoustic absorption coefficient is calculated as

$$A(\omega) = 1 - |R(\omega)|^2, \qquad R(\omega) = \frac{Z_{\mathrm{s}}(\omega) - Z_0}{Z_{\mathrm{s}}(\omega) + Z_0}. \tag{A.48}$$

Here, $R(\omega)$ is the reflection coefficient which depends on the characteristic impedance Z_0 of the adjacent fluid (which in the present work is the same as the fluid in pores), and on the complex-valued frequency-dependent surface acoustic impedance $Z_{\mathrm{s}}(\omega)$ of the absorbing layer (or multi-layer). In the case of a single sound-absorbing layer of porous material with open porosity ϕ and thickness h, placed on a rigid, impervious wall, the surface acoustic impedance is found analytically as

$$Z_{\mathrm{s}}(\omega) = -\mathrm{i}\varrho_{\mathrm{e}}(\omega)c_{\mathrm{e}}(\omega)\cot\left(\frac{\omega h}{c_{\mathrm{e}}(\omega)}\right) = -\mathrm{i}\frac{Z_0}{\phi}\sqrt{\frac{\alpha(\omega)}{\beta(\omega)}}\cot\left(\frac{\omega h}{c_0}\sqrt{\alpha(\omega)\beta(\omega)}\right), \tag{A.49}$$

by solving the corresponding Helmholtz problem in the layer of equivalent homogenised medium (with the effective density ϱ_{e} and effective speed of sound c_{e}) placed on a rigid, impervious wall and subject on its free surface to a normally-incident plane harmonic wave.

A.3 Approximations based on transport parameters

Dynamic permeabilities and tortuosities can be determined using scaling functions [24–28] which depend on the kinematic viscosity ν and thermal diffusivity ν_{th} of the pore fluid, and on the so-called transport parameters which are fluid-independent and related to the micro-geometry of the porous medium. In comparison with the direct calculation of the dynamic properties discussed in Section A.2, this is an approximative approach. However, it is significantly less computationally demanding and usually provides accurate predictions. The most enhanced, robust and accurate approximation that will be used in this paper requires 8 transport parameters, namely: the porosity ϕ, the (geometrical) tortuosity α_∞ [24], the static viscous [28] and thermal [26] tortuosities, $\alpha_{0\text{v}}$ and $\alpha_{0\text{th}}$, respectively, the static viscous [8] and thermal [27] permeabilities, $\mathcal{K}_0$ and θ_0, respectively, and two characteristic lengths, namely, Λ_v for viscous forces [24], and Λ_th for thermal effects [25]. The calculation of porosity $\phi = \Omega_\text{f}/\Omega$ is obvious. Below, we thoroughly discuss how to (numerically) determine the other transport parameters. Then, the approximations for the dynamic tortuosity and permeability functions involving these parameters are presented.

The dynamic viscous tortuosity $\alpha(\omega)$ is a generalisation of the concept of tortuosity and (by definition) $\alpha_\infty = \lim_{\omega\to\infty} \text{Re}\,\alpha(\omega) = \lim_{\omega\to\infty} \alpha(\omega)$, since $\lim_{\omega\to\infty} \text{Im}\,\alpha(\omega) = 0$. However, for $\omega \to \infty$ (i.e. in high-frequency regime) and in absence of scattering, the viscosity of fluid can be neglected since its behaviour tends to be as that of an ideal fluid, so that the behaviour of the flow through the porous medium is dominated by the inertia of the saturating fluid. When the viscosity is neglected (i.e. for $\eta = 0$), the Stokes' equations of oscillatory flow (A.12)–(A.14) become the linearised Euler's equations of ideal (i.e. inviscid and incompressible) oscillatory flow, namely,

$$-\text{i}\omega\varrho_0\mathbf{v}^{(0)} = \nabla_x p^{(0)} - \nabla_y p^{(1)} \quad \text{in } \Omega_\text{f}, \tag{A.50}$$

$$\nabla_y \cdot \mathbf{v}^{(0)} = 0 \quad \text{in } \Omega_\text{f}, \tag{A.51}$$

$$\mathbf{v}^{(0)} \cdot \mathbf{n} = 0 \quad \text{on } \Gamma_\text{sf}. \tag{A.52}$$

Notice that the no-slip boundary condition (A.14) for viscous fluid is replaced by the no-penetration condition (A.52) for an inviscid one, where $\mathbf{n}$ is the unit vector normal to the solid boundary Γ_sf. Here, in a way similar to Eqs. (A.15) and (A.16), the velocity $\mathbf{v}^{(0)}$ and local pressure $p^{(1)}$ can be linearly related to the global pressure gradient $\nabla_x p^{(0)}$, which drives the ideal flow (inside the periodic cell Ω_f) described by the system of linear equations (A.50)–(A.52), namely,

$$\mathbf{v}^{(0)}(x,y) = -\frac{\tilde{\underline{\underline{\mathbf{E}}}}(y)}{\text{i}\omega\varrho_0} \cdot \nabla_x p^{(0)}(x), \qquad p^{(1)}(x,y) = -\tilde{\mathbf{q}}(y) \cdot \nabla_x p^{(0)}(x) + \bar{p}^{(1)}(x), \tag{A.53}$$

where $\tilde{\underline{\underline{\mathbf{E}}}}(y)$ represents an Ω-periodic local tensor field, $\tilde{\mathbf{q}}(y)$ is an Ω-periodic local vector field, and $\bar{p}^{(1)}(x)$ is a constant field. For the sake of simplicity, we are narrowing now our discussion to isotropic media or to the flow in a preferential direction $\mathbf{e}$, which means that the pressure gradient forcing the flow is $\nabla_x p^{(0)}(x) = \left\|\nabla_x p^{(0)}(x)\right\| \mathbf{e}$, and the fields of velocity and pressure (A.53) can be expressed as

$$\mathbf{v}^{(0)}(x,y) = -\frac{\left\|\nabla_x p^{(0)}(x)\right\|}{\text{i}\omega\varrho_0}\mathbf{E}(y), \qquad p^{(1)}(x,y) = -\left\|\nabla_x p^{(0)}(x)\right\| q(y) + \bar{p}^{(1)}(x), \tag{A.54}$$

where we have introduced the Ω-periodic vector field $\mathbf{E}(y) \equiv \tilde{\underline{\underline{\mathbf{E}}}}(y) \cdot \mathbf{e}$ and scalar field $q(y) \equiv \tilde{\mathbf{q}}(y) \cdot \mathbf{e}$. Inserting these linear relations into the equations of oscillatory ideal flow (A.50)–(A.52) yields

$$\mathbf{E} = \mathbf{e} - \nabla_y q \quad \text{in } \Omega_\text{f}, \tag{A.55}$$

$$\nabla_y \cdot \mathbf{E} = 0 \quad \text{in } \Omega_\text{f}, \tag{A.56}$$

$$\mathbf{E} \cdot \mathbf{n} = 0 \quad \text{on } \Gamma_\text{sf}. \tag{A.57}$$

This set of equations describes an electric conduction problem of a porous medium made up of a dielectric (i.e. insulating) solid frame and saturated with an electrically conductive fluid, assuming that $\mathbf{e}$ is a global (i.e. external, locally-constant) electric field, while $\mathbf{E}(y)$ is the local electric field and $q(y)$ is the local scalar field of electric potential in the saturating fluid. Although in our case, these quantities have been normalised by $\|\mathbf{e}\|$, so that $\mathbf{e}$ is in fact a dimensionless constant unit-vector field, consequently, $\mathbf{E}$ is also dimensionless, while q has the unit of length (m). In that way, the problem of ideal linear flow through a porous medium (A.50)–(A.52) coincides formally with such electric conduction problem [80–83] described with Eqs. (A.55)–(A.57) which, on the other hand, reduces to a Laplace problem for the Ω-periodic (electric) potential q, namely,

$$\nabla_y^2 q = 0 \quad \text{in } \Omega_\text{f}, \tag{A.58}$$

$$\nabla_y q \cdot \mathbf{n} = \mathbf{e} \cdot \mathbf{n} \quad \text{on } \Gamma_\text{sf}. \tag{A.59}$$

When the solution q is found, the local (Ω-periodic) electric field $\mathbf{E}$ is computed from Eq. (A.55).

Let us now assume that (at least virtually) the solid matrix of porous material is dielectric, while the saturating fluid is characterised by electric conductivity ς_f. Due to the Kirchoff's reformulation of Ohm's law, the electric current density $\mathbf{j}$ at a given location in the saturating fluid is proportional to the electric field $\mathbf{E}$ at that location, namely, $\mathbf{j}(y) = \varsigma_\mathrm{f}\,\mathbf{E}(y)$. The macroscopic electric current density $\mathbf{J}$ through a representative cell Ω of such porous material is the cell average of this local vector field of electric current density, i.e.

$$\mathbf{J} = \langle \mathbf{j}(y) \rangle = \phi \, \langle \mathbf{j}(y) \rangle_\mathrm{f} = \phi \, \varsigma_\mathrm{f} \, \langle \mathbf{E}(y) \rangle_\mathrm{f} \,. \tag{A.60}$$

On the other hand, the macroscopic electric current density $\mathbf{J}$ is related to the macroscopic electric field $\mathbf{e}$ by a similar Ohm's law formulated for the homogenised medium, namely,

$$\mathbf{J} = \varsigma_\mathrm{e} \mathbf{e} \quad \text{where} \quad \varsigma_\mathrm{e} = \frac{\phi \, \varsigma_\mathrm{f}}{\alpha_\infty} \tag{A.61}$$

is the effective electric conductivity of porous medium saturated with conductive fluid [81]; it is directly proportional to the electric conductivity ς_f of the saturating fluid and to the porosity ϕ, while inversely proportional to the tortuosity α_∞ of the pore fluid network.

The comparison of Eqs. (A.60) and (A.61) shows that the tortuosity of porous medium plays the following role in the relation between the global and local electric fields

$$\mathbf{e} = \alpha_\infty \, \langle \mathbf{E}(y) \rangle_\mathrm{f} \,. \tag{A.62}$$

Multiplying both sides of this equation by $\mathbf{e}$ yields

$$\|\mathbf{e}\|^2 = \alpha_\infty \, \langle \mathbf{E} \cdot \mathbf{e} \rangle_\mathrm{f} \,, \tag{A.63}$$

where one may also substitute the following result

$$\langle \mathbf{E} \cdot \mathbf{e} \rangle_\mathrm{f} = \langle \mathbf{E} \cdot \mathbf{E} \rangle_\mathrm{f} + \langle \mathbf{E} \cdot \nabla_y q \rangle_\mathrm{f} = \langle \mathbf{E} \cdot \mathbf{E} \rangle_\mathrm{f} \,, \tag{A.64}$$

obtained by using Eq. (A.55) and the fact that the third averaged term in (A.64) vanishes (by integration by parts), because the electric field is solenoidal, see Eq. (A.56), Ω-periodic, and satisfies the boundary condition (A.57) on the solid walls. Equations (A.63) and (A.64) provide equivalent formulae for tortuosity

$$\alpha_\infty = \frac{\|\mathbf{e}\|^2}{\langle \mathbf{E} \cdot \mathbf{e} \rangle_\mathrm{f}} = \frac{\|\mathbf{e}\|^2}{\langle \mathbf{E} \cdot \mathbf{E} \rangle_\mathrm{f}} . \tag{A.65}$$

Alternatively, the following formula is straightforwardly obtained from Eq. (A.62)

$$\|\mathbf{e}\|^2 = \alpha_\infty^2 \, \langle \mathbf{E} \rangle_\mathrm{f} \cdot \langle \mathbf{E} \rangle_\mathrm{f} \quad \text{or} \quad \alpha_\infty = \frac{\|\mathbf{e}\|}{\|\langle \mathbf{E} \rangle_\mathrm{f}\|} . \tag{A.66}$$

Notice that $\|\mathbf{e}\|^2 = \|\mathbf{e}\| = 1$, if the calculations are carried out for the normalised constant electric field, i.e. unitary vector $\mathbf{e}$. On the other hand, whatever the vector $\mathbf{e}$ is, it can be eliminated from Eqs. (A.65) and (A.66) to get the following formula for tortuosity

$$\alpha_\infty = \frac{\langle \mathbf{E} \cdot \mathbf{E} \rangle_\mathrm{f}}{\langle \mathbf{E} \rangle_\mathrm{f} \cdot \langle \mathbf{E} \rangle_\mathrm{f}} = \phi \frac{\langle \mathbf{E} \cdot \mathbf{E} \rangle}{\langle \mathbf{E} \rangle \cdot \langle \mathbf{E} \rangle} . \tag{A.67}$$

The solution $\mathbf{E}(y)$ of the electric conduction problem through periodic representative cell of a porous medium serves also to determine the viscous characteristic length [24]

$$\Lambda_\mathrm{v} = 2 \frac{\int_{\Omega_\mathrm{f}} \mathbf{E} \cdot \mathbf{E} \, \mathrm{d}\Omega}{\int_{\Gamma_\mathrm{sf}} \mathbf{E} \cdot \mathbf{E} \, \mathrm{d}\Gamma} \,, \tag{A.68}$$

while the thermal length is calculated directly from the porous micro-geometry as twice the ratio of the volume of fluid domain to the surface of solid walls (i.e. the solid-fluid interface) inside the cell

$$\Lambda_\mathrm{th} = 2 \frac{\int_{\Omega_\mathrm{f}} \mathrm{d}\Omega}{\int_{\Gamma_\mathrm{sf}} \mathrm{d}\Gamma} \,. \tag{A.69}$$

It can be demonstrated (see [9, 13, 73]) that for a porous medium with channels parallel to the direction of flow and with arbitrary but constant cross-sections $\alpha_\infty = 1$ (the porous medium is not tortuous) and $2\Lambda_\mathrm{v} = 2\Lambda_\mathrm{th}$ is the well-known hydraulic diameter.

The dynamic viscous permeability $\mathcal{K}(\omega)$ is a generalisation of the (static, viscous) permeability and by definition $\mathcal{K}_0 = \mathcal{K}(0)$ (since $\operatorname{Im}\mathcal{K}(0) = 0$), while $\alpha_{0\mathrm{v}} = \lim_{\omega\to 0}\operatorname{Re}\alpha(\omega)$. Therefore, to calculate the static viscous permeability $\mathcal{K}_0$ and tortuosity $\alpha_{0\mathrm{v}}$, the equations (A.34)–(A.36) are solved for $\omega = 0$. Then, the first term in Eq. (A.34) vanishes and the whole set of equations is not only frequency-independent, but also real-valued and fluid-independent. We denote $\hat{\mathbf{k}}_0(y) \equiv \hat{\mathbf{k}}(y,0)$ and $\hat{\pi}_0 \equiv \hat{\pi}(y,0)$, and solve the following set of equations formulated in terms of the real-valued Ω-periodic unknowns $\hat{\mathbf{k}}_0$ and $\hat{\pi}_0$

$$-\nabla_y^2\hat{\mathbf{k}}_0 + \nabla_y\hat{\pi}_0 = \mathbf{e} \quad \text{in } \Omega_\mathrm{f}, \tag{A.70}$$

$$\nabla_y\cdot\hat{\mathbf{k}}_0 = 0 \quad \text{in } \Omega_\mathrm{f}, \tag{A.71}$$

$$\hat{\mathbf{k}}_0 = \mathbf{0} \quad \text{on } \Gamma_\mathrm{sf}. \tag{A.72}$$

This is a scaled Stokes' problem (i.e. a normalised steady-state viscous flow globally driven in the direction $\mathbf{e}$), and in order to determine the static viscous permeability tensor $\underline{\underline{\mathbf{k_0}}}$ one may proceed as discussed in Section A.2 in the case of the dynamic permeability tensor (incidentally, notice that $\underline{\underline{\mathbf{k_0}}} = \underline{\underline{\mathbf{k}}}(0)$). That means solving the problem (A.70)–(A.72) N-times, independently, for mutually perpendicular directions $\mathbf{e}^{\{i\}}$ ($i = 1,\ldots,N$, where $N = 2$ in 2D and $N = 3$ in 3D); then, the static permeability tensor is computed as $\underline{\underline{\mathbf{k_0}}} = \sum_{i=1}^{N}\mathbf{k}_0^{\{i\}}\otimes\mathbf{e}^{\{i\}}$, where $\mathbf{k}_0^{\{i\}} = \left\langle\hat{\mathbf{k}}_0^{\{i\}}(y)\right\rangle = \phi\left\langle\hat{\mathbf{k}}_0^{\{i\}}(y)\right\rangle_\mathrm{f}$ and the field $\hat{\mathbf{k}}_0^{\{i\}}(y)$ is the solution for $\mathbf{e} = \mathbf{e}^{\{i\}}$. When the anisotropy factor is not large, an isotropic approximation can be applied for the permeability tensor, i.e. $\underline{\underline{\mathbf{k_0}}} \approx \mathcal{K}_0\underline{\underline{\mathbf{I}}}$, where the static viscous permeability has been computed as $\mathcal{K}_0 = \operatorname{tr}\underline{\underline{\mathbf{k_0}}}$. Alternatively (and usually), the static viscous permeability is computed as follows for the preferential flow direction $\mathbf{e}$

$$\mathcal{K}_0 = \left\langle\hat{\mathbf{k}}_0(y)\cdot\mathbf{e}\right\rangle = \phi\left\langle\hat{\mathbf{k}}_0(y)\cdot\mathbf{e}\right\rangle_\mathrm{f}. \tag{A.73}$$

Note that in the case of structural isotropy, the same value of permeability $\mathcal{K}_0$ is obtained for any direction $\mathbf{e}$. Incidentally, when $\mathcal{K}_0$ is known, the static flow resistivity can be computed for a particular fluid as $\sigma_0 = \sigma(0) = \eta/\mathcal{K}_0$. Finally, the static viscous tortuosity is calculated from the solution $\hat{\mathbf{k}}_0(y)$ using the following formula

$$\alpha_{0\mathrm{v}} = \phi\frac{\left\langle\hat{\mathbf{k}}_0\cdot\hat{\mathbf{k}}_0\right\rangle}{\left\langle\hat{\mathbf{k}}_0\right\rangle\cdot\left\langle\hat{\mathbf{k}}_0\right\rangle} = \frac{\left\langle\hat{\mathbf{k}}_0\cdot\hat{\mathbf{k}}_0\right\rangle_\mathrm{f}}{\left\langle\hat{\mathbf{k}}_0\right\rangle_\mathrm{f}\cdot\left\langle\hat{\mathbf{k}}_0\right\rangle_\mathrm{f}}, \tag{A.74}$$

which (if need be) can be generalised for anisotropy to give the second-order tensor of static viscous tortuosity.

Notice that, by definition, $\theta_0 = \theta(0)$ (since $\operatorname{Im}\theta(0) = 0$) and $\alpha_{0\mathrm{th}} = \lim_{\omega\to 0}\operatorname{Re}\alpha_\mathrm{th}(\omega)$. Therefore, to calculate the static thermal permeability θ_0 and tortuosity $\alpha_{0\mathrm{th}}$, the equations (A.38)–(A.39) are solved for $\omega = 0$, which means that the first term in Eq. (A.38) vanishes and the new set of equations describes a Poisson's problem, which is real-valued and frequency- and fluid-independent. By denoting $\tilde{\theta}_0(y) \equiv \tilde{\theta}(y,0)$, the following set of equations, formulated in terms of the real-valued Ω-periodic unknown $\tilde{\theta}_0$, is to be solved

$$-\nabla_y^2\tilde{\theta}_0 = 1 \quad \text{in } \Omega_\mathrm{f}, \tag{A.75}$$

$$\tilde{\theta}_0 = 0 \quad \text{on } \Gamma_\mathrm{sf}. \tag{A.76}$$

Then, the static thermal permeability is calculated as

$$\theta_0 = \left\langle\tilde{\theta}_0(y)\right\rangle = \phi\left\langle\tilde{\theta}_0(y)\right\rangle_\mathrm{f}, \tag{A.77}$$

while the static thermal tortuosity is computed from the following formula

$$\alpha_{0\mathrm{th}} = \phi\frac{\left\langle\tilde{\theta}_0^2\right\rangle}{\left\langle\tilde{\theta}_0\right\rangle^2} = \frac{\left\langle\tilde{\theta}_0^2\right\rangle_\mathrm{f}}{\left\langle\tilde{\theta}_0\right\rangle_\mathrm{f}^2}. \tag{A.78}$$

The transport parameters permit quick, accurate approximations of the dynamic tortuosity and permeability functions characterising the porous medium saturated with air (or other specified fluid). Three approximate models are used throughout this work, or as a matter of fact, an advanced semi-phenomenological model and (additionally) its two enhanced versions, namely:

- **JCA** – the *Johnson-Champoux-Allard* model [24, 25] with 5 transport parameters, i.e. ϕ, α_∞, $\mathcal{K}_0$, Λ_v and Λ_th;

- **JCAL** – the *Johnson-Champoux-Allard-Lafarge* model [24–27] with 6 transport parameters, i.e. 5 parameters as in the JCA model plus the static thermal permeability θ_0;
- **JCALP** – the *Johnson-Champoux-Allard-Lafarge-Pride* model [24–28] with 8 transport parameters, i.e. 6 parameters as in the JCAL model plus the static tortuosities $\alpha_{0\mathrm{v}}$ and $\alpha_{0\mathrm{th}}$.

According to this kind of modelling, the dynamic viscous tortuosity $\alpha(\omega)$ can be estimated as

$$\alpha(\omega) = \alpha_\infty\Big(1 + \frac{\mathcal{F}_\mathrm{v}(\omega)}{\mathrm{i}\omega/\omega_\mathrm{v}}\Big), \quad \text{where} \quad \mathcal{F}_\mathrm{v}(\omega) = 1 - \mathcal{P}_\mathrm{v} + \sqrt{\mathcal{P}_\mathrm{v}^2 + \frac{\mathcal{M}_\mathrm{v}}{2}\frac{\mathrm{i}\omega}{\omega_\mathrm{v}}}\,. \tag{A.79}$$

Here, the viscous characteristic frequency ω_v is introduced, together with the viscous pore-shape factor $\mathcal{M}_\mathrm{v}$ and the low-frequency viscous correction parameter $\mathcal{P}_\mathrm{v}$, namely,

$$\omega_\mathrm{v} = \frac{\phi\,\nu}{\alpha_\infty \mathcal{K}_0}\,, \qquad \mathcal{M}_\mathrm{v} = \frac{8\alpha_\infty \mathcal{K}_0}{\phi\Lambda_\mathrm{v}^2}\,, \qquad \mathcal{P}_\mathrm{v} = \frac{\mathcal{M}_\mathrm{v}}{4(\alpha_{0\mathrm{v}}/\alpha_\infty - 1)}\,. \tag{A.80}$$

The formula for $\mathcal{P}_\mathrm{v}$ depends on the static viscous tortuosity $\alpha_{0\mathrm{v}}$, which is required only by the JCALP model. For the JCA and JCAL models $\mathcal{P}_\mathrm{v} = 1$, and then $\mathcal{F}_\mathrm{v}(\omega) = \sqrt{1 + \frac{\mathcal{M}_\mathrm{v}}{2}\mathrm{i}\omega/\omega_\mathrm{v}}$. Similarly, the dynamic thermal tortuosity $\alpha_\mathrm{th}(\omega)$ is computed as

$$\alpha_\mathrm{th}(\omega) = 1 + \frac{\mathcal{F}_\mathrm{th}(\omega)}{\mathrm{i}\omega/\omega_\mathrm{th}}\,, \quad \text{where} \quad \mathcal{F}_\mathrm{th}(\omega) = 1 - \mathcal{P}_\mathrm{th} + \sqrt{\mathcal{P}_\mathrm{th}^2 + \frac{\mathcal{M}_\mathrm{th}}{2}\frac{\mathrm{i}\omega}{\omega_\mathrm{th}}}\,. \tag{A.81}$$

Here, the thermal characteristic frequency ω_th is introduced, together with the thermal pore-shape factor $\mathcal{M}_\mathrm{th}$ and the low-frequency thermal correction parameter $\mathcal{P}_\mathrm{th}$ defined as follows:

$$\omega_\mathrm{th} = \frac{\phi\,\nu_\mathrm{th}}{\theta_0}\,, \qquad \mathcal{M}_\mathrm{th} = \frac{8\theta_0}{\phi\Lambda_\mathrm{th}^2}\,, \qquad \mathcal{P}_\mathrm{th} = \frac{\mathcal{M}_\mathrm{th}}{4(\alpha_{0\mathrm{th}} - 1)}\,. \tag{A.82}$$

The formula for $\mathcal{P}_\mathrm{th}$ depends on the static thermal tortuosity $\alpha_{0\mathrm{th}}$, which is required by the JCALP model. For the JCA and JCAL models $\mathcal{P}_\mathrm{th} = 1$, and then $\mathcal{F}_\mathrm{th}(\omega) = \sqrt{1 + \frac{\mathcal{M}_\mathrm{th}}{2}\mathrm{i}\omega/\omega_\mathrm{th}}$. Moreover, in the original JCA model, the static thermal permeability θ_0 is not required, because it is approximated by the result obtained, for example, for straight circular channels, i.e. $\theta_0 = \phi\Lambda_\mathrm{th}^2/8$, which means that in this model $\mathcal{M}_\mathrm{th} = 1$ and $\omega_\mathrm{th} = 8\nu_\mathrm{th}/\Lambda_\mathrm{th}^2$.

Using relations (A.41) and (A.42) for the approximations (A.79) and (A.81), the corresponding approximation formulae for dynamic (viscous and thermal) permeabilities are derived, namely,

$$\mathcal{K}(\omega) = \frac{\phi\,\nu}{\mathrm{i}\omega\,\alpha(\omega)} = \frac{\mathcal{K}_0}{\mathrm{i}\omega/\omega_\mathrm{v} + \mathcal{F}_\mathrm{v}(\omega)}, \qquad \theta(\omega) = \frac{\phi\,\nu_\mathrm{th}}{\mathrm{i}\omega\,\alpha_\mathrm{th}(\omega)} = \frac{\theta_0}{\mathrm{i}\omega/\omega_\mathrm{th} + \mathcal{F}_\mathrm{th}(\omega)}. \tag{A.83}$$

It is direct to confirm that $\mathcal{K}(0) = \mathcal{K}_0$ and $\theta(0) = \theta_0$, that is, for $\omega \to 0$ the imaginary parts of $\mathcal{K}$ and θ vanish and these functions take their static values.

B Fillets

Figure B.1 shows a cross-section of the porous periodic structure used for benchmark calculations in Section 3.2 with added fillets with *smooth* inflection points, and provides all necessary data for the exact re-construction of such geometry. Note that it can be easily done using even very simple CAD systems that do not support fillets, but only three geometric primitives, namely, a sphere (for the pores), a cube (for the cubic cell), and a torus (for the manually constructed fillets). The fillet radius R_F is related to the pore radius R_p, and for the sake of the drawing legibility $R_\mathrm{F} = R_\mathrm{p}/10$ in Figure B.1, however, curvature radii of smaller fillets (in particular, those used for numerical calculations of transport parameters) are also depicted to demonstrate how the geometry with fillets tends to the (initial) one with sharp edges, when R_F decreases to zero. In particular, one may compare the radius $\hat{R}_\mathrm{w}$ of sharp-edge windows connecting the pores, with the corresponding radius R_w of a filleted window, namely:

$$\hat{R}_\mathrm{w} = \sqrt{R_\mathrm{p}^2 - \tfrac{1}{4}\ell_\mathrm{c}^2}, \qquad R_\mathrm{w} = R_\mathrm{T} - R_\mathrm{F}, \qquad R_\mathrm{T} = \sqrt{\big(R_\mathrm{p} + R_\mathrm{F}\big)^2 - \tfrac{1}{4}\ell_\mathrm{c}^2}. \tag{B.1}$$

Here, R_T is the large radius of the fillet torus (see Figure B.1). The window radii, as well as the volume of the pore fluid V_f and surface area of the solid skeleton S_s inside the periodic REV, its porosity $\phi = V_\mathrm{f}/\ell_\mathrm{c}^3$, and the thermal characteristic length $\Lambda_\mathrm{th} = 2V_\mathrm{f}/S_\mathrm{s}$, are compared in Table B.1 for various values of the ratio $R_\mathrm{p}/R_\mathrm{F}$ (with fixed $R_\mathrm{p} = 0.11\,\mathrm{mm}$ and decreasing fillet radius R_F). These geometrical results are determined analytically for both cases, i.e. the geometry with

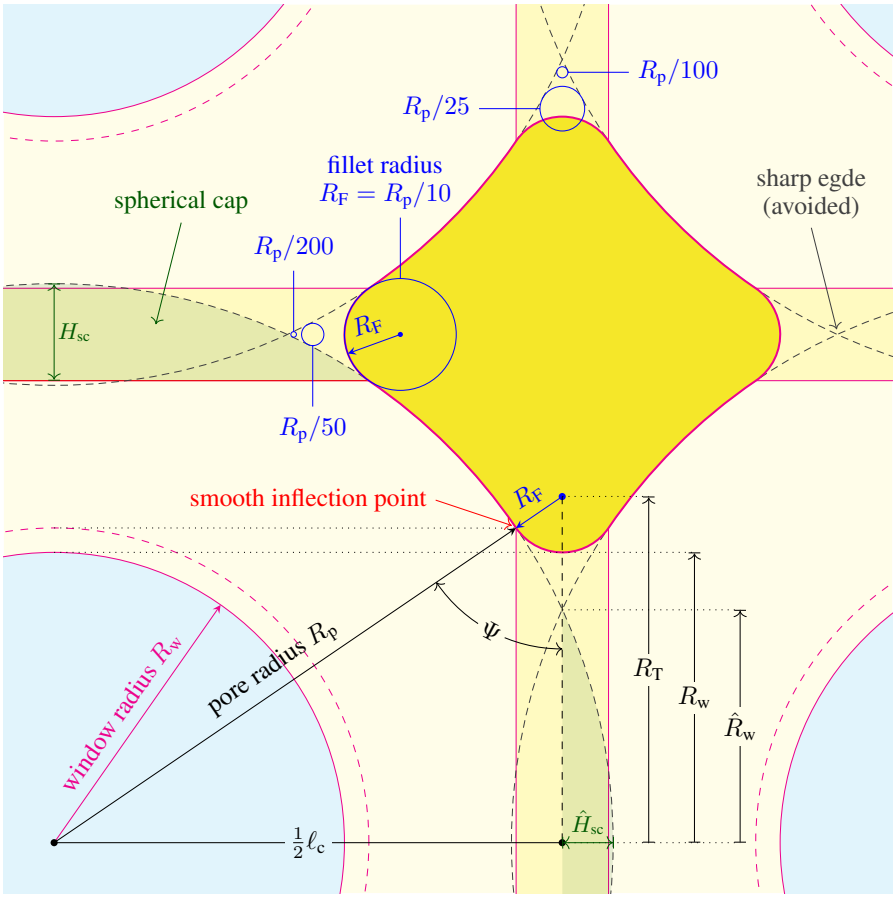

Figure B.1: A cross-sectional view of the regular periodic foam showing the geometry with fillets around the windows connecting the pores

Table B.1: Geometrical features of the periodic REV with fillets (analytical calculations), for decreasing values of R_F (and fixed $R_p = 0.11$ mm), and their convergence toward the corresponding values of the REV with sharp edges (for $R_p/R_F \to \infty$)

R_p/R_F	ϕ (%)	V_f (m^3)	S_s (m^2)	Λ_{th} (m)	R_w (m)
10	68.139	$5.4512 \cdot 10^{-12}$	$9.6596 \cdot 10^{-8}$	$1.1286 \cdot 10^{-4}$	$5.7125 \cdot 10^{-5}$
25	67.364	$5.3891 \cdot 10^{-12}$	$1.0380 \cdot 10^{-7}$	$1.0384 \cdot 10^{-4}$	$5.1164 \cdot 10^{-5}$
50	67.228	$5.3782 \cdot 10^{-12}$	$1.0693 \cdot 10^{-7}$	$1.0059 \cdot 10^{-4}$	$4.8681 \cdot 10^{-5}$
100	67.191	$5.3753 \cdot 10^{-12}$	$1.0869 \cdot 10^{-7}$	$9.8914 \cdot 10^{-5}$	$4.7307 \cdot 10^{-5}$
200	67.181	$5.3745 \cdot 10^{-12}$	$1.0962 \cdot 10^{-7}$	$9.8061 \cdot 10^{-5}$	$4.6581 \cdot 10^{-5}$
∞	67.178	$5.3742 \cdot 10^{-12}$	$1.1058 \cdot 10^{-7}$	$9.7197 \cdot 10^{-5}$	$4.5826 \cdot 10^{-5}$

R_p/R_F	$\phi/\hat{\phi} = V_f/\hat{V}_f$	$S_s/\hat{S}_s$	$\Lambda_{th}/\hat{\Lambda}_{th}$	$R_w/\hat{R}_w$
10	1.01432	0.87351	1.16119	1.24657
25	1.00278	0.93865	1.06832	1.11649
50	1.00075	0.96698	1.03492	1.06230
100	1.00019	0.98283	1.01767	1.03232
200	1.00005	0.99124	1.00889	1.01647

$\hat{\phi}$, $\hat{V}_f$, $\hat{S}_s$, $\hat{\Lambda}_{th}$, $\hat{R}_w$ are the values for $R_p/R_F \to \infty$ (i.e., no fillets), listed in the last row of the upper table.

sharp edges and the one with fillets, from the following formulae for the fluid volume and solid surface, where the "hat" symbol ($\hat{}$) marks the case with sharp edges (i.e. without fillets), namely,

$$\hat{V}_f = \frac{4\pi}{3} R_p^3 - 6\hat{V}_{sc}, \qquad \hat{S}_s = 4\pi R_p^2 - 6\hat{S}_{sc} \qquad \text{(with sharp edges, no fillets)}, \tag{B.2}$$

$$V_f = \frac{4\pi}{3} R_p^3 - 6V_{sc} + 6V_w, \qquad S_s = 4\pi R_p^2 - 6S_{sc} + 6S_w \qquad \text{(for smooth surface with fillets)}, \tag{B.3}$$

where the volumes ($\hat{V}_{\mathrm{sc}}$ and V_{sc}) and surface areas ($\hat{S}_{\mathrm{sc}}$ and S_{sc}), as well as the heights ($\hat{H}_{\mathrm{sc}}$ and H_{sc}) of the relevant spherical caps (see Figure B.1) are

$$\hat{V}_{\mathrm{sc}} = \frac{\pi}{3}\hat{H}_{\mathrm{sc}}^2\big(3R_{\mathrm{p}} - \hat{H}_{\mathrm{sc}}\big), \qquad \hat{S}_{\mathrm{sc}} = 2\pi R_{\mathrm{p}}\hat{H}_{\mathrm{sc}}, \qquad \hat{H}_{\mathrm{sc}} = R_{\mathrm{p}} - \tfrac{1}{2}\ell_{\mathrm{c}} \tag{B.4}$$

$$V_{\mathrm{sc}} = \frac{\pi}{3}H_{\mathrm{sc}}^2\big(3R_{\mathrm{p}} - H_{\mathrm{sc}}\big), \qquad S_{\mathrm{sc}} = 2\pi R_{\mathrm{p}}H_{\mathrm{sc}}, \qquad H_{\mathrm{sc}} = \hat{H}_{\mathrm{sc}} + R_{\mathrm{F}}\sin\Psi, \tag{B.5}$$

respectively, and the volume V_{w} and solid surface area S_{w} inside the filleted window are calculated as

$$V_{\mathrm{w}} = \pi R_{\mathrm{F}}\Big(R_{\mathrm{T}}^2\sin\Psi + R_{\mathrm{F}}^2\big(\sin\Psi - \tfrac{1}{3}\sin^3\Psi\big) - R_{\mathrm{F}}R_{\mathrm{T}}\big(\Psi + \sin\Psi\cos\Psi\big)\Big), \tag{B.6}$$

$$S_{\mathrm{w}} = 2\pi R_{\mathrm{F}}\Big(R_{\mathrm{T}}\Psi - R_{\mathrm{F}}\sin\Psi\Big), \qquad \Psi = \arcsin\frac{\ell_{\mathrm{c}}}{2(R_{\mathrm{p}} + R_{\mathrm{F}})}. \tag{B.7}$$

References

[1] G. Kirchhoff, Ueber den Einfluss der Wärmeleitung in einem Gase auf die Schallbewegung ("About the influence of heat conduction on the sound propagation in a gas"), Annalen der Physik und Chemie 134 (1868) 177–193.

[2] J. W. S. Rayleigh, The Theory of Sound, 2nd ed., Dover, New York, 1945.

[3] C. Zwikker, C. W. Kosten, Sound Absorbing Materials, Elsevier, Amsterdam, 1949.

[4] M. A. Biot, Theory of propagation of elastic waves in a fluid-saturated porous solid. I. low-frequency range, J. Acoust. Soc. Am. 28 (1956) 168–178.

[5] M. A. Biot, Theory of propagation of elastic waves in a fluid-saturated porous solid. II. higher frequency range, J. Acoust. Soc. Am. 28 (1956) 179–191.

[6] K. Attenborough, Acoustical characteristics of porous materials, Physics Reports 82 (1982) 179–227.

[7] T. Levy, E. Sanchez-Palencia, Equations and interface conditions for acoustic phenomena in porous media, J. Math. Anal. Appl. 61 (1977) 813–834.

[8] J. L. Auriault, L. Borne, R. Chambon, Dynamics of porous saturated media, checking of the generalized law of Darcy, J. Acoust. Soc. Am. 77 (1985) 1641–1650.

[9] J. F. Allard, N. Atalla, Propagation of Sound in Porous Media: Modeling Sound Absorbing Materials, 2nd ed., John Wiley & Sons, Chichester, 2009.

[10] H. Tijdeman, On the propagation of sound waves in cylindrical tubes, J. Sound Vib. 39 (1975) 1–33.

[11] A. Craggs, J. G. Hildebrandt, Effective densities and resistivities for acoustic propagation in narrow tubes, J. Sound Vib. (1984) 3213–3231.

[12] M. R. Stinson, The propagation of plane sound waves in narrow and wide circular tubes, and generalization to uniform tubes of arbitrary cross-sectional shape, J. Acoust. Soc. Am. 89 (1991) 50–558.

[13] M. Nori, R. Venegas, Sound propagation in porous materials with annular pores, J. Acoust. Soc. Am. 141 (2017) 4642–4651.

[14] K. Attenborough, Acoustical characteristics of rigid fibrous absorbents and granular materials, J. Acoust. Soc. Am. 73 (1983) 785–799.

[15] V. Tarnow, Compressibility of air in fibrous materials, J. Acoust. Soc. Am. 99 (1996) 3010–3017.

[16] V. Tarnow, Airflow resistivity of models of fibrous acoustic materials, J. Acoust. Soc. Am. 100 (1996) 3706–3713.

[17] V. Tarnow, Calculation of the dynamic air flow resistivity of fiber materials, J. Acoust. Soc. Am. 102 (1997) 1680–1688.

[18] O. Umnova, D. Tsiklauri, R. Venegas, Effect of boundary slip on the acoustical properties of microfibrous materials, J. Acoust. Soc. Am. 126 (2009) 1850–1861.

[19] O. Umnova, K. Attenborough, K. M. Li, Cell model calculations of dynamic drag parameters in packings of spheres, J. Acoust. Soc. Am. 107 (2000) 3113–3119.

[20] O. Umnova, K. Attenborough, K. M. Li, A cell model for the acoustical properties of packings of spheres, Acta Acust. 87 (2001) 226–235.

[21] C. Boutin, C. Geindreau, Estimates and bounds of dynamic permeability of granular media, J. Acoust. Soc. Am. 124 (2008) 3576–3593.

[22] C. Boutin, C. Geindreau, Periodic homogenization and consistent estimates of transport parameters through sphere and polyhedron packings in the whole porosity range, Phys. Rev. E 82 (2010) 036313.

[23] R. Venegas, O. Umnova, Acoustical properties of double porosity granular materials, J. Acoust. Soc. Am. 130 (2011) 2765–2776.

[24] D. L. Johnson, J. Koplik, R. Dashen, Theory of dynamic permeability and tortuosity in fluid-saturated porous media, J. Fluid Mech. 176 (1987) 379–402.

[25] Y. Champoux, J. F. Allard, Dynamic tortuosity and bulk modulus in air-saturated porous media, J. Appl. Phys. 70 (1975-1979) 1991.

[26] D. Lafarge, Propagation du son dans les matériaux poreux à structure rigide saturés par un fluide viscothermique ("Sound propagation in rigid porous media saturated by a viscothermal fluid"), Ph.D. thesis, Université du Maine (France) (1993).

[27] D. Lafarge, P. Lemarinier, J. F. Allard, V. Tarnow, Dynamic compressibility of air in porous structures at audible frequencies, J. Acoust. Soc. Am. 102 (1997) 1995–2006.

[28] S. R. Pride, F. D. Morgan, A. F. Gangi, Drag forces of porous-medium acoustics, Phys. Rev. B 47 (1993) 4964–4975.

[29] K. V. Horoshenkov, J.-P. Groby, O. Dazel, Asymptotic limits of some models for sound propagation in porous media and the assignment of the pore characteristic lengths, J. Acoust. Soc. Am. 139 (2016) 2463–2474.

[30] K. V. Horoshenkov, J.-P. Groby, O. Dazel, Erratum: Asymptotic limits of some models for sound propagation in porous media and the assignment of the pore characteristic lengths [J. Acoust. Soc. Am. 139(5), 2463–2474 (2016)], The Journal of the Acoustical Society of America 147 (1) (2020) 205–205.

[31] K. V. Horoshenkov, A. Hurrell, , J.-P. Groby, A three-parameter analytical model for the acoustical properties of porous media, J. Acoust. Soc. Am. 145 (2019) 2512–2517.

[32] K. V. Horoshenkov, A. Hurrell, J.-P. Groby, Erratum: A three-parameter analytical model for the acoustical properties of porous media [J. Acoust. Soc. Am. 145(4), 2512–2517 (2019)], The Journal of the Acoustical Society of America 147 (1) (2020) 146–146.

[33] S. Gasser, F. Paun, Y. Bréchet, Absorptive properties of rigid porous media: Application to face centered cubic sphere packing, J. Acoust. Soc. Am. 117 (2005) 2090–2099.

[34] C. Perrot, F. Chevillotte, R. Panneton, Bottom-up approach for microstructure optimization of sound absorbing materials, J. Acoust. Soc. Am. 124 (2008) 940–948.

[35] C. Perrot, F. Chevillotte, R. Panneton, Dynamic viscous permeability of an open-cell aluminum foam: Computations versus experiments, J. Appl. Phys. 103 (2008) 024909.

[36] F. Chevillotte, C. Perrot, R. Panneton, Microstructure based model for sound absorption predictions of perforated closed-cell metallic foams, J. Acoust. Soc. Am. 128 (2010) 1766–1776.

[37] R. Venegas, Microstructure influence on acoustical properties of multiscale porous materials, Ph.D. thesis, University of Salford (UK) (2011).

[38] C. Peyrega, D. Jeulin, Estimation of acoustic properties and of the representative volume element of random fibrous media, J. Appl. Phys. 113 (2013) 104901.

[39] T. G. Zieliński, Microstructure representations for sound absorbing fibrous media: 3D and 2D multiscale modelling and experiments, J. Sound and Vib. 409 (2017) 112–130.

[40] H. T. Luu, C. Perrot, V. Monchiet, R. Panneton, Three-dimensional reconstruction of a random fibrous medium: Geometry, transport and sound absorbing properties, J. Acoust. Soc. Am. 141 (2017) 4768–4780.

[41] H. T. Luu, R. Panneton, C. Perrot, Effective fiber diameter for modeling the acoustic properties of polydisperse fiber networks, J. Acoust. Soc. Am. 141 (2017) EL96–EL101.

[42] H. T. Luu, C. Perrot, R. Panneton, Influence of porosity, fiber radius and fiber orientation on the transport and acoustic properties of random fiber structures, Acta Acust. united Acust. 103 (2017) 1050–1063.

[43] M. He, C. Perrot, J. Guilleminot, P. Leroy, G. Jacqus, Multiscale prediction of acoustic properties for glass wools: Computational study and experimental validation, J. Acoust. Soc. Am. 143 (2018) 3283–3299.

[44] M.-Y. Zhou, P. Sheng, First-principles calculations of dynamic permeability in porous media, Phys. Rev. B 39 (1989) 12027–12039.

[45] C.-Y. Lee, M. J. Leamy, J. H. Nadler, Acoustic absorption calculation in irreducible porous media: A unified computational approach, J. Acoust. Soc. Am. 126 (2009) 1862–1870.

[46] T. G. Zieliński, Microstructure-based calculations and experimental results for sound absorbing porous layers of randomly packed rigid spherical beads, J. Appl. Phys. 116 (2014) 034905.

[47] V. V. Dung, R. Panneton, R. Gagné, Prediction of effective properties and sound absorption of random close packings of monodisperse spherical particles: Multiscale approach, J. Acoust. Soc. Am. 145 (2019) 3606–3624.

[48] O. Doutres, N. Atalla, K. Dong, Effect of the microstructure closed pore content on the acoustic behavior of polyurethane foams, J. Appl. Phys. 110 (2011) 064901.

[49] C. Perrot, F. Chevillotte, M. T. Hoang, G. Bonnet, F.-X. Becot, L. Gautron, A. Duval, Microstructure, transport, and acoustic properties of open-cell foam samples: Experiments and three-dimensional numerical simulations, J. Appl. Phys. 111 (2012) 014911.

[50] M. T. Hoang, C. Perrot, Solid films and transports in cellular foams, J. Appl. Phys. 112 (2012) 054911.

[51] M. T. Hoang, C. Perrot, Identifying local characteristic lengths governing sound wave properties in solid foams, J. Appl. Phys. 113 (2013) 084905.

[52] O. Doutres, M. Ouisse, N. Atalla, M. Ichchou, Impact of the irregular microgeometry of polyurethane foam on the macroscopic acoustic behavior predicted by a unit-cell model, J. Acoust. Soc. Am. 136 (2014) 1666–1681.

[53] X. H. Yang, S. W. Ren, W. B. Wang, X. Liu, F. X. Xin, T. J. Lu, A simplistic unit cell model for sound absorption of cellular foams with fully/semi-open cells, Compos. Sci. Technol. 118 (2015) 276–283.

[54] K. Gao, J. A. W. van Dommelen, M. G. D. Geers, Microstructure characterization and homogenization of acoustic polyurethane foams: Measurements and simulations, Int. J. Solids Struct. 100-101 (2016) 536–546.

[55] F. Chevillotte, C. Perrot, Effect of the three-dimensional microstructure on the sound absorption of foams: A parametric study, J. Acoust. Soc. Am. 1428 (2017) 1130–1140.

[56] J. H. Park, K. S. Minn, H. R. Lee, S. H. Yang, C. B. Yu, S. Y. Pak, C. S. Oh, Y. S. Song, Y. J. Kang, J. R. Youn, Cell openness manipulation of low density polyurethane foam for efficient sound absorption, J. Sound Vib. 406 (2017) 224–236.

[57] J. H. Park, S. H. Yang, H. R. Lee, C. B. Yu, S. Y. Pak, C. S. Oh, Y. J. Kang, J. R. Youn, Optimization of low frequency sound absorption by cell size control and multiscale poroacoustics modeling, J. Sound Vib. 397 (2017) 17–30.

[58] K. Gao, J. A. W. van Dommelen, M. G. D. Geers, Investigation of the effects of the microstructure on the sound absorption performance of polymer foams using a computational homogenization approach, Eur. J. Mech. A. Solids 61 (2017) 330–344.

[59] V. H. Trinh, V. Langlois, J. Guilleminot, C. Perrot, Y. Khidas, O. Pitois, Tuning membrane content of sound absorbing cellular foams: Fabrication, experimental evidence and multiscale numerical simulations, Mater. Des. 162 (2019) 345–361.

[60] T. G. Zieliński, Generation of random microstructures and prediction of sound velocity and absorption for open foams with spherical pores, J. Acoust. Soc. Am. 137 (2019) 1790–1801.

[61] J. Park, S. H. Yang, K. S. Minn, C. B. Yu, S. Y. Pak, Y. S. Song, J. R. Youn, Design and numerical analysis of syntactic hybrid foam for superior sound absorption, Mater. Des. 142 (2018) 212–220.

[62] R. Venegas, O. Umnova, Numerical modelling of sound absorptive properties of double porosity granular materials, in: Proceedings of COMSOL Conference 2010, Paris, France, 2010.

[63] F. Chevillotte, C. Perrot, E. Guillon, A direct link between microstructure and acoustical macro-behavior of real double porosity foams, J. Acoust. Soc. Am. 134 (2013) 4681–4690.

[64] R. Venegas, C. Boutin, Enhancing sound attenuation in permeable heterogeneous materials via diffusion processes, Acta Acust. united Ac. 104 (2018) 623–635.

[65] T. G. Zieliński, Pore-size effects in sound absorbing foams with periodic microstructure: modelling and experimental verification using 3D printed specimens, in: P. Sas, D. Moens, A. van de Walle (Eds.), Proceedings of ISMA2016 International Conference on Noise and Vibration Engineering and USD2016 International Conference on Uncertainty in Structural Dynamics, 2016, pp. 95–104.

[66] J. Boulvert, T. Cavalieri, J. Costa-Baptista, L. Schwan, V. Romero-García, G. Gabard, E. R. Fotsing, A. Ross, J. Mardjono, J.-P. Groby, Optimally graded porous material for broadband perfect absorption of sound, J. Appl. Phys. 126 (2019) 175101.

[67] K. C. Opiela, M. Rak, T. G. Zieliński, A concept demonstrator of adaptive sound absorber/insulator involving microstructure-based modelling and 3D-printing, in: W. Desmet, B. Pluymers, D. Moens, W. Rottiers (Eds.), Proceedings of ISMA2018 International Conference on Noise and Vibration Engineering and USD2018 International Conference on Uncertainty in Structural Dynamics, 2018, pp. 1195–1207.

[68] K. C. Opiela, T. G. Zieliński, Microstructural design, manufacturing and modelling of an adaptable porous composite sound absorber, Compos. B Eng. 187 (2020) 107833.

[69] H. Meng, Q. B. Ao, S. W. Ren, F. X. Xin, H. P. Tang, T. J. Lu, Anisotropic acoustical properties of sintered fibrous metals, Compos. Sci. Technol. 107 (2015) 10–17.

[70] W. Chen, T. Chen, F. Xin, X. Wang, X. Du, T. J. Lu, Modeling of sound absorption based on the fractal microstructures of porous fibrous metals, Mater. Des. 105 (2016) 386–397.

[71] S. Ren, F. Xin, T. J. Lu, C. Zhang, A semi-analytical model for the influence of temperature on sound propagation in sintered metal fiber materials, Mater. Des. 134 (2017) 513–522.

[72] S. Ren, Q. Ao, H. Meng, F. Xin, L. Huang, C. Zhang, T. J. Lu, A semi-analytical model for sound propagation in sintered fiber metals, Composites B 126 (2017) 17–26.

[73] T. G. Zieliński, F. Chevillotte, E. Deckers, Sound absorption of plates with micro-slits backed with air cavities: Analytical estimations, numerical calculations and experimental validations, Appl. Acoust. 146 (2019) 261–279.

[74] FreeFEM – A high-level multiphysics finite element software.
https://freefem.org/
(accessed 15 March 2020).

[75] F. Hecht, New development in FreeFem++, J. Numer. Math. 20 (2012) 251–265.

[76] C. Taylor, P. Hood, A numerical solution of the Navier-Stokes equations using the finite element technique, Comput. Fluids 1 (1998) 73–100.

[77] M. Firdaouss, J.-L. Guermond, D. Lafarge, Some remarks on the acoustic parameters of sharp-edged porous media, Int. J. Eng. Sci. 36 (1998) 1035–1046.

[78] J. L. Auriault, C. Boutin, C. Geindreau, Homogenization of Coupled Phenomena in Heterogeneous Media, ISTE, Wiley, 2009.

[79] R. Venegas, C. Boutin, Acoustics of permeable heterogeneous materials with local non-equilibrium pressure states, J. Sound and Vib. 418 (2018) 221–239.

[80] R. J. S. Brown, Connection between formation factor for electrical resistivity and fluid-solid coupling factor in Biot's equations for acoustic waves in fluid-filled porous media, Geophysics 45 (1980) 1269–1275.

[81] M. Avellaneda, S. Torquato, Rigorous link between fluid permeability, electrical conductivity, and relaxation times for transport in porous media, Phys. Fluids A 3 (1991) 2529–2540.

[82] D. Lafarge, Comments on "Rigorous link between fluid permeability, electric conductivity, and relaxation times for transport in porous media", Phys. Fluids A 5 (1993) 500–502.

[83] D. Lafarge, The equivalent fluid model, Materials and Acoustics Handbook, ISTE, Wiley, 2009, Ch. 6, pp. 167–201.